

Characterization and microstructure-based modeling of spot weld failure in hot stamped steel

by

Alireza Mohamadizadeh

A thesis
presented to the University of Waterloo
in fulfillment of the
thesis requirement for the degree of
Doctor of Philosophy
in
Mechanical and Mechatronics Engineering

Waterloo, Ontario, Canada, 2021

©Alireza Mohamadizadeh 2021

Examining Committee Membership

The following served on the Examining Committee for this thesis. The decision of the Examining Committee is by majority vote.

External Examiner:	Professor Mohammad Jahazi Mechanical Engineering, Ecole de Technologie supérieure, Montreal, Quebec, Canada
Supervisor(s):	Professor Michael Worswick and Professor Elliot Biro Mechanical and Mechatronics Engineering University of Waterloo, Waterloo, Canada
Internal Member:	Professor Adrian Gerlich Mechanical and Mechatronics Engineering University of Waterloo, Waterloo, Canada
Internal Member:	Professor Clifford Butcher Mechanical and Mechatronics Engineering University of Waterloo, Waterloo, Canada
Internal-External Member:	Professor Thomas Willett System Design Engineering University of Waterloo, Waterloo, Canada

AUTHOR'S DECLARATION

This thesis consists of material all of which I authored or co-authored: see Statement of Contributions included in the thesis. This is a true copy of the thesis, including any required final revisions, as accepted by my examiners.

I understand that my thesis may be made electronically available to the public.

Statement of Contributions

This thesis consists of 5 chapters: introduction and literature review (Chapters 1 and 2) which represent original work based on available published literature. Chapters 3 and 4 include the original work and a series of published or under review manuscripts that the candidate authored. The thesis has been prepared with a “paper-based” style for which the original papers are provided in the appendices. The candidate is the primary author of all data provided in Chapters 3 and 4. Chapter 5 is the conclusions and future work. The following co-authors have contributed to the current work as outlined below:

Professor Michael Worswick and Professor Elliot Biro supervised the research progress, advised on research direction, reviewed manuscripts and provided technical facilities to conduct the research.

Chapter 3

Mohamadizadeh A, Biro E, Worswick M, Zhou N, Malcolm S, Yau C, Jiao Z, Chen K. “*Spot Weld Strength Modeling and Processing Maps for Hot-Stamping Steels*”. *Weld. J.*, 2019;98:241–9.

The candidate carried out the experimental work, analyzed the data and prepared the manuscript and all associated figures. Prof. Biro and Prof. Worswick’s role were described as above. Prof. Norman Zhou supervised a part of the project on spot welding process modeling, had scientific discussions, and provided access to testing facilities. Mr. Skye Malcolm from Honda Development & Manufacturing of America, Ohio, USA acted as an industrial supervisor, granted access to simulation software, provided financial support, feedback on research direction and edited manuscript. Mr. Cyrus Yao from Magna Promatek research center, Ontario, Canada acted as an industrial and fabrication consultant, provided tooling and material processing consultation, feedback on spot welding process and edited manuscript. Mr. Zhan Jiao and Mr. Kevin Chan from Huys® Industries Ltd., Ontario, Canada acted as spot welding process consultant, provided access to spot weld process modeling software, technical and scientific support, and edited manuscript.

Chapter 4

Mohamadizadeh A, Biro E, Worswick M. “*Shear band formation at the fusion boundary and failure behaviour of resistance spot welds in ultra-high-strength hot-stamped steel*”. *Sci. Technol. Weld. Join.* 2020;0:1–8.

The candidate carried out the experimental work, analyzed the data and prepared the manuscript and all associated figures. Prof. Biro and Prof. Worswick's role were described as above.

Mohamadizadeh A, Biro E, Worswick M. "Novel Double-Half Spot Weld Testing Technique For Damage Progress And Failure Analysis Using Digital Image Correlation Techniques". *Exp. Mech.* 2021.

The candidate carried out the experimental work, analyzed the data and prepared the manuscript and all associated figures. Prof. Biro and Prof. Worswick's role were described as above.

Sherepenko O, Mohamadizadeh A, Zvorykina A, Worswick M, Biro E, Jüttner S. "*Determination of resistance spot weld failure path in ultra-high-strength press-hardened steel by control of fusion boundary transient softening*". *J Mater Sci* 2021;56:14287–97.

The candidate is the secondary author of this published paper. The candidate performed the simulation part of the work based on the experimental data provided by the first author Dr. Oleksii Sherepenko, edited and reviewed the paper (original submission and revisions) and prepared the sections related to spot weld failure simulation. The simulation results and discussions composed by the candidate were included in this thesis. Other work from the paper that was primarily authored by coauthors other than the candidate was not included in this thesis. Dr. Oleksii Sherepenko from OVG University of Magdeburg, Germany performed the conceptualization of the paper and the experimental work, along with writing, revising and editing the paper, Mrs. Anastasiia Zvorykina from OVG University of Magdeburg, Germany participated in conducting the experiments, Prof. Sven Juettner from OVG University of Magdeburg, Germany supervised the project, reviewed manuscripts and provided technical facilities to conduct the research. Prof. Biro and Prof. Worswick's role provided technical and scientific support, reviewed the manuscript, and provided access to the simulation software.

Mohamadizadeh A, Biro E, Worswick M." *Failure characterization and meso-scale damage modeling of spot welds in hot-stamped automotive steels using a hardness-mapping approach*", *Eng. Frac. Mech.* , Under Review (2021).

The candidate carried out the experimental work, analyzed the data and prepared the manuscript and all associated figures. Prof. Biro and Prof. Worswick's role were described as above.

Abstract

The performance of automotive safety components in a crash event depends on the mechanical properties of the sheet metal as well as the failure behavior of the spot welds that are used for sheet metal assembly. Unlike many practical and numerical methods for quantitative and qualitative failure characterization of uniform sheet metals, spot weld failure analysis methods are complicated by the complex microstructure, non-uniform properties and loading conditions around the weld and the fact that spot weld area is not accessible during failure. Therefore, current spot weld failure analysis is typically limited to post-failure observations and peak load measurement. Without having a proper way to characterize the spot weld failure, simple load-based failure criteria were used to predict the onset of failure. In these models the effect of microstructure, through-thickness damage progression, failure mode, the location of failure, post-failure energy absorption, and fracture paths are not considered.

In the present work, spot weld failure for several automotive-grade press-hardening steels, Usibor®1500-AS, Ductibor®1000-AS, and Ductibor®500-AS, is investigated considering the effect of microstructure on failure and a hardness-mapping approach to implement local material properties into meso-scale models. To this end, resistance spot weld process optimization was performed using a combination of experiment and process simulation for five different material conditions including the three aforementioned hot-stamped alloys, as well as two tailored hot stamped conditions using lower quench rates for Usibor®1500-AS. Using the optimized welding settings, a transient softened zone at the fusion boundary, the halo ring, was formed in the as-hot-stamped Usibor®1500-AS spot welds. Optical and electron microscopy showed that, the halo ring is a ~100 µm wide band with a minimum hardness of 472 HV around the weld nugget which leads to partial thickness failure and pull-out through a shear-assisted fracture along the band.

A novel *in-situ* failure characterization test method using modified double half-weld (DHW) specimens coupled with Digital Image Correlation (DIC) was developed to capture the failure event on the cross-section of the welds under shear and normal loading. To demonstrate the capability of the new *in-situ* testing technique for different failure modes, modified RSW parameters were used to eliminate the halo ring in hot-stamped Usibor®1500-AS spot weld and to promote interfacial failure in the hot-stamped Ductibor®1000-AS spot weld. The DIC results revealed that failure is initiated at the weld notch by Corona debonding regardless of spot weld microstructure and loading condition. In

the presence of the halo ring, failure occurs by strain localization and shear band formation at the halo ring. In the absence of the halo ring, fracture occurs parallel to the load under normal loading and within the softened HAZ under shear load. Using the DHW+DIC technique, interfacial failure in the as-hot-stamped Ductibor[®]1000-AS spot weld was found to be a ductile shear-dominant event rather than brittle fracture, as is commonly asserted for interfacial failure in the literature.

A hardness/microstructure mapping approach was used to assign local material properties to a discretized spot weld geometry model which was created with a 3D meshing strategy with nominal element size of 60 μm . The constitutive models and fracture surfaces for the HAZ were calibrated based on tensile and plane-strain V-bend test results and implemented in finite element models of lap-shear and cross-tension tests. The models were able to predict partial and complete pull-out as well as interfacial failure responses, depending upon the alloy and welding process conditions. The predicted failure modes and mechanisms, location of failure, and through-thickness damage progression matched the experimental observations and the predicted failure loads were within 6.3% of measured values.

From the current research, comprising detailed microstructure characterization, development of the novel *in-situ* failure analysis techniques, and meso-scale through-thickness modeling, a fundamental understanding of spot weld failure mechanisms and damage progression has been established, which was the key outcome of this research.

Acknowledgements

First, I would like to give my warmest thanks to my supervisors, Prof. Michael Worswick and Prof. Elliot Biro for their leadership, continuous support, and patience through the past 5 years. I would like to express my sincere gratitude and appreciation to Prof. Michael Worswick for giving me the opportunity to be part of his research group working on a project of my dreams in the automotive industry. Prof. Worswick trusted in my abilities and provided me the freedom to pursue my research interests and cultivating my curiosities. His teachings broadened my horizons in both academic and living qualities that will carry on forever. I would also like to appreciate all the time and energy Prof. Biro put into teaching thousands of invaluable lessons in research, writing, and real life. I truly appreciate his patience, understanding, and inspiring supervision through this research. Working with you has been a boundless honor and one my greatest experience I ever had.

I would like to thank Prof. Mohammad Jahazi, Prof. Thomas Willett, Prof. Clifford Butcher, and Prof. Adrian Gerlich for agreeing to be members of my committee. I appreciate their time and invaluable feedback on my work.

I would like to extend my sincere gratitude to Sky Malcolm from Honda Development & Manufacturing of America, Cyrus Yao from Magna Promatek research center, Dan Papalazarou and Willie Bernert from ArcelorMittal Dofasco for their continual support and feedback on research progress and publications. I would also like to thank Auto/Steel Partnership for providing academic and financial support for this project.

There are many people at the University of Waterloo I would like to thank for helping me through my journey: Eckhard Budziarek, Tom Gawel, Andy Barber and Dough Hirst who helped me with tools and materials in the lab. Thanks to Pedram Samadian, Cameron Tolton, Cameron O’Keeffe, Armin Abedini, Jose Imbert, Abdelbaset Midawi, Amir Zhumagulov, Ryan George, Alex Sherepenko, Matt Tummers, Steven Lee, Ali Keshavarzkermani, Ali Ghatei, Reza Tangestani,

I would like to thank my father, Javad, my mother, Nahid, and sister, Neda, for their unconditional support and positive thoughts who are always my safe havens and pure sources of spiritual energy. I am more grateful to you than you'll ever know. Last, but not certainly least, I would like to give a special thanks to my wife, Negar, for standing by me in happiness and sadness, for being so patient and supportive, and for being the reason for all I fought and tried for.

Dedication

To My Father, who taught me how to live

To My Mother, who taught me how to Love

To My Wife, whom I live with her love

Table of Contents

Examining Committee Membership.....	ii
AUTHOR'S DECLARATION	iii
Statement of Contributions.....	iv
Abstract	vii
Acknowledgements	ix
Dedication	x
List of Figures	xiv
List of Tables.....	xix
List of Publications.....	xx
Chapter 1 Introduction.....	1
1.1 Background	1
1.2 Thesis Outline.....	2
Chapter 2 Literature Review and Current Scope.....	4
2.1 Overview	4
2.2 Press-Hardenable Steel.....	4
2.3 Resistance Spot Welding.....	7
2.3.1 Process Parameters of RSW	8
2.3.2 Material Parameters.....	10
2.4 Microstructure of Spot Welds	11
2.5 Mechanical Properties of Spot Welds	13
2.6 Failure Characterization of Spot Weld	17
2.6.1 Spot Weld Failure Modes.....	17
2.6.2 Effect of Microstructure in Spot Weld Failure.....	20
2.7 Characterization Methods for Local Material Properties	23
2.7.1 Direct methods.....	23
2.7.2 Indirect Methods.....	25
2.8 Numerical Modeling of Spot Weld Failure	27
2.8.1 Damage and Failure Analysis.....	27
2.8.2 General Failure and Damage Modeling.....	29
2.8.3 Damage and Failure Criteria for Spot Welds	32
2.8.4 Spot Weld Failure Simulation	34

2.9 Summary of Previous Work.....	36
2.10 Research Objectives and Scope	36
2.10.1 Objectives	36
2.10.2 Research Scope	37
Chapter 3 Experiments and Methodology	39
3.1 Overview.....	39
3.2 Material Preparation.....	39
3.3 Spot Weld Process Development (Task 1)	43
3.4 Mechanical Testing.....	45
Chapter 4 Results and Discussion.....	48
4.1 Overview.....	48
4.2 Spot Weld Characterization (Task 2).....	48
4.2.1 Microstructure of Spot Welds	48
4.2.2 Microhardness Profiles	51
4.2.3 Characterization of the Transient Softened Zone in U1500-FQ	52
4.3 Failure Behavior of Spot Welds (Task 3)	54
4.3.1 Load-displacement Curves and Failure Modes.....	54
4.3.2 Role of the Halo Ring and Softened HAZ	58
4.4 <i>In-situ</i> Failure Analysis and Damage Accumulation (Task 3 Cont.)	61
4.4.1 Modified Test Coupon Geometries.....	61
4.4.2 Modified RSW Parameters	63
4.4.3 DIC Results and Real-time Failure Analysis	64
4.5 Meso-scale Spot Weld Damage Modeling (Task 4)	71
4.5.1 Selected Spot Weld Conditions for Modeling	73
4.5.2 Hardness-mapping Modeling Approach	73
4.5.3 Spot Weld Failure Model Description	75
4.5.4 Local Material Property Measurement.....	77
4.5.5 Meso-Scale Spot Weld Failure Simulation	85
4.6 Summary	94
Chapter 5 Conclusions and Future Work.....	97
5.1 Conclusions.....	97
5.2 Recommendation for Future Work	99

Letters of Copyright Permission.....	101
Bibliography	113
Appendix A	129
Appendix B.....	130
Appendix C.....	131
Appendix D	132
Appendix E.....	133

List of Figures

Figure 2-1. Illustration of (a) Direct hot stamping, (b) Indirect hot stamping processes [17].	6
Figure 2-2. Schematic of a B-pillar made by (a) Tailor heated, and (b) Tailor welded hot stamping methods [20].	7
Figure 2-3. Resistance spot welding process (a) Initial configuration, (b) Squeezing, (c) Welding, and (d) Cooling.	8
Figure 2-4. Schematic trend of electrical resistance and corresponding temperature as a function of distance [24].	9
Figure 2-5. A typical welding lobe showing the boundaries and constraints for process welding parameters [9].	10
Figure 2-6. A schematic illustration of different zones in a typical spot weld cross-section, corresponding peak temperatures and an example of microstructure for a DP600 steel. Based on [9,37].	11
Figure 2-7. (a) The typical temperature gradient in HAZ of spot weld and sub-categories, and (b) to (e) corresponding room temperature microstructure for MS1200 Martensitic steel (0.09 wt.%C) (Based on [38,40]).	13
Figure 2-8. The schematic illustration of different loading conditions for evaluating mechanical properties of spot welds (a) lap-shear test and (b) cross-tension test (based on [46]).	14
Figure 2-9. Schematic illustration of (a) KSII test specimen and testing configurations for different loading conditions (adopted from Tolton [48]), and (b) H-shaped test specimens according to SEP 1220-p2 European standard [50] (the iso-view images of the H-shaped samples were adopted from Heidrich <i>et al.</i> [54]).	16
Figure 2-10. Typical load vs. displacement curve obtained from quasi-static LS and CT tests (based on [55]).	17
Figure 2-11. Schematic representation of failure modes in spot weld and corresponding examples of fracture surfaces for different failure modes (based on [46,58]).	18
Figure 2-12. Effect of weld nugget size on the failure mode and peak load [60].	19
Figure 2-13. Typical load-displacement curves for IF and PF modes under shear-tension load [61].	20
Figure 2-14. (a) Hardness profile of weld nugget and (b) microstructure after failure for DP450 [64].	21
Figure 2-15. Microhardness profile and microstructures for spot welds of the same size in (a) and (c) DP590 and (b) and (d) DP980 [65].	22

Figure 2-16. Sample preparation for miniaturized tensile test used by Tong <i>et al.</i> [75] for direct measurement of local material properties.....	24
Figure 2-17. Strain field measurement on the surface of spot welded samples using DIC technique (a) notched tensile sample in Usibor®1500 steel [78], (b) 3D DIC results used for lap-shear and V-bend tests in Usibor®1500 steel [79].....	25
Figure 2-18. Example of spot weld material reproduction for indirect local material properties measurement used by Raath <i>et al.</i> [81]. (a) SORPAS® simulated temperature history, (b) extracted temperature history for the points of interest, (c) Gleeble simulated temperature history to achieve the target temperature.....	26
Figure 2-19. Different types of fracture in standard tensile samples and spot welds with respect to the identified failure modes in bulk metals (Fractographs adopted from [92]).....	28
Figure 2-20. Rotational relationships between hexagonal solid elements (4 or 8 solid elements) for the spot weld and quadrilateral shell elements for the sheet [131].....	35
Figure 2-21. Flow chart of project progression showing the main objectives and deliverables for each task.	38
Figure 3-1. As-received microstructures of (a) Usibor®1500-AS, (b) Ductibor®1000-AS, (c) Ductibor®500-AS.	40
Figure 3-2. The optical and electron microstructures of selected PHS materials after hot stamping in different conditions.....	42
Figure 3-3. An example of side-by-side comparison of simulation results and experimental measurements for RSW at 7 kA, 700 ms, and 3.5 kN for (a) U1500-FQ and (b) D500-FQ.....	44
Figure 3-4. 3D welding lobes developed based on the validated simulation results.	44
Figure 3-5. Lap-shear and cross-tension test sample geometries and dimension based on AWS D8.1 [53]. Dimensions are in mm.	46
Figure 3-6. Sub-sized Tensile test specimen (dimensions are in millimeters)	46
Figure 3-7. V-bend test specimen and testing apparatus in accordance with VDA 238-100 [148].	47
Figure 4-1. Optical micrographs of spot welds indicating the sub-regions within the spot welds for (a) U1500-FQ, (b) D1000-FQ, (c) D500-FQ, (d) U1500-400, and (e) U1500-700.....	50
Figure 4-2. SEM images of spot weld subregions for U1500-FQ spot weld, (a) CG-HAZ, (b) FG-HAZ, (c) IC-HAZ, and (d) SC-HAZ. M: Martensite, F: Ferrite, TM: Tempered Martensite, B: Bainite	51
Figure 4-3. Microhardness profiles across the spot welds for different base material conditions.	52

Figure 4-4. Microstructure of the U1500-FQ spot weld showing (a) the optical micrograph under partial light, (b) the EBSD - IPF map of the FB, and (c) the EBSD -KAM map of the FB.....	53
Figure 4-5. Load-displacement curves obtained from lap-shear and cross-tension tests for different material conditions and thicknesses.....	55
Figure 4-6. Relationship between the measured peak load and displacement at failure for different material conditions and sheet thickness (a) Lap-shear, and (b) Cross-tension.	56
Figure 4-7. Macroscopic images of failed samples under shear and normal loads for U1500-FQ and D500-FQ spot welds.	57
Figure 4-8. Identified spot weld failure modes for different spot welds, thicknesses and loading conditions based on AWS D8.1 specifications [53].....	58
Figure 4-9. Optical micrographs of U1500-FQ spot weld showing (a) and (b) the post-failure microstructure and the location of failure, and (c) interrupted lap-shear test showing shear band formation along the halo ring.....	59
Figure 4-10. The optical and SEM micrographs obtained from U1500-FQ spot weld failed under shear loading showing failure due to shearing at the halo ring: (a) the non-symmetrical shape of the weld nugget after failure, which appears smaller on the side where failure is initiated (b) overall shape of the weld nugget, (c) higher magnification of the blue rectangle in (b), (d) Higher magnification image showing the S-shaped shear band (A) and heavily distorted band (B) due to failure.	60
Figure 4-11. Schematic of the modified double half-weld lap-shear test geometry.	62
Figure 4-12. Schematic for KSII (U-shaped) test coupon, (a) conventional KSII coupon (adopted from AWS C1.1 standard [153]), (b) modified KSII pre-weld coupon, (c) welded modified KSII assembly, and (d) Final DHW KSII test sample.....	63
Figure 4-13. DIC results for a U1500-FQ DHW lap-shear test sample that exhibited mode 2 pull-out failure under shear loading (a) strain map, (b) macro-etched samples.	66
Figure 4-14. DIC results for a D1000-FQ DHW lap-shear test sample that exhibited mode 7 interfacial failure under shear loading (a) strain map, (b) macro-etched samples, and (c) SEM Fractograph.	68
Figure 4-15. DIC results for a U1500-FQ DHW KSII test sample that exhibited mode 2 pull-out failure under normal loading (a) strain map, (b) macro-etched samples.	69
Figure 4-16. DIC results for a D1000-FQ DHW KSII test sample that exhibited mode 2 pull-out failure under normal loading (a) strain map, (b) macro-etched samples.	71

Figure 4-17. Spot weld region discretization based on hardness and definition of local material conditions for (a) U1500-FQ, and (b) D1000-FQ.	74
Figure 4-18. Correspondence between actual test specimen and the reduced physical domain for simulation.	76
Figure 4-19. Detailed weld geometry for U1500-FQ-with-halo and isolated sub-region within the weld (Quarter symmetry model for normal loading test).	77
Figure 4-20. Engineering stress-strain curves for hot-stamped U1500 and D1000 adopted from Samadian <i>et al.</i> [162] and Lee [161] and the tempered HAZ materials.	78
Figure 4-21. Linear relationship between stress at 5% elongation with hardness for as-hot-stamped and tempered martensitic (HAZ) conditions. As-hot stamped tensile data for U1500-FQ due to Samadian <i>et al.</i> [32] and for D1000 due Lee [42]	79
Figure 4-22. True stress versus equivalent plastic strain curves and fitted modified Hockett-Sherby constitutive models to the engineering stress-strain data in using Equation 4-3.	80
Figure 4-23. Linear relationship between fracture strain in plane-plane strain condition with the hardness of hot-stamped materials (Adopted from [162] and [161]) and HAZ material conditions....	81
Figure 4-24. Fracture loci for hot-stamped U1500 and D1000 (adopted from [162] and [161]) and HAZ materials using linear interpolation based on hardness.	83
Figure 4-25. 3D Bai-Wierzbicki fracture loci calculated from the 2D plane stress fracture loci in Figure 13 (a) U1500, and (b) D1000. The plane stress loci corresponding to the T1 material condition are also plotted for each alloy (solid curves).	84
Figure 4-26. Failure simulation results for spot welds under normal loading showing the location of failure and damage progression through the thickness for (a), (b) and (c) U1500-FQ-with-halo, (d), (e) and (f) U1500-FQ-no-halo, and (g), (h) and (i) D1000-FQ spot welds. Loading direction is shown by orange arrows.	86
Figure 4-27. Failure simulation results for spot welds under normal loading showing the location of failure and damage progression through the thickness for (a), (b) and (c) U1500-FQ-with-halo, (d), (e) and (f) U1500-FQ-no-halo, and (g), (h) and (i) D1000-FQ spot welds. Loading direction is shown by orange arrows.	87
Figure 4-28. Predicted versus experimentally examined cross-section of spot welds showing the location of failure under (a), (b) and (c) Normal loading, and (d), (e), and (f) shear loading for different spot weld conditions.	89
Figure 4-29. Post-failure analysis of interfacial failure in D1000-FQ spot weld.	90

Figure 4-30. Predicted strain-stress state history of the critical element for U1500-FQ-with-halo spot weld in lap-shear test. Critical element is shown in the inset finite element mesh.	91
Figure 4-31. Predicted strain-stress state history of the critical element for D1000-FQ spot weld in lap-shear test. Critical element is shown in the inset finite element mesh.	92
Figure 4-32. Comparison of predicted and experimental load-displacement curves for different spot welds under (a), (b) and (c) under normal, and (d), (e), and (f) under shear loading.	93
Figure 4-33. Predicted versus measured peak load data for different spot welds and loading conditions.	94

List of Tables

Table 2-1 The nominal mechanical properties of several PHS grades produced by ArcelorMittal [16].	5
Table 3-1 The chemical composition of the PHS selected for this research (wt.%)	39
Table 3-2 The summary of material conditions and hot-stamping parameters	41
Table 3-3 The average hardness values and phase fractions (F is ferrite, B is bainite, P is pearlite, and M is martensite) for the PHSs in the as-received and hot-stamped conditions	42
Table 3-4 The optimized welding parameters (baseline) for different material thicknesses	45
Table 3-5 The modified welding parameters used for promoting specific failure behavior	45
Table 4-1. Heat-treatment specifications, target and measured hardness values for recreated HAZ materials	75
Table 4-2. Hardness values assigned to different weld regions shown in Figure 4-19	77
Table 4-3. Calibrated constants for the modified Hockett-Sherby material model (Equation 4-3).....	81
Table 4-4. Calibrated constants for the Bai-Wierzbicki fracture surface equation (Equation 4-5).....	84

List of Publications

1. Mohamadizadeh A, Biro E, Worswick M, Zhou N, Malcolm S, Yau C, Jiao Z, Chen K. “Spot Weld Strength Modeling and Processing Maps for Hot-Stamping Steels”. *Weld. J.*, 2019;98:241–9. <https://s3.amazonaws.com/WJ-www.aws.org/supplement/2019.98.021.pdf>
2. Mohamadizadeh A, Biro E, Worswick M. “Shear band formation at the fusion boundary and failure behaviour of resistance spot welds in ultra-high-strength hot-stamped steel”. *Sci. Technol. Weld. Join.* 2020;0:1–8. <https://www.tandfonline.com/doi/full/10.1080/13621718.2020.1773057>
3. Mohamadizadeh A, Biro E, Worswick M. “Novel Double-Half Spot Weld Testing Technique For Damage Progress And Failure Analysis Using Digital Image Correlation Techniques”. *Exp. Mech.* 2021. <https://doi.org/10.1007/s11340-021-00743-4>
4. Sherepenko O, Mohamadizadeh A, Zvorykina A, Worswick M, Biro E, Jüttner S. “Determination of resistance spot weld failure path in ultra-high-strength press-hardened steel by control of fusion boundary transient softening”. *J Mater Sci* 2021;56:14287–97. <https://doi.org/10.1007/s10853-021-06165-w>
5. Mohamadizadeh A, Biro E, Worswick M.” Failure characterization and meso-scale damage modeling of spot welds in hot-stamped automotive steels using a hardness-mapping approach”, *Eng. Fra. Mech.*, Submitted (2022).

Chapter 1

Introduction

1.1 Background

Development of light weight structures for vehicles is a primary concern of the automotive industry to tackle the global issue of greenhouse gas emissions and to improve passenger safety. To this end, various generations of advanced high strength steels (AHSS) and thermo-mechanical forming techniques have been developed during the last decades. By using AHSS for structural components, it is possible to decrease the material thickness used in vehicle construction, while maintaining the strength of automotive parts. However, limited formability, springback, and high production costs are major issues associated with application of conventional AHSS [1]. These issues were addressed by the development of hot press forming, that involves simultaneous hot forming and die-quenching of low-alloyed boron-containing steels [2]. The mechanical properties of press-hardened steel (PHS) prior to hot stamping is similar to conventional high strength steels with a tensile strength of 600 MPa [3]. Boron and carbon improve hardenability of the PHS during rapid cooling so that a martensitic microstructure with ultra-high strength levels (>1000 MPa) are achieved.

Different commercial grades of PHS are now available for various automotive applications. An example is Usibor[®]1500 (produced by ArcelorMittal) with an ultimate tensile strength of 1500 MPa and 5% total elongation to rupture in the hot-stamped condition [4]. Usibor[®]1500 is currently used in anti-intrusion B-pillar structures (the vertical pillar between the front and rear doors) for protecting the passenger cabin during side impact [5]. On the other hand, more ductile PHS grades are used for absorbing high impact energy through controlled deformation during crash. An example is Ductibor[®]500, which has an ultimate tensile strength of 700 MPa and 16% total elongation to fracture [4] and is used in frontal crash components with the aim of impact energy absorption during frontal crash incidents [6]. There are also some PHS grades with intermediate strength, such as Ductibor[®]1000, with a combination of high strength (~ 1000 MPa) and moderate ductility ($\sim 6\%$ elongation) in hot-stamped condition.

Although the intrinsic properties of PHSs are promising, Williams and Parker [7] demonstrated that the durability and safety design of automobiles are significantly influenced by weld and joint performance. Resistance spot welding (RSW) is the most commonly used joining technique in the automotive industry due to its low cost, rapid production, and high reliability. Typically, the Body-in-White (BIW) structure of a modern vehicle has somewhere between 2000 to 6000 spot welds [8].

Therefore, the integrity of the entire structure is affected by the performance of the spot welds. It has been shown that spot welds fail in different failure modes, depending on loading condition, material properties, and welding parameters, which affects total strength and amount of energy absorbed by the joint before complete failure [9]. Considering the large number of spot welds within a body structure, it is important to investigate the RSW process development and failure behavior to improve safety and overall performance of vehicles. Another important aspect of RSW research is the numerical analysis of failure and damage modeling, which is essential to predict spot weld failure in crash simulation and to understand failure micro-mechanisms. However, the majority of current modeling approaches utilize simplified spot weld failure models that only consider rudimentary load-based criteria to predict the onset of failure [10,11].

Although, there are many reports on the substantial effects of spot weld microstructure, local material properties, and damage progression on failure behavior of spot welds, there are still several unexplored areas in the spot weld characterization and failure analysis of the newly developed PHS grades. The current gaps in the literature include, but are not limited to: effect of microstructure on mechanical properties, failure mechanisms, through-thickness damage progression, and numerical modeling of failure and damage progression, taking local material properties into account.

The present study aims to determine the effect of spot weld microstructure on failure behavior, identify through-thickness damage mechanisms, and develop mesoscale failure models by taking local material properties into account.

1.2 Thesis Outline

The present thesis has been prepared in a manuscript-based format, comprising this synopsis which consists of five chapters, accompanied by five appendices corresponding to the original research publications. This chapter (Chapter 1) introduces the topic, background and overall objectives of this research. A comprehensive review of the relevant published literature is presented in Chapter 2, including the RSW process, weld microstructure, failure analysis, and failure modeling of advanced high-strength steels. At the end of chapter two, the scope and objectives of the current work are discussed in detail based on the identified gaps in the literature to date. Chapter 3 describes the experimental procedures that were used throughout the research. Also presented in Chapter 3 are the base material conditions, RSW process development, preliminary microstructural observations, and mechanical testing procedures. In Chapter 4, a summary of the results is presented and discussed

which builds on microstructural examination and spot weld failure analysis as the foundation for the development of mesoscale failure models. Lastly, Chapter 5 summarizes the main findings of the research, conclusions, and proposed topics for future research. All content of the published or submitted peer-reviewed manuscripts presented within this thesis can be found in the appendices.

Below is the list of published/submitted peer-reviewed papers by the candidate (available in the appendices) where more detailed presentation of the results can be found:

- Appendix A Mohamadizadeh A., Biro E., Worswick M., Zhou N., Malcolm S., Yau C., Zhen J., Chan K. “Spot Weld Strength Modeling and Processing Maps for Hot-Stamping Steels”. *Welding Journal*, vol. 98, p. 241–249, 2019.
- Appendix B Mohamadizadeh A., Biro E., Worswick M. “Shear Band Formation at The Fusion Boundary and Failure Behaviour of Resistance Spot Welds in Ultra-high-Strength Hot-stamped Steel”. *Science and Technology of Welding and Joining*, vol. 25 (7), p. 556-563, 2020.
- Appendix C Mohamadizadeh, A., Biro, E., Worswick, M. Novel Double-Half Spot Weld Testing Technique for Damage Progress and Failure Analysis Using Digital Image Correlation Techniques. *Experimental Mechanics*, vol. 61(9), p. 1405-141, 2021.
- Appendix D Sherepenko, O., Mohamadizadeh A., Zvorykina A., Worswick M., Biro E., Jüttner S., Determination of Resistance Spot Weld Failure Path in Ultra-high-strength Press-hardened Steel by Control of Fusion Boundary Transient Softening, *Journal of Material Science*, vol. 56, p. 14287-14297, 2021.
- Appendix E Mohamadizadeh, A., Biro, E., Worswick, M. Failure Characterization and Mesoscale Damage Modeling of Spot Welds in Hot-stamped Automotive Steels using a Hardness-mapping Approach. *Engineering Fracture Mechanics*, **Under Review**, December 2021.

Chapter 2

Literature Review and Current Scope

2.1 Overview

The overall performance of spot welds under various loading conditions depends on the geometrical and microstructural characteristics of the joint. From the RSW processing standpoint, both the material properties and the process parameters are important factors which determine the quality and performance of the spot weld during failure. The state of loading around the spot weld nugget is complex, due to the non-uniform distribution of material properties across the weld region. Therefore, failure analysis, identification of damage mechanisms, and failure prediction can be quite difficult tasks. This chapter provides a critical review of the RSW process, mechanical properties, and failure modeling in advanced high-strength steels (AHSS) for automotive application. The review includes but is not limited to the effect of weld microstructure on mechanical properties, practical methods for failure analysis of spot welds, and current spot weld failure modeling approaches.

2.2 Press-Hardenable Steel

The hot stamping process was first invented in the early 1970s by Swedish Steel Works, Norrbottens Järnverk AB (NJA), to produce parts used in the agricultural and construction industries. In the original patent [12], the hot stamping technology was described as a thermomechanical treatment consisting of sequential heating, forming, and cooling stages that strengthen boron steels during forming. Commercialization of hot stamping in Europe starting in the 1980's and the technology has attracted tremendous interest from automotive companies for side impact beams [2]. By the late-1990s, more than 9 million hot-stamped parts were produced worldwide with an increase in application from side impact beams to front and rear bumper reinforcements [13]. At the time, 22MnB5 was the most commonly used boron steel with refined chemical composition and optimal combination of mechanical properties, weldability, and cost. ArcelorMittal patented a hot-dip-aluminized version of 22MnB5, known as Usibor[®]1500-AS in 1999 for hot stamping and commercialized the application in 2007 [14]. More ductile versions of Usibor[®] were also developed by ArcelorMittal, known as Ductibor[®] grades, with lower carbon and boron content. The nominal mechanical properties of Usibor[®]1500 and the two grades of Ductibor[®] considered in the current research are listed in Table 2-1. Further development has increased the number of hot-stamped parts

used per vehicle dramatically as the total number of parts made worldwide increased to 107 million parts per year in 2007 [2,13] and was estimated to be 700 million parts per year in 2017 [15].

Table 2-1 The nominal mechanical properties of several PHS grades produced by ArcelorMittal [16].

Steel Grade	Yield Stress (MPa)	Tensile Strength (MPa)	Elongation to Rupture (%)	Bending Angle (°)
Usibor®1500	≥1050	≥1400	5	≥50
Ductibor®500	≥350	≥550	14	≥90
Ductibor®1000	≥800	≥1000	6	≥80

*The properties are measured after 5 to 10 minutes of heating in a furnace at 880 to 930 °C followed by quenching in cooled hot stamping tools.

Conventional hot stamping can be done in two different ways: direct and indirect hot stamping (Figure 2-1). In the direct hot stamping of boron steels, a blank is heated in a furnace to reach the austenitization temperature, then transferred to the press with chilled dies followed by a simultaneous forming and quenching process (Figure 2-1a). The indirect hot stamping process has an extra stage at the beginning of the process in which the blank is cold formed up to 90-95% of its final shape (Figure 2-1b) [17]. This pre-form ensures that geometrical details are well formed before quench hardening during the final stage of hot stamping.

While the direct method is commonly used in most applications, indirect hot stamping is more beneficial when dealing with complex parts made out of ductile materials (good room temperature formability) or for cases in which reduction of tool wear is important [18]. From a material science viewpoint, an austenitic microstructure at elevated temperature (in the range of 800 to 950 °C) provides good formability during stamping [17]. As soon as the sheet starts to be formed by the dies into channels and cavities, material temperature decreases at contact points; however, the main quenching process occurs when the blank fully contacts the die during the forming step [5]. At this time, the heat transfer rate increases dramatically (on the order of 100°C per second) promoting the austenite to martensite transformation [19]. This rapid martensitic transformation increases the strength of the part which is one of the main goals of hot stamping. However, for some forming cases with tight bending radii or complex shapes, the martensitic transformation causes early hardening during forming which restricts further deformation leading to severe tool wear, or sometimes sheet metal failure. Therefore, the hot stamping procedure must be designed carefully.

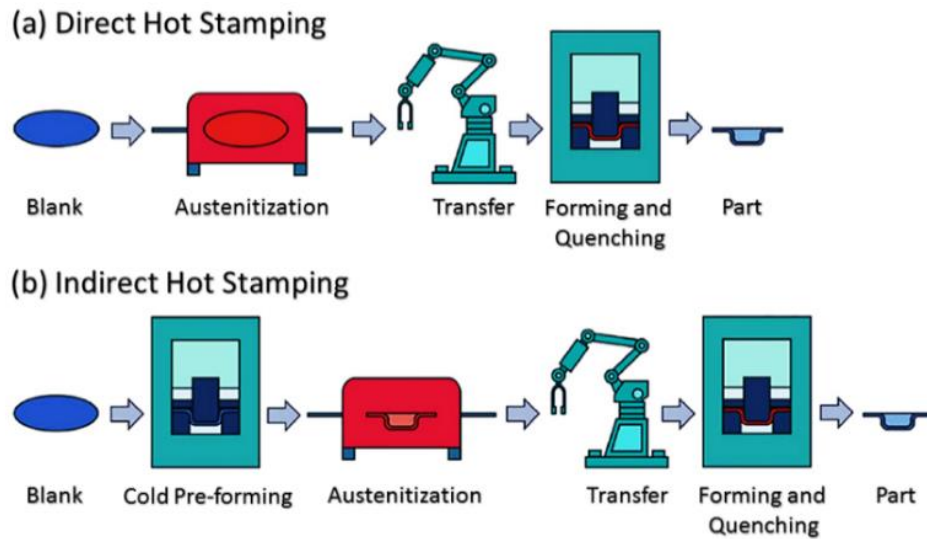


Figure 2-1. Illustration of (a) Direct hot stamping, (b) Indirect hot stamping processes [17].

The complex design and application of safety components has led to the development of hot stamped parts with tailored properties. In the tailoring approach, the manufactured sheet metal has functionally graded properties in different sections to improve the performance of the parts. In-die heating tailoring and tailor welded blanks (TWB) are recent approaches for performance improvement of PHS in the automotive industry. In-die heating was first introduced by ThyssenKrupp Steel AG to combine anti-intrusion properties and impact energy absorption capability within a single part [2]. In this tailored heating method, a pair of multi-zone heated dies is used to alter the quenching rate at different locations resulting in a microstructure gradient and corresponding range of final properties (Figure 2-2a). Tailor welded blanks are basically two or more different materials that are laser welded together and undergo the same quenching rate during hot stamping but ending up with different strength and ductility due to differences in their chemical composition (Figure 2-2b). The tailoring approach has gained much industrial attention due to the variety of materials and process combinations that can be used to achieve a range of properties in the same hot stamped part, such as rails, pillars, dash panels and floor cross members.

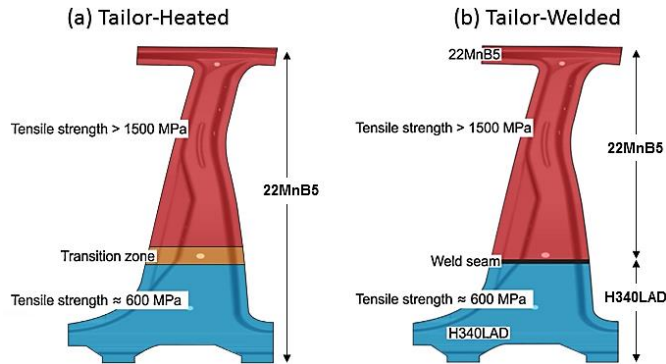


Figure 2-2. Schematic of a B-pillar made by (a) Tailor heated, and (b) Tailor welded hot stamping methods [20].

2.3 Resistance Spot Welding

Although the selection of hot stamped materials for automotive safety components provides excellent mechanical properties, the failure behavior of the joints that are used to assemble sheet metal parts also plays a vital role in the overall performance of the assembly. Resistance spot welding is the most commonly used joining technique for automotive assembly due to its flexibility and rapid production rate. According to Vural *et al.* [21] the performance and durability of a vehicle is affected by the quality and mechanical properties of spot welds. Therefore, it is important to properly investigate the characteristics and mechanical properties of spot welds. RSW is a joining process for two or more sheets through resistive heat generation at discrete contact points [22]. An RSW setup (Figure 2-3) includes a pair of water-cooled electrodes, usually made of Cu alloys, installed on a pneumatic jaw [9]. In the first stage of the welding process (Figure 2-3a), the sheets are positioned between the electrodes. Then, the sheets are squeezed by the electrodes, maintaining a specified load until the end of the process (Figure 2-3b). Upon establishing an electrical flow between the two electrodes, the point of contact between the two sheets, having the maximum electrical resistance, heats by resistive, or Ohmic heating within a few milliseconds (Figure 2-3c). As soon as the temperature reaches the melting point of the material, an enclosed pool of molten metal is formed and begins to grow rapidly. Electrical current and welding time determines the size of the molten metal pool. At the end of the welding stage, heat dissipates from the molten metal pool to the surrounding material and toward the cold electrodes leading to rapid solidification of the molten pool (Figure 2-3c). The process forms a ovoid-shaped joint between the two sheets that is called the weld nugget [22].

The diameter of the weld nugget, known as the nugget size, is the most important characteristic of a spot weld. According to the American Welding Society (AWS) D8.1 standard for spot welds in automotive applications [23], a minimum nugget size of $4\sqrt{t}$, where t is the sheet thickness, is required for an acceptable spot weld. As a general rule, weld strength increases with increasing nugget diameter. However, nugget size and spot weld quality are controlled by a range of process and material parameters.

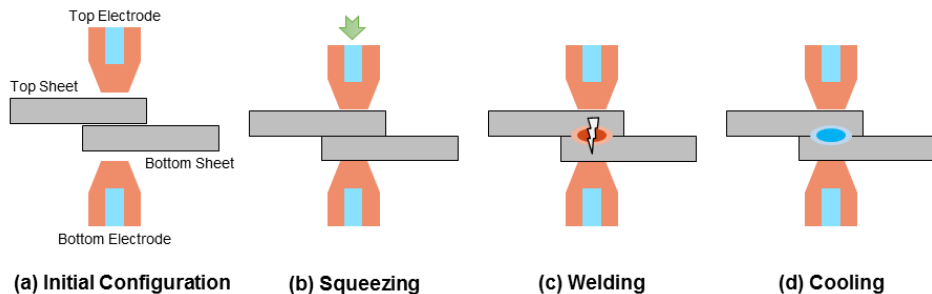


Figure 2-3. Resistance spot welding process (a) Initial configuration, (b) Squeezing, (c) Welding, and (d) Cooling.

2.3.1 Process Parameters of RSW

Welding current, time, and electrode force are the most important process parameters in RSW. The welding current facilitates heat generation through Joule heating (the higher the resistance the more heat is generated) [9]. Figure 2-4 shows the schematic distribution of resistance and resultant temperature during the initial stages of welding. The majority of the heat is generated at the location of highest resistance at the sheet-to-sheet interface (point 4 in Figure 2-4), however, there are four other major resistance sites along the current path [24]. The electrode-to-sheet interfaces (points 2 and 6) have a contact resistance that is lower than the sheet-to-sheet interface since the copper electrodes are softer with fewer asperities at the interface. Typically, the bulk resistance of the copper electrodes which is about $1.5 \times 10^{-8} \Omega \cdot m$ (1 and 7) is considered negligible compared to the bulk resistance of the steel sheets (about $1.4 \times 10^{-7} \Omega \cdot m$), shown as 3 and 5 in Figure 2-4. It was shown that electrical resistance increases dynamically as temperature increases at the contact point which increases the rate of heat generation over time [9]. Longer welding time generates more heat; therefore, a larger nugget is obtained. The electrode force also contributes to nugget size by affecting the contact resistance. A high electrode force results in lower contact resistance by flattening the micro-asperities on the material surface (higher contact areas); thus, current density is lowered and less heat is generated [25].

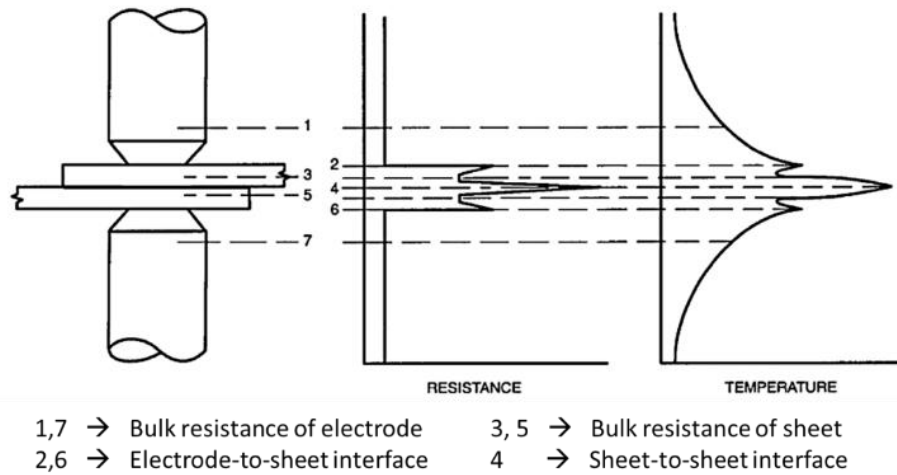


Figure 2-4. Schematic trend of electrical resistance and corresponding temperature as a function of distance [26].

Hold time is another process parameter referring to the time duration (dwell) between the moment when current is terminated and when the electrodes are retracted. The majority of the weld cooling occurs during the hold time. The duration of hold time should be long enough to allow rapid heat dissipation from molten metal zone (toward the water-cooled electrodes) so the weld solidifies before electrode release [27]. In special cases, including joining sheets with different thicknesses or coatings, pre-pulsing and post-tempering current pulses are introduced for material surface and weld nugget heat treatment, respectively [28].

The range over which the main process parameters result in an acceptable nugget size is defined by the weld lobe. A typical weld lobe is shown in Figure 2-5 in which the lines determine the upper and lower bound for current and time combinations resulting in an “acceptable weld”. The lower bound is defined by combinations of welding time and current resulting in a nugget size equal to or larger than $4\sqrt{t}$ as prescribed by AWS D8.1 [23]. In general, overly low current and/or low welding time will lead to an unacceptable weld or even no nugget [29]. The upper limit of the welding lobe is defined by onset of “expulsion” which is the ejection of molten metal from the nugget due to growth of the molten nugget beyond the diameter of the clamped material [29]. Expulsion occurs when welding time and/or current are relatively high. The volume of molten metal and the expansion pressure becomes excessive; consequently, the extra volume of molten metal cannot be kept in place and drifts out. Pouranvari *et al.* [30] and Nikoosohbat *et al.* [31] showed that expulsion deteriorates the mechanical properties of spot welds (will be discussed later) and, therefore, should be avoided.

Kaiser *et al.* [32] also noted that the welding lobe boundaries can be adjusted by electrode force. Using a low electrode force increases contact resistance and reduces the retention pressure on the molten metal, thereby promoting expulsion [9,25]. On the other hand, a high electrode force lowers the current density, resulting in a smaller nugget size, but increases the retention pressure (confining expulsion) and helps the nugget to compensate for shrinkage cavities and pores after cooling [33]. Despite the notable effect of electrode force on the nugget size, a typical welding lobe usually does not take into account the effect of electrode force.

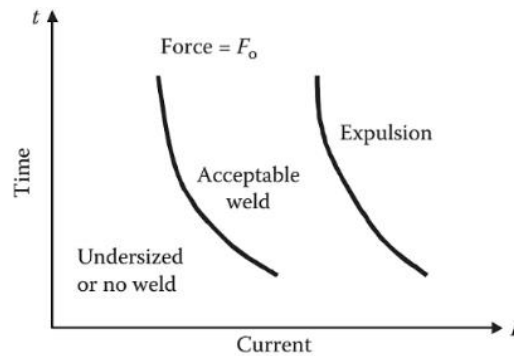


Figure 2-5. A typical welding lobe showing the boundaries and constraints for process welding parameters [9].

2.3.2 Material Parameters

In addition to the process parameters, there are a few important factors associated with material properties and specifications that affect nugget size in spot welds. The strength of the materials, thickness of the sheets, type of coating, and electrode diameter are the most influential factors in this context. Uijl *et al.* [34] showed that as the strength of the sheets increases, indentation resistance increases which may result in low weldability and hot cracking in severe conditions. On the other hand, softer materials tend to deform easier under the electrode force making full contact with each other [35]. As mentioned earlier, the minimum nugget size for an acceptable spot weld is a function of material thickness; therefore, as thickness increases, higher current and/or time are required. From a material point of view, different thicknesses also alter the rate of heat dissipation that should be compensated for by adjusting heat input [36].

Ighodaro [37] showed that welding current requirements for RSW are affected by the difference in electrical resistance associated with coating characteristics such as coating type and thickness. The last, but not least, important factor is the electrode diameter which determines the contact area in

RSW. The diameter of the electrode determines the current density during welding and also the post-weld cooling rate for the weld nugget [9]. Other material characteristics such as chemical composition, liquidus and solidus temperature, and thermo-electrical properties of the sheets also are important factors in determining weld size [35].

2.4 Microstructure of Spot Welds

Heat generation during RSW affects the microstructure of the steel through different phase transformations and resulting microstructure evolution. Figure 2-6 illustrates the cross-sectional view of a weld nugget with the corresponding peak temperature profile and microstructure. The fusion zone (FZ) is the solidified molten metal pool which reaches the melting temperature (T_m) of the material during RSW. The heat affected zone (HAZ) is the material surrounding the FZ that undergoes solid state microstructural evolution due to its proximity to the FZ. The peak temperature in the HAZ is just below T_m at the FZ/HAZ boundary (the red oval in Figure 2-6) and gradually decreases towards the base metal (BM). Due to the temperature gradient, different configurations and micro-constituents are expected within the microstructure of the spot weld. The corresponding microstructure of a DP600 steel is also shown in Figure 2-6. Both the FZ and HAZ consist of martensite, although the HAZ structure is much finer due to the difference in temperature and cooling rate regimes [38].

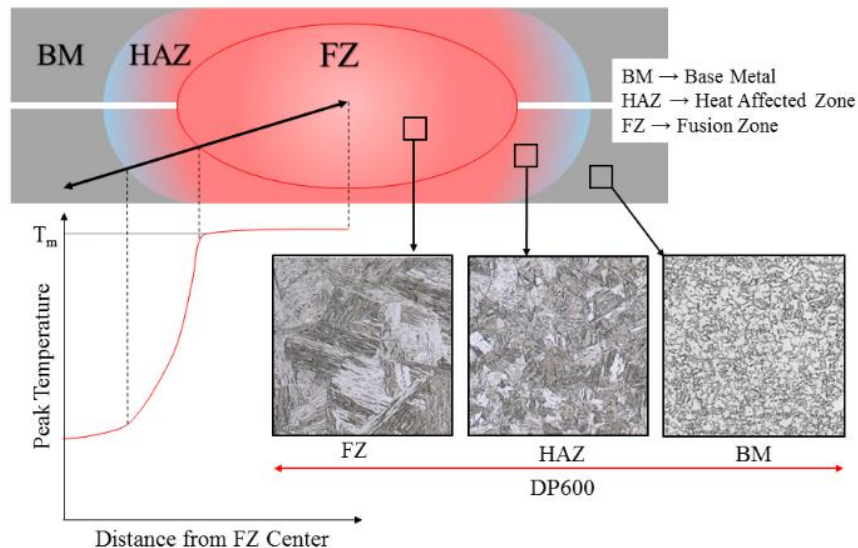


Figure 2-6. A schematic illustration of different zones in a typical spot weld cross-section, corresponding peak temperatures and an example of microstructure for a DP600 steel. Based on [9,38]

Figure 2-7a shows the correlation between peak temperature gradient in the HAZ and Fe-C phase diagram [39]. Four sub-zones can be identified within the HAZ. The temperature in the region surrounding the FZ does not reach T_m but it is high enough to promote rapid grain growth; thus, it is called the coarse grained-HAZ (CG-HAZ). For a typical high-strength low-alloy (HSLA) steel the peak temperature in CG-HAZ is above 1100 °C, which includes the δ -ferrite and upper half of the austenitic region [40]. Figure 2-7b shows an electron micrograph of the CG-HAZ in a martensitic MS1200 steel, consisting of large martensite packets formed during rapid cooling of the initial coarse austenite grains [41]. In the lower half of the austenitic region (Figure 2-7a), where the peak temperature is lower than 1100 °C but still above the A_{c3} (Austenite finish temperature during heating), the austenite grains undergo recrystallization resulting in grain refinement [42]. Therefore, this sub-zone is known as the fine grained-HAZ (FG-HAZ). Figure 2-7c shows an example of an FG-HAZ microstructure for MS1200 steel. Based on Figure 2-7, the typical microstructure where peak temperature reaches between the A_{c3} and A_{c1} (Austenite start temperature during heating) is a mixture of ferrite and austenite, known as the inter-critical HAZ (IC-HAZ). The type and fraction of micro-constituents in the IC-HAZ strongly depend on initial microstructure of the base metal and can be complex. For instance, a martensitic steel would have a mixture of partially transformed austenite (which retransforms to martensite upon rapid cooling and known as secondary martensite) and tempered martensite. An example of a microstructure taken from the IC-HAZ is shown Figure 2-7d for the MS1200 steel showing the martensite and ferrite [41].

The region surrounding the IC-HAZ (Figure 2-7a) is expected to undergo a peak temperature between A_{c1} and a minimum temperature required for decomposition of martensite (~400 °C). This low temperature region is known as the sub-critical HAZ (SC-HAZ), and for a martensitic steel such as a PHS, it consists of tempered martensite (or chemically decomposed initial martensite) [40]. In this region, the temperature is favorable for long-range diffusion of interstitial solute atoms resulting in a broken appearance of martensite laths and sub-micron carbide precipitations [43,44]. The broken appearance of the martensite laths after tempering is shown in the high magnification micrograph of the SC-HAZ for MS1200 in Figure 2-7e [41]. Saha *et al.* [45] and Jong *et al.* [8] showed that temperature history and chemical composition determines the micro-constituent type, distribution, and properties within the different regions of the HAZ. Considering the abundance of spot welds in automotive applications, understanding the relationship between mechanical properties and the microstructure of the spot welds is vital.

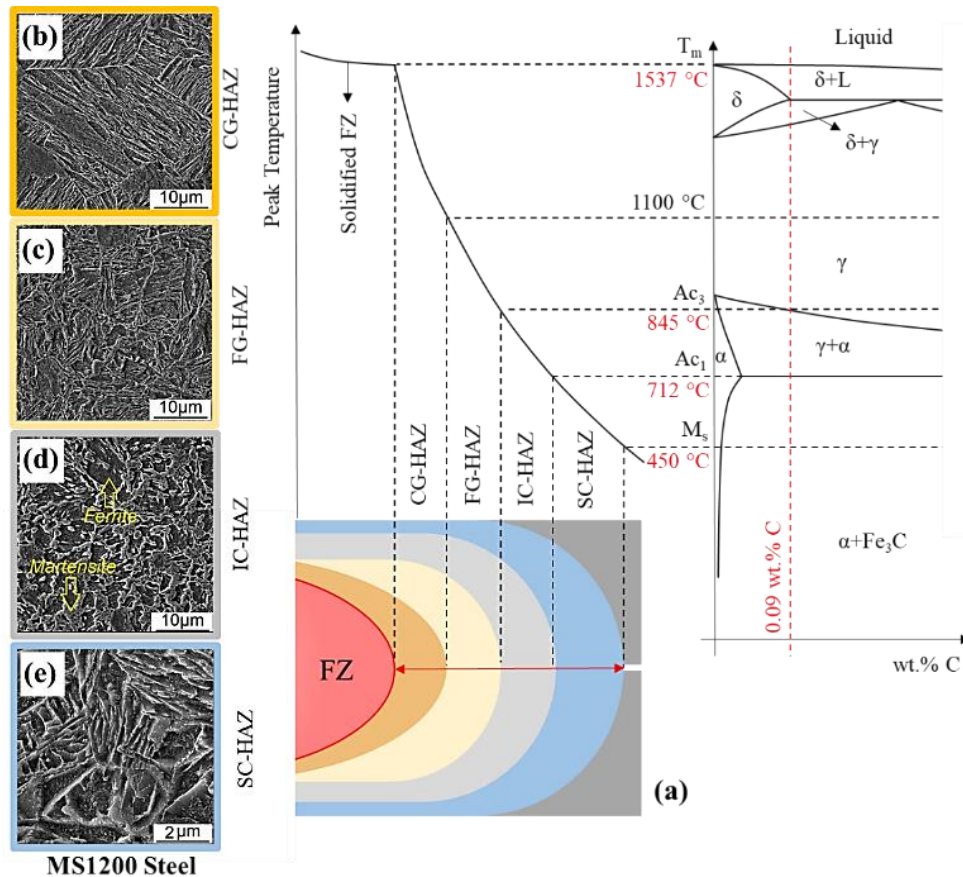


Figure 2-7. (a) The typical temperature gradient in HAZ of spot weld and sub-categories, and (b) to (e) corresponding room temperature microstructure for MS1200 Martensitic steel (0.09 wt.%C) (Based on [39,41])

2.5 Mechanical Properties of Spot Welds

Spot welds are subjected to complex loading conditions including shear, normal, torsion, and any combination of these major loading conditions. In practice, mechanical properties of spot welds are typically evaluated under shear and normal loading, which are defined with respect to the relative direction of load to the length of the sheets [46]. The Tensile-Shear (TS) and Cross-Tension (CT) tests are the most common techniques for evaluating the strength of spot welds in shear and normal loading under quasi-static conditions. In order to evaluate the dynamic performance of spot welds, complex fatigue and impact tests are usually conducted. Quasi-static tests are normally used for fundamental studies due to ease of load application [47]. Test coupons for the TS and CT tests are made using a lap-joint configuration and then pulled such that the weld is loaded primarily in shear (TS) or normal to the weld (or sheet) surface (CT).

Figure 2-8 shows the TS and CT test specimens, schematically. In the TS test (Figure 2-8a), the load is applied parallel to the sheets, causing a global tensile stress in the sheets, and a shear dominant load on the spot weld. The loading condition is initially uniaxial; however, the weld nugget rotates due to the moment induced by off-plane loading [40]. This also changes the loading condition from shear to a combination of shear and tension upon failure (Figure 2-8a). Therefore, typical stress and strain measurements cannot be done for spot welds due to the transient state of loading and the complex load-bearing area within the weld nugget geometry. The out-of-plane rotation is usually inevitable in the TS test due to the asymmetrical loads applied to the sheet in the lap configuration. However, the extent of rotation is usually less extensive for higher strength martensitic materials such as MS1400 and as-hot-stamped 22MnB5 steels [40,41] and can be minimized by shimming the grip regions to equal thickness.

In the CT test (Figure 2-8b), the resistance of weld nugget to “opening” is evaluated. Although the loading direction is initially normal to the sheets, the loading condition may not remain constant during the CT test, depending on the strength and ductility of the base metal which causes the steel sheets to bend (Figure 2-8b). Due to the bending in the BM, the load can impose a shear component on the spot weld which makes the failure behavior of the spot weld quite complex. This complexity is one of the key issues associated with the CT test, especially for ductile materials which are expected to undergo greater bending. Radakovic and Tumuluru [48] showed that failure in CT testing can be due to either brittle fracture of the nugget or shear overload in the HAZ; the failure mode becomes dependent on the sheet thickness and strength and ductility of the base metal and HAZ.

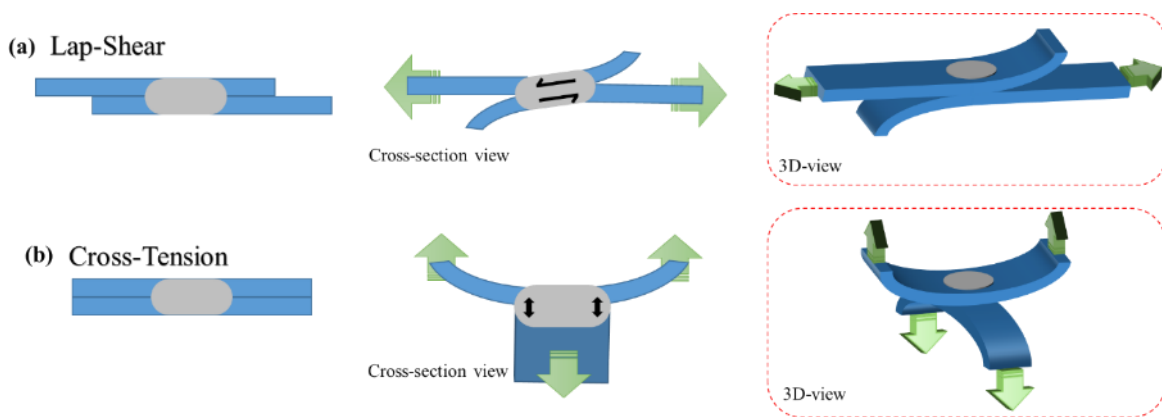


Figure 2-8. The schematic illustration of different loading conditions for evaluating mechanical properties of spot welds (a) lap-shear test and (b) cross-tension test (based on [47]).

To minimize out-of-plane rotation in the TS test and the bending issue in the CT test, more constrained testing geometries such as KSII [49,50] and H-shaped samples [51] are utilized in addition to or instead of standard tests. Figure 2-9a shows the KSII test specimen with the weld located at the center of the mating surfaces which can be used for normal, shear, or combined loading conditions based on its angle to the load during testing. The 90° KSII test puts the spot weld under normal load similar to CT while the 0° KSII applies a shear load similar to tensile-shear test discussed above. The KSII benefits from its U-shaped coupons and tight clearance when bolted to the test fixture which minimizes the out-of-plane rotation under shear and BM bending under normal loading [49]. Although KSII testing appears more robust in terms of controlling the loading condition, one may find the fabrication of the test specimen and the fixture required to rotate the samples between 0 to 90° challenging especially when dealing with less ductile materials such as martensitic steel with low ductility [52]. In addition, the geometrical constraints in the KSII test may be sometimes too extreme when compared with spot welds in actual loading conditions [53]. Therefore, KSII is typically not considered to be a replacement for standard lap-shear and cross-tension test. Figure 2-9b also shows how the H-shaped test samples can be used to test a group of spot welds under shear and normal (peeling) conditions. The H-shaped test samples, which consist of 5 spot welds on each side of the joint for a total of 10, provide improved correspondence to real loading conditions for automotive spot welded structures.

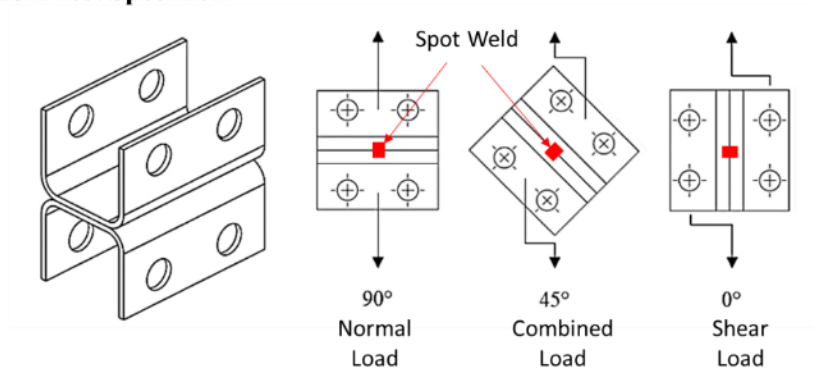
The AWS D8.1M [23] standard specifies minimum performance levels in terms of strength during CT and ST testing; these are calculated (in kN) using Eq. (1) and (2), respectively:

$$CT_{\min} = 1.25t^{2.2} \quad (1)$$

$$TS_{\min} = \frac{(-6.36 \times 10^{-7} \times S^2 + 6.58 \times 10^{-4} \times S + 1.674) \times S \times 4 \times t^{1.5}}{1000} \quad (2)$$

where S is the base metal tensile strength (MPa) and t is the thickness of a single sheet (mm). The minimum strength criterion shows that for a higher material strength and thickness, a larger value for TS strength is required, however, the required CT strength is not affected by the strength of the base material, only the thickness.

(a) KSII Test Specimen



(b) H-shaped Test Specimen

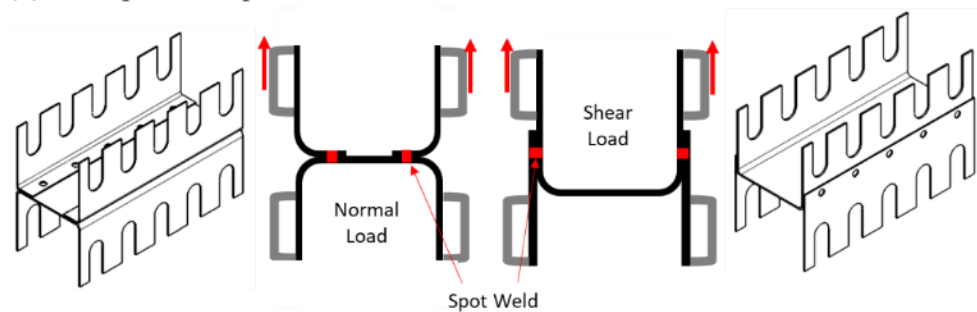


Figure 2-9. Schematic illustration of (a) KSII test specimen and testing configurations for different loading conditions (adopted from Tolton [49]), and (b) H-shaped test specimens according to SEP 1220-p2 European standard [51] (the iso-view images of the H-shaped samples were adopted from Heidrich *et al.* [54]).

The TS and CT tests are characterized in terms of the measured load vs. displacement, as shown in Figure 2-10. The strength of a spot weld is usually expressed in terms of the peak load. However, the amount of absorbed energy (area below the curve up to the failure) and displacement at the peak load (maximum displacement) are also important [55]. Peak load is generally higher for a larger weld nugget. However, weld defects such as expulsion and formation of voids are more likely to occur in over-sized weld nuggets which generally degrade the mechanical properties of spot welds [9]. Sun *et al.* [56] showed that excessive indentation and significant metal loss occur due to heavy expulsion in oversized nuggets in DP800 and TRIP800. The corresponding TS results showed only a slight increase in peak load and absorbed energy, despite a 30% increase in nugget size. Pouranvari *et al.* [30] reported that expulsion would only affect energy absorption capacity of weld nuggets in Fe-0.045C-0.189Mn steel by changing failure location associated with excessive indentation, but does not affect peak load.

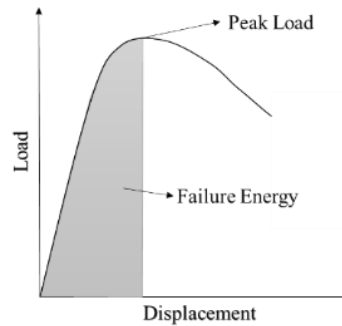


Figure 2-10. Typical load vs. displacement curve obtained from quasi-static LS and CT tests (based on [55]).

2.6 Failure Characterization of Spot Weld

In addition to the measured load-displacement curves, the failure behavior of spot welds can be qualitatively characterized by examining post-failure spot welds at macro and micro scales. The overall macroscopic shape of the failed spot weld is used to classify the failure mode which provides important information regarding the failure behavior of the spot weld. In addition, the failure path and microscopic location failure can be examined using metallography techniques. Due to the heterogeneous properties of the nugget, the failure behavior of spot welds can be only evaluated destructively using the standard TS and CT tests (as well as the KSII and H-shaped specimens, for example). This assessment is usually done by examining the final state of the weld nugget after failure or by several interrupted tests. However, the information obtained from typical destructive methods are limited considering that damage accumulation and crack propagation occurs in an enclosed space around the weld nugget. Nevertheless, spot weld failure can be determined and categorized to some extent based on post-failure observations. The failure modes and the relationship between microstructure and failure behavior of spot welds are discussed the following sections.

2.6.1 Spot Weld Failure Modes

Failure location, crack propagation path and overall shape of the joint after complete separation provide additional understanding of spot weld failure. Failure mode is a qualitative measure of the mechanical properties of spot welds and can be taken as an indication of the load carrying capacity and energy absorption of the weld. Figure 2-11 shows the various types of failure modes that can occur during mechanical testing of spot welds. Figure 2-11 a shows the interfacial failure (IF) mode in which failure occurs along the interface of the sheets and propagates through the FZ. A smaller fusion

area, due to small nugget size and defects such as expulsion and shrinkage voids, promote the IF mode; therefore, IF is frequently cited as an undesirable failure mode in the published literature [57]. Figure 2-11b shows pull-out failure (PF), in which the weld nugget is pulled out of one sheet (through-thickness failure) and remains as a button on the other side. PF is the most common type of failure in ductile materials and is often viewed as indicating satisfactory mechanical properties [9].

Both IF and PF can occur partially meaning that a transition between these two failure modes is possible as failure proceeds. Figure 2-11c and d show schematics of partial IF (PIF) and partial PF (PPF) modes, respectively. In these cases, failure starts in either an interfacial or through-thickness mode and then transitions to the other mode until complete fracture [47]. The major difference between PIF and PPF is that failure initiates interfacially for the PIF but through-thickness fracture is dominant in the PPF which both turn into button pull-out afterwards. Neither of these failure modes can be precisely predicted due to the complex effect of weld geometry, loading condition and microstructural factors involved in dynamic failure mode transition. Figure 2-11e shows a double pull-out failure (DPF) that is similar to PF but in this case, the nugget is detached from both sides. DPF is observed in martensitic steels with a wide HAZ [58]. DPF is not a standard failure mode in the literature; however, it was encountered frequently in the present work.

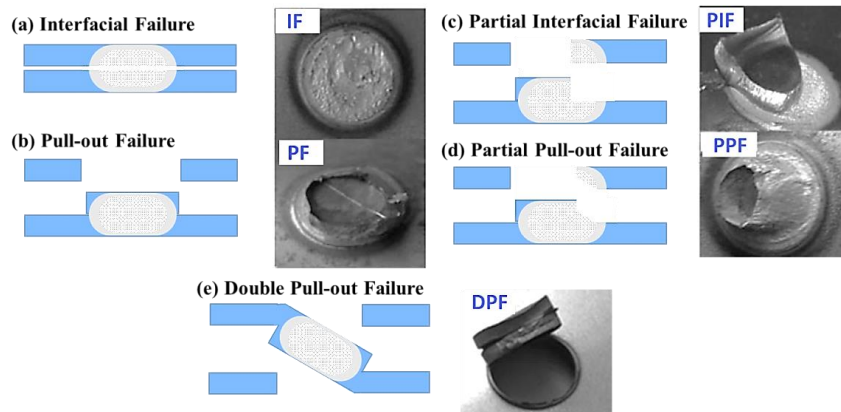


Figure 2-11. Schematic representation of failure modes in spot weld and corresponding examples of fracture surfaces for different failure modes (based on [47,58]).

From the point of view of mechanical properties, failure modes strongly depend on weld nugget size. According to Pouranvari *et al.* [59], the transition from interfacial to pull-out failure occurs when the FZ is larger than a critical value. Therefore, a minimum nugget size is required to ensure that spot welds fail in pull-out mode under shear-tension. However, Sun *et al.* [56] showed that the common criterion of $4\sqrt{t}$ for the minimum nugget size (as prescribed by AWS D8.1 [23]) does not guarantee

PF mode in high strength materials such as DP800 and TRIP800. In other research by Pouranvari *et al.* [60] it was shown that the critical nugget diameter for IF to PF transition (D_c) is not the same value for all materials with identical thicknesses (*e.g.* 1.5 mm in Figure 2-12). In addition, no clear relationship between the peak load and D_c could be established in that work.

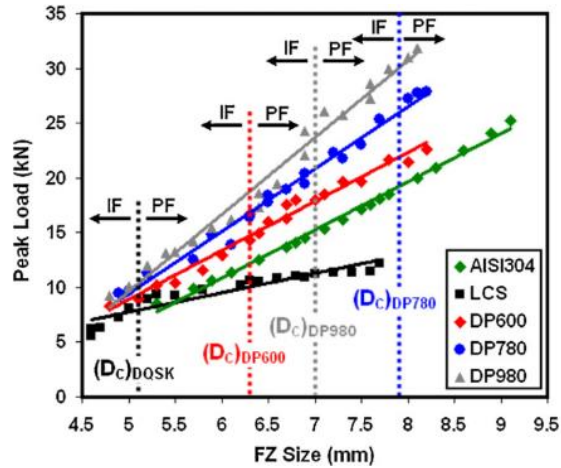


Figure 2-12. Effect of weld nugget size on the failure mode and peak load [60].

Figure 2-13 shows the typical shapes of the load-displacement curves for spot welds under shear-tension loading for both IF and PF modes. The peak load and the amount of absorbed energy for welds failing in the PF mode is usually much higher than those failing in the IF mode. Also, the failure occurs at lower displacement in IF, representing a more brittle type of fracture [61]. It is important to note that peak load and amount of absorbed energy are functions of nugget diameter so that larger welds are more likely to fail in PF mode and tend to be stronger (neglecting other geometrical and material-related factors). The load-displacement behavior of PPF and PIF are not easy to predict because fracture is a mix of IF and PF and each may dominate the failure based on the weld characteristics. However, the load-displacement curve is reported to be close to the curve for PF for martensitic steels [41]. Note that failure characteristics are not only affected by material properties, weld nugget geometry and loading direction, but also depend on loading speed. Song *et al.* [62] performed numerous ST tests to investigate the effect of loading rate on failure behavior of spot welds. The results showed that spot weld failure modes are not affected by test speed, but peak loads are significantly higher in dynamic loading.

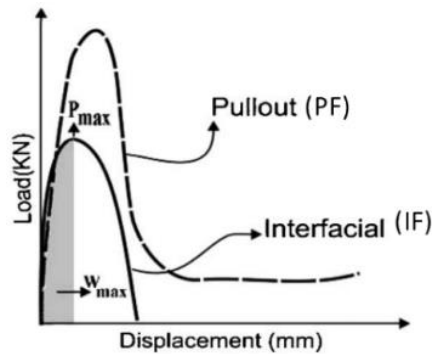


Figure 2-13. Typical load-displacement curves for IF and PF modes under shear-tension load [61].

2.6.2 Effect of Microstructure in Spot Weld Failure

In addition to the loading conditions and geometrical factors, characteristics of the BM, FZ, and HAZ play an important role in mechanical properties and failure behavior of spot welds. The properties of different regions within a spot weld are usually evaluated by hardness measurement, which is a good indicator of local strength of the material. Typically, the FZ is usually the hardest region within the weld due to the extremely high cooling rate in the FZ that promotes martensitic transformation. For example, Tamizi *et al.* [58] showed that the cooling rate in the FZ is so high that its hardness is actually independent of the welding parameters and heat input so that a constant hardness value is obtained for the FZ in a martensitic MS1400 steel. Therefore, the FZ can be treated as a rigid section and it is reported that the FZ affects the strength of spot welds only when defects such as voids and excessive indentation are present [37].

The BM contributes to resistance spot weld failure of ductile materials in regions where it is softer than both the FZ and HAZ. This effect is particularly prominent for low-carbon steels with high martensite hardenability [63]. Dancette *et al.* [64] reported similar results for DP450 automotive steel (Figure 2-14). According to hardness profile measurements (Figure 2-14a), the relatively high hardness in the FZ is due to rapid cooling and martensite formation. Transformation of austenite to martensite during cooling in the CG-HAZ and FG-HAZ, and formation of martensite from partially transformed austenite in the IC-HAZ increases the hardness in the different regions of the HAZ. However, the BM does not show any noticeable changes due to the minor changes in temperature that it is exposed to, making it the softest area within the spot weld. As expected, failure occurs in the BM or HAZ/SC-HAZ for DP450 due to the significantly lower strength of the BM (Figure 2-14b).

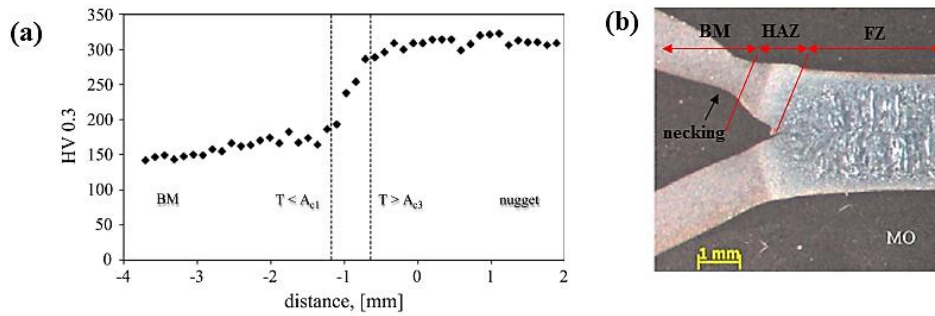


Figure 2-14. (a) Hardness profile of weld nugget and (b) microstructure after failure for DP450 [64].

Ordoñez Lara *et al.* [65] showed that spot welds in high strength steels have a different hardness distribution and microstructural configuration (Figure 2-15). Comparison between microhardness profiles for DP590 and DP980 (Figure 2-15a and b) show that the BM is not the weakest zone in DP980. The corresponding micrographs of HAZ and BM (Figure 2-15c and d) show that the hardness of the BM in DP980 is higher due to a higher amount of martensite. Although the HAZ has undergone a similar thermal cycle in both materials, HAZ softening is more prominent in DP980 due to extensive martensite tempering. Pouranvari *et al.* [41] and Tamizi *et al.* [58] also reported similar results for MS1200 and MS1400 martensitic steels, respectively. HAZ softening due to martensite tempering is also reported for hot-stamped steels in which the average hardness values of the BM and FZ are almost the same [8]. Therefore, spot welds made for BMs with relatively high fraction of martensite typically tend to fail in the HAZ due to HAZ softening [66,67].

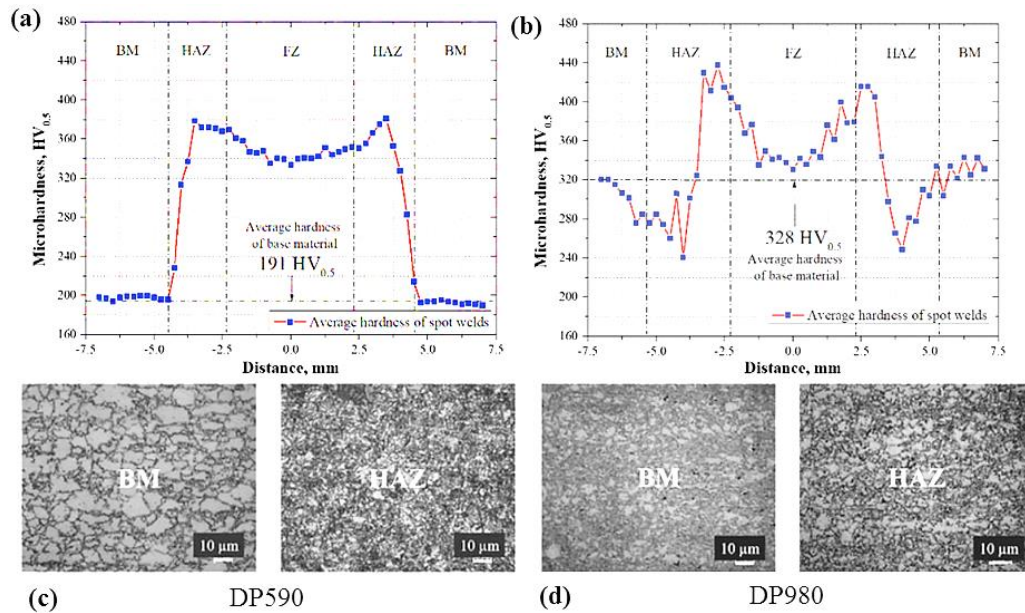


Figure 2-15. Microhardness profile and microstructures for spot welds of the same size in (a) and (c) DP590 and (b) and (d) DP980 [65].

In general, for materials with medium to high martensite content, the PF mode is typically associated with HAZ softening and the PF occurs in the BM when weld region is relatively harder than the BM. In addition, the PF mode is reported for fully martensitic MS1400 [66] and PHS [68] due to failure at the interface of FZ and HAZ. However, crack propagation and the mechanism of failure at the interface of the FZ and HAZ is still not fully understood. In a recent paper by Sherepenko *et al.* [69] the presence of a transient softened zone at the fusion boundary was identified as the main reason for failure at the interface of the FZ and HAZ in 22MnB5 steel. However, the failure propagation and mechanisms were not elaborated.

In addition to local material properties, the spot weld failure mode strongly depends on the loading condition, *e.g.* shear, normal or mixed loading. Studies show that the PF mode is most likely to occur under normal load but it is also a common failure mode under shear load for steels with a soft BM or softened HAZ region [60,66]. On the other hand, the IF mode has been observed in fully or partially martensitic steels, such as PHS grades, when the weld nugget is too small or the sheet metal is relatively thick ($>1.5\text{mm}$) [68]. It is worth mentioning that IF is also more probable for welds with expulsion and/or solidification voids in the vicinity of the HAZ [70]. However, it is reported that a fully martensitic microstructure in the FZ and HAZ (near the fusion boundary) allows easier propagation of cracks into the FZ, promoting an IF mode [47,71]. Despite the very detailed reports on

requirements for IF to PF transition for different grades of AHSS for automotive application, Pouranvari *et al.* [60] showed that there is no direct relationship between susceptibility to IF failure mode and the tensile strength of the BM. Therefore, the experimental analysis and prediction of failure in spot welds is very challenging. There are several other reasons that makes both qualitative and quantitative failure analysis of spot welds substantially difficult. One is the inability to image the interior of the spot weld during testing to record the failure phenomena. Failure in spot welds occurs within the enclosed volume of material between the two sheets; therefore, there is no practical way for *in-situ* failure characterization except state-of-the-art characterization methods such as x-ray tomography [72]. The other challenge is the variability of spot weld failure due to complex loading conditions around the weld nugget and statistical variation associated with the welding process itself, which makes it quite hard to obtain the same result for every interrupted test. Thus, a practical method for *in-situ* observation of spot weld failure is needed.

2.7 Characterization Methods for Local Material Properties

As discussed above, microstructural characterization of spot welds is essential for qualitative analysis of failure. However, quantitative analysis of spot weld failure is also required to enable numerical modeling of damage progression and failure prediction, which is usually performed by measuring local material properties of different weld regions. Local material properties of spot welds, such as flow stress curves and fracture strains, are typically measured using direct or indirect measurement techniques. The direct method uses the actual (or partially machined parts of the) spot weld to measure the local mechanical properties; while for the indirect method, the BM is heat treated separately to simulate the spot weld material which is then subjected to typical sheet metal characterization methods. As was mentioned earlier, both qualitative and quantitative failure characterization of spot welds are a quite challenging due to the complex loading conditions around the weld and limited accessibility for *in-situ* analysis of spot weld failure. For the same reason, the measurement of local material properties for different regions of spot weld can be difficult, as discussed in the following sections.

2.7.1 Direct methods

The majority of the direct methods for local material property measurement use spot welded test samples and correlate the strain fields on the surface with the onset of spot weld failure. The most convenient measuring technique is a combination of modified mechanical test samples extracted from

the spot welded coupons coupled with Digital Image Correlation (DIC) technique [52,73] for local strain measurement. Tao *et al.* [74] directly measured the flow stresses for different regions within spot welds for a DP600 steel by extracting small shear samples consisting of different sections of a spot weld. They used DIC technique to capture deformation images and measure local strain on speckled patterns on the surface of the sample. A similar method was used by Tong *et al.* [74] to characterize the tensile flow behavior beyond diffuse necking by using miniaturized samples with 1 mm gauge-length extracted from the actual spot welds in a dual-phase steel (shown in Figure 2-16). Although the abovementioned methods for direct measurement of local material properties for spot welds have shown good agreement with experiments, the examined flow behavior is unique to that particular weld since the results strongly depend on the weld size and thickness of the sheets. In addition, fracture characterization of different weld regions, such as fracture strains at various stress states, are not addressed by the aforementioned studies.

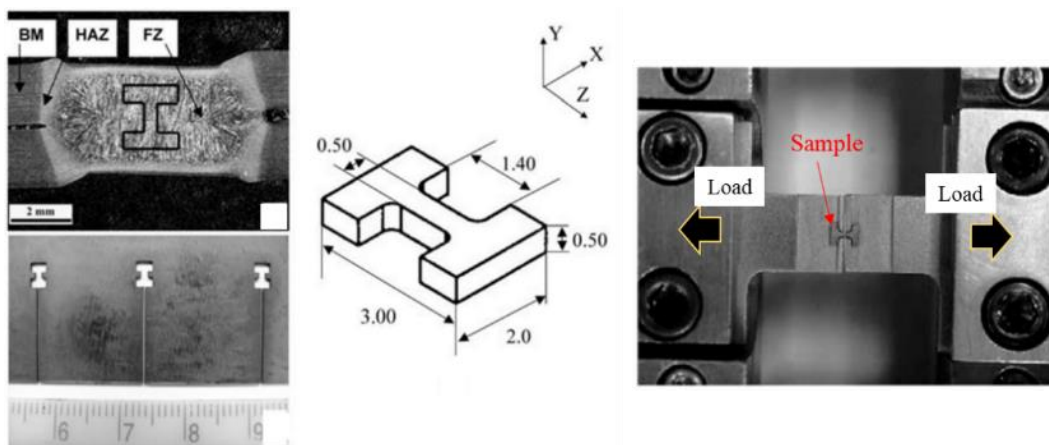


Figure 2-16. Sample preparation for miniaturized tensile test used by Tong *et al.* [75] for direct measurement of local material properties

Eller *et al.* [76] used an inverse FEA modeling approach to calibrate the Bai-Wierzbicki fracture model [77] based on asymmetric uniaxial tensile tests which consist the actual weld. These tests included but were not limited to partially machined and central hole tensile and bending tests in which off-centered load was applied next to the spot weld region. The calibrated fracture criterion was used along with constitutive flow models to predict failure in spot welds for 22MnB5 steel; however, the amounts of experimental work and inverse simulation runs required for the fracture model calibration were exceptionally high and unlikely to be applicable to different spot welds. Close-to-reality behavior of materials and relatively easy calibration of constitutive models and

fracture criteria are the most notable advantages of direct methods for measuring local material properties for spot welds. However, the data from direct methods are exclusive to the specific loading condition, only represent failure on the surface, and cannot be used to predict different failure modes. The direct measurement of local material properties is also used to confirm strain localization at the HAZ or the predicted location of failure. Ghassemi-Armaki *et al.* [78] measured fracture strains associated with failure at the HAZ for hot-stamped 22MnB5 spot welds. As shown in Figure 2-17a, the major strain field was only measured on the surface of the weld with the assumption that it occurs at the HAZ. O’Keeffe [79] used 3D DIC technique to measure the strain fields on the surface of spot welded 22MnB5 samples under different loading conditions. The 3D DIC technique uses a pair of angled cameras pointing at the same area of interest enabling out-of-plane measurement of strain. Examples of equivalent strain fields measured by O’Keeffe [79] are shown in Figure 2-17 for lap-shear (shear loading) and plane strain v-bend tests in which the test sample has out-of-plane movements. However, the direct measurement of strain on the surface does not give insight into quantitative failure analysis or through-thickness damage progression for the spot weld.

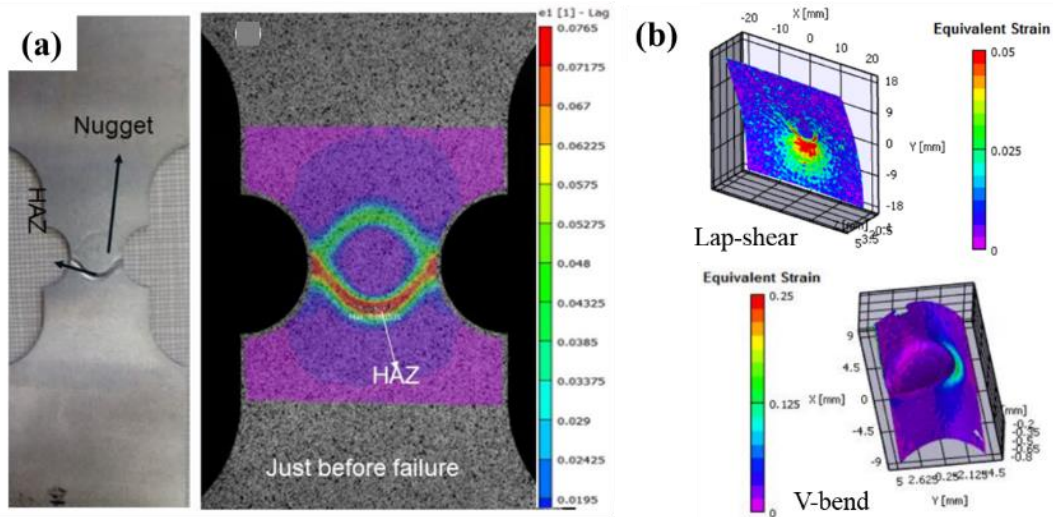


Figure 2-17. Strain field measurement on the surface of spot welded samples using DIC technique (a) notched tensile sample in Usibor®1500 steel [78], (b) 3D DIC results used for lap-shear and V-bend tests in Usibor®1500 steel [79].

2.7.2 Indirect Methods

The reproduction of spot weld material (including different subregions) via separate heat treatment is the one common aspect of all indirect methods for measuring local material properties of spot welds. Dancette *et al.* [80] used a commercial welding process simulator named SORPAS® to predict the

temperature history for different locations within the weld zone. Then, they reproduced the weld material using a Gleeble thermo-mechanical simulator to recreate the temperature history within relatively larger sheets, resulting in the same microstructure and hardness of the actual weld region. Using this approach, the constitutive flow behavior of spot welds in DP450 and DP980 were characterized in tension. Raath *et al.* [81] used the same approach to characterize the constitutive flow behavior of 22MnB5 steel but also performed a fundamental fracture characterization at various loading conditions. The material reproduction procedure used by Raath *et al.* [81] is shown in Figure 2-18. The welding process simulation provides the estimated temperature gradient (shown in Figure 2-18a and b). Using the target peak temperatures for each point of interest, several heating paths are simulated using the Gleeble apparatus (Figure 2-18c) until the microhardness and microstructures match with the original target. A similar technique was used by Paveebunvipak and Uthaisangskuk [82] to characterize flow behavior and fracture response of weld material in similar and dissimilar joints of high strength steels. They used the Representative Volume Element (RVE) modeling approach to establish a correlation between microstructure and local material properties of the FZ, HAZ and BM for different stack configurations. They observed a good correlation between the predictions and experiments.

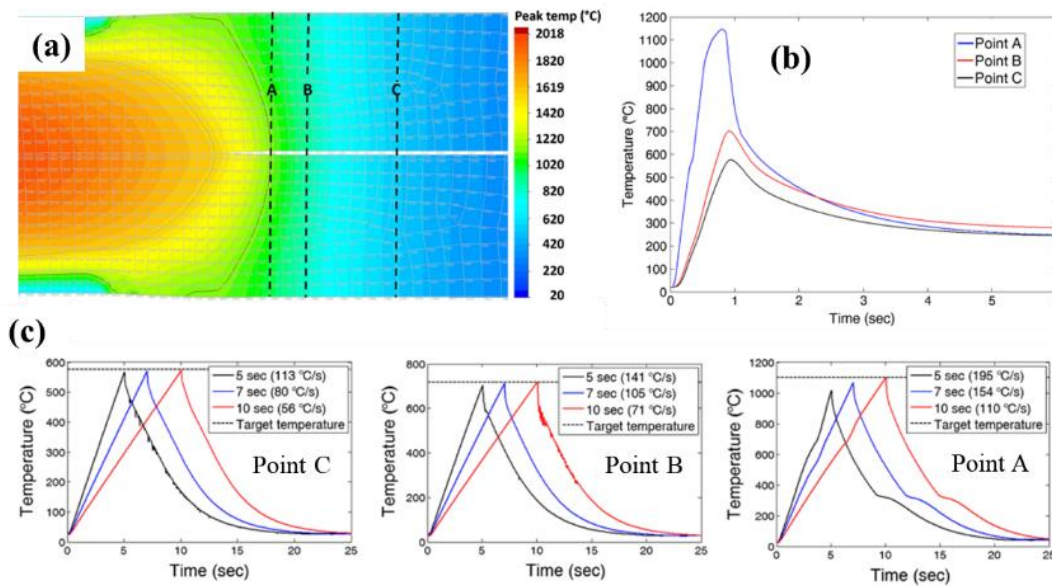


Figure 2-18. Example of spot weld material reproduction for indirect local material properties measurement used by Raath *et al.* [81]. (a) SORPAS® simulated temperature history, (b) extracted temperature history for the points of interest, (c) Gleeble simulated temperature history to achieve the target temperature.

In recent work by Ma *et al.* [83] a combined experimental and computational approach was used for failure analysis of spot welds in DP980 due to liquid metal embrittlement. The FZ was characterized directly by modified miniature tensile tests and the local properties of the HAZ were measured indirectly by reproducing similar material conditions. The reported results showed that the constitutive and fracture behavior of regions within the weld zone correlate with the predictions which show the sequence of failure and fracture path through the thickness of the pre-cracked sheets.

Based on the above-mentioned reports, the indirect measurement of local material properties is beneficial in terms of offering the flexibility to perform standard tests requiring coupons sizes larger than the weld zones on material with a microstructure similar to the individual weld zones. However, the constraints imposed by the adjacent regions, *e.g.* the FZ and upper-HAZ (U-HAZ), within the spot weld and the inevitable differences in temperature histories of the reproduced material and the actual weld material, may introduce a level of measurement error for the indirect method.

2.8 Numerical Modeling of Spot Weld Failure

Spot weld failure models are required to predict the performance of spot welds in computer-aided engineering (CAE) analysis of vehicle crashworthiness. For many years, the accuracy of the crash behavior of full-size assemblies has been limited by poor predictions of the failure behavior of spot welded structural connections [84,85].

The failure behavior of spot welds affects the performance of structural automotive components in terms of the ability of component-level joints to resist failure and/or absorb a significant amount of energy during failure. In conventional mild steels, the spot weld is often much stronger than the base metal, such that the spot weld appears rigid in nature. In contrast, spot weld and base metal strengths in ultra-high strength steels are much closer in magnitude. In addition, HAZ softening in such joints greatly complicates prediction of failure. Thus, accurate simulation of spot weld failure becomes essential to improve joint performance and structural crash crashworthiness [86].

2.8.1 Damage and Failure Analysis

Failure in metals occurs as a result of damage accumulation when the material is deformed under applied load or due to impact. From a microscopic viewpoint, damage progression leads to formation of micro-cracks or micro-voids which propagate or grow due to strain localization leading to macroscopic discontinuities better known as failure [87]. Failure in sheet metal forming analysis usually refers to onset of fracture, while in the context of spot weld failure analysis, physical

separation of the joint as the result of damage progression is the general definition of failure. However, the terms fracture and failure are often used interchangeably in this context.

Failure in metals occurs in a brittle or ductile manner. Figure 2-19 provides a schematic illustration of fracture types in a standard tensile sample and spot weld with respect to the identified failure modes. In standard tensile tests, a flat and faceted fracture surface with microscopic cleavage planes is an indication of brittle fracture which corresponds to the appearance of the sheet interface of a spot weld that failed in an IF mode. Brittle fracture in spot welds in high-strength DP980 and TRIP780 steels has been reported by Dancette *et al.* [64], Marya and Gayden [88] and Ma *et al.* [89]. Brittle fracture entails rapid crack propagation with limited plastic deformation and low energy absorption fracture promotes failure in the IF (or PIF) modes directly due to presence of martensite in the FZ. Ductile fracture, however, can be identified as a deformed fracture surface with microscopic dimples formed due to necking in standard tensile tests. This surface appearance is similar to that of spot welds failed in the PF mode, characterized by bent base metal and deformed edges around the nugget [9].

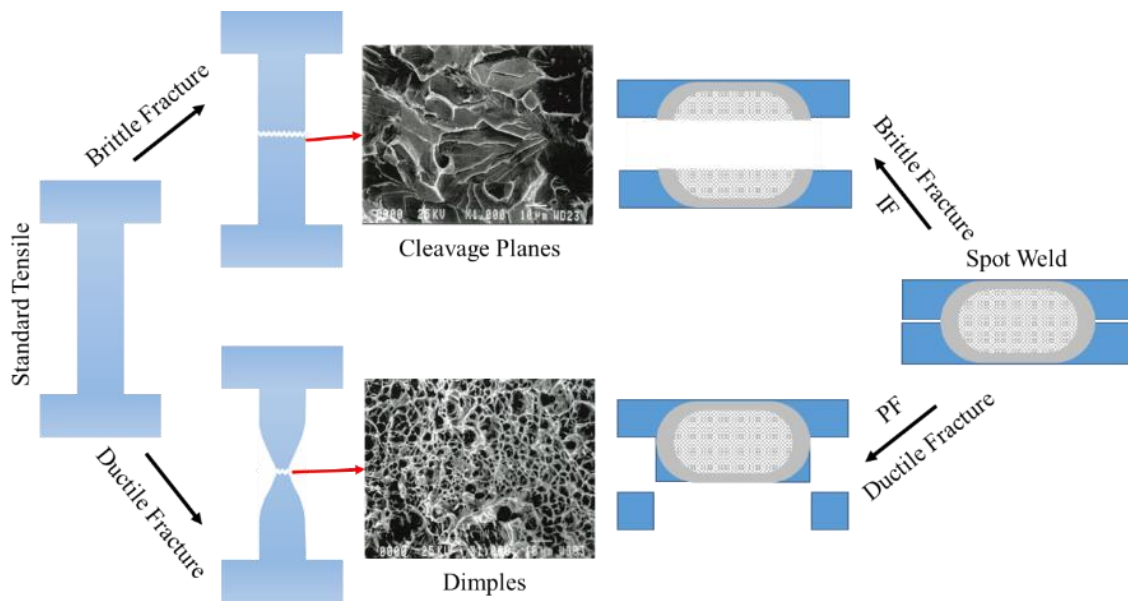


Figure 2-19. Different types of fracture in standard tensile samples and spot welds with respect to the identified failure modes in bulk metals (Fractographs adopted from [90]).

2.8.2 General Failure and Damage Modeling

For ductile fracture modeling of metals, there are two major modeling approaches: physical and phenomenological. From a microscopic viewpoint, a ductile fracture occurs by void formation, growth, and coalescence involving physical properties of micro-constituents, *e.g.* volume fraction, distribution, dislocation density, and grain size. Micromechanical damage models fall into this category. From a macroscopic point of view, ductile fracture is a phenomenon that involves empirical relationships of global motion and failure [87].

Micromechanical damage models are the most commonly used physical models for prediction of fracture. Stress localization at microstructural discontinuities such as second phase particles, inclusions and, pre-existing voids, is the basis of numerical analysis in micromechanics. Three sequential stages of damage evolution are considered in micromechanical models: void formation, growth, and coalescence. Stress localization, first, leads to void formation at the microstructural level. The progression of deformation opens up the void cavity, referred to as void growth, up to a state that voids link together (void coalescence) leading to macroscopic fracture [91].

Utilizing a representative volume element (RVE) technique is a common way to bring microstructural features into flow behavior and fracture analysis. Srithananan *et al.* [92] used an RVE approach to model macroscopic flow curves and fracture behavior of PHS. To do this, different combinations of martensite and bainite had to be prepared by altering hot stamping conditions, followed by flow measurement in various loading conditions and careful microstructure analysis to examine flow behavior and fracture of the material with respect to the microstructural components. The RVE was generated according to micrographs and boundary conditions were assigned to different combinations of micro-constituent volume fractions and distributions. Even though the RVE based models can predict the fracture behavior of PHS, the empirical observation of this evolution is expensive, complicated, and time-consuming.

Mean-field homogenization (MFH) is another micromechanical modeling approach used for fracture modeling in which micro-constituent fields are approximated by their phase average. Effective parameters in MFH are field fluctuations, geometry, and microscale phase interactions that make the modeling less computationally demanding [93]. Although micromechanical fracture models allow capturing micro-mechanisms in failure of materials, the number of experiments and amount of analysis required for the calibration of these models is still too high such that they do not attract much attention for real applications.

Unlike micromechanical damage models, phenomenological models are based on the motion analysis of a continuum body at the macroscale. Continuum damage mechanics (CDM) models are considered phenomenological since they are essentially connected to macroscopic parameters within a thermodynamic framework [94,95]. CDM predicts the onset of damage through an internal damage variable (D) which is the ratio of damage area to total surface area of a section plane. Failure then occurs as D reaches its critical value. D has a general form given by:

$$D = f(\sigma_{ij}, \varepsilon_{ij}^p) \quad \text{Equation 2-1}$$

where σ and ε^p are the stress and plastic strain tensors, respectively. In CDM, damage is coupled with the constitutive relation, therefore, a progressive connection between damage evolution and plasticity models is necessary. Various relationships for the rate of change in damage are proposed by Lemaitre [96], Wang [97], Bonora [98], and Dhar *et al.* [99], however, the complexity of calibration and large computational cost are disadvantages of coupled CDM models [100].

In addition to the coupled CDM, there are several empirical phenomenological fracture and damage indicator models that are uncoupled from constitutive models but consider fracture initiation as a limit state of the damage evolution process [95]. By this definition, a ductile fracture criterion has a general form of:

$$D = \int_0^{\bar{\varepsilon}_f} f(\text{state.variable}) d\bar{\varepsilon}^p \quad \text{Equation 2-2}$$

where $\bar{\varepsilon}_f$ is the equivalent failure strain, $d\bar{\varepsilon}^p$ is the incremental equivalent plastic strain and f is a weight function that depends on relevant state variable including observable variables, e.g.

temperature, or internal variables, plastic strain tensor (ε_{ij}^p) or stress tensor (σ_{ij}). Several such fracture models are reviewed by Wierzbicki *et al.* [101]. A constant equivalent strain (CES) criterion is the simplest form of phenomenological criterion in which f is taken as unity in Equation 2-2. In the CES approach, fracture occurs when the equivalent strain ($\bar{\varepsilon}^p$) reaches a certain value. The CES model basically predicts the equivalent plastic strain to fracture [102]. Lee *et al.* [103] proposed a stress-dependent model for damage in which critical damage can be estimated by:

$$D_c = \int_0^{\bar{\varepsilon}_f} \eta d\bar{\varepsilon}^p \quad \text{Equation 2-3}$$

where η is stress triaxiality defined as the ratio of the hydrostatic stress to equivalent stress [104]. Unlike the CES approach, the stress triaxiality-weighting in Equation 2-3 provides a stress state-dependent failure criterion. Cockcroft and Latham [105] and Clift *et al.* [106] proposed more advanced failure criteria based on total plastic work over a strain path and Johnson and Cook [107] developed a damage parameter as a function of the stress triaxiality, equivalent plastic strain rate and temperature. According to Equation 2-2, there is a critical value for the damage parameter that should be determined based on experiments; however, by using a normalized definition of the damage parameter, fracture occurs when D equals unity. Xue [108] showed that accumulated damage is then expressed as:

$$D = \int_{\bar{\varepsilon}^p} \frac{d\bar{\varepsilon}^p}{\bar{\varepsilon}^f} \quad \text{Equation 2-4}$$

considering a linear relationship between the damage parameter and equivalent plastic strain. However, it was demonstrated experimentally that the relationship may be non-linear. Therefore, a power-law function was developed by Xue [108] to account for non-linearity of loading path:

$$D = \int dD = \int d \left[\left(\frac{\bar{\varepsilon}^p}{\bar{\varepsilon}^f} \right)^n \right] = \int_{\bar{\varepsilon}^p} n \left(\frac{\bar{\varepsilon}^p}{\bar{\varepsilon}^f} \right)^{n-1} \frac{d\bar{\varepsilon}^p}{\bar{\varepsilon}^f} d \left[\left(\frac{\bar{\varepsilon}^p}{\bar{\varepsilon}^f} \right)^n \right] \quad \text{Equation 2-5}$$

in which n is a damage exponent and is determined through calibration of the model based on experiments. This non-linear damage criterion is also known as Generalized Incremental Stress-State-dependent damage MOdel (GISSMO) [109]. Ten Kortenaar *et al.* [110] and Samadian *et al.* [111] calibrated the GISSMO criterion for Usibor®1500-AS (in-die heated and fully quenched) and Ductibor®500-AS (fully quenched), respectively. Omer *et al.* [112] and Peister *et al.* [113] showed that the simulation results for the dynamic failure of Usibor®1500-AS and Ductibor®500-AS based on the GISSMO damage model are in a good agreement with the experimental measurements.

An alternative phenomenological modeling approach to predict fracture considers stress-dependent expressions of failure. Such fracture criteria can be strain- and stress-path independent and are often similar to yield criteria [95], such as the Tresca maximum shear stress [114] or Mohr-Coulomb [115,116] criteria in stress space. Although these criteria are simple, they ignore the stress state history if used without making a link to damage-indicator expressions (Equation 2-4 or Equation 2-5) [95]. The path independency of some phenomenological models is disadvantageous for accurate damage modeling due to the fact that they do not account for the accumulation of damage over various strain paths.

2.8.3 Damage and Failure Criteria for Spot Welds

There have been numerous efforts in the literature to model and predict failure of spot welds through direct analysis of the mechanics of spot welds. Despite the complexity of physical models, Nielsen and Tvergaard [117] utilized a modified Gurson micromechanics model, developed by Nahshon and Hutchinson [118], to predict shear failure of spot welds through void growth and coalescence. They found that IF happens under very low stress triaxiality for which the original Gurson model cannot accurately predict void growth. Yang *et al.* [119] also showed that a simplified Gurson model can be used to model the failure of spot welds only when PF occurs in base metal. On the other hand, phenomenological modeling approaches showed more promising results in terms of accuracy and applicability in finite element simulations. One simple failure criterion was proposed by Chao [120] based on peak load values obtained for spot welds in ST and CT tests. The model was able to provide an estimation of the load at failure (P_f) for ST and CT as a function of thickness (t), nugget diameter (d), and fracture stress of the parent metal in tension (σ_f) and shear (τ):

$$P_f^{ST} = 0.785td\sigma_f \quad \text{Equation 2-6}$$

$$P_f^{CT} = td\tau \quad \text{Equation 2-7}$$

Here, “failure” refers to onset of fracture which corresponds to peak load. The proposed model also was capable of determining the failure criterion based on von Mises ($\tau_f = 0.577\sigma_f$) and Tresca ($\tau_f = 0.5\sigma_f$) failure criteria for a biaxial stress field [121]:

$$1.623\left(\frac{P_S}{td}\right)^2 + 3\left(\frac{P_N}{td}\right)^2 = \sigma_f^2 \quad \text{Equation 2-8}$$

$$1.623\left(\frac{P_S}{td}\right)^2 + 4\left(\frac{P_N}{td}\right)^2 = \sigma_f^2 \quad \text{Equation 2-9}$$

where P_S and P_N are the shear and normal components of the applied force, respectively. The most intriguing result of Chao’s work was that the failure mechanism of the spot welds in ST, at the microstructural level, is tensile despite the global shear load that the material undergoes. A similar contradiction was observed in CT tests for which failure occurs under shear loading while the global loading is tensile [120].

Another force-based failure criterion was proposed by Wung [10] who suggested that failure occurs with respect to independent failure modes under combined static loading conditions. The simple criterion that governs the failure can be expressed as:

$$\left(\frac{f_s}{F_s}\right)^\alpha + \left(\frac{m_b}{M_b}\right)^\gamma + \left(\frac{f_n}{F_n}\right)^\mu + \left(\frac{m_t}{M_t}\right)^\beta = 1 \quad \text{Equation 2-10}$$

in which s , b , n , and t indicate shear-tensile, peel bending, normal pull out, and in-plane torsion failure modes, respectively. The F and M indicate spot weld strengths while f and m are the applied load corresponding to each failure mode. In Equation 2-10, the exponents α , γ , μ , and β are calibration parameters that are approximately 2 for small sheet thickness-to-radius ratios ($t/r < 0.3$) [122]. However, calibration of the model requires more effort for larger t/r ratios. The force-based failure criterion is not the most accurate model for spot welds but is commonly adopted for industrial applications, such as simulation of vehicle crash worthiness, due to its simplicity [10].

Rokhlin and Adler [123] measured the mechanical properties of spot welds using ultrasound techniques and implemented the results in continuum mechanics modelling of a crack tip for shear sliding to obtain a failure criterion. Despite their accurate measurements, the models were only able to predict shear failure in the vicinity of a pre-existing crack at the weld notch. Zhang [124] derived a series of formulae to estimate stress fields around the weld nugget with respect to loading condition, weld nugget size, applied load and intensive properties of the material. Lin *et al.* [11] developed a more advanced general failure criterion for spot welds under combined loading conditions, accounting for the components of load and moment on the circumferential of fracture surface in PF mode:

$$\left[1 - 2\alpha + 2\alpha^2\right] \bar{P}_z^2 + k_{P_{xy}}^2 \left[\frac{1}{3} + \left(\frac{4t}{\pi d}\right)^2 \right] \left(\bar{P}_x^2 + \bar{P}_y^2 \right) + k_{M_z}^2 \bar{M}_z^2 + 4k_{M_{xy}}^2 \left(\bar{M}_x^2 + \bar{M}_y^2 \right) = 1 \quad \text{Equation 2-11}$$

In this criterion, $\bar{P}_i = \frac{P_i}{P_{\max}}$ are the normalized failure loads and $\bar{M}_i = \frac{M_i}{P_{\max}} \frac{4}{\pi d}$ are normalized

moments with respect to a Cartesian coordinate system, t is sheet thickness, and, d is the weld nugget diameter. The term α is a load distribution factor defined as the ratio of the load in the x - z plane to the normal load, indicating the combined state of load. For example, $\alpha=1$ for pure uniaxial opening loading mode (0° loading) [125] and $\alpha=0.5$ under multi-axial (combined shear-tension) loading condition (45° loading) [126,127]. There are also three correction factors, $K_{P_{xy}}$, K_{M_z} , and $K_{M_{xy}}$, that are determined based on the experimental results under combined loading conditions. On the left-hand side of Equation 2-11, the first term represents the contribution from the out-of-plane opening force. The second term is the in-plane shear force, the third one represents the twisting moment with

respect to the out-of-plane coordinate, z , and the fourth term is the result of the in-plane bending moment [11].

As discussed in this section, several fracture criteria have been uniquely developed for failure prediction of spot welds. However, they all have limitations that restrict their application in spot weld failure modeling for the automotive industry. The most notable drawback is the damage accumulation independency and non-integrated form of the criteria, meaning that the damage history of the spot weld has not been considered. The other limitation of such specific models is associated with the complexity of the models and the large number of experiments required for calibration. Finally, they cannot be used for failure analysis of a group of spot welds in assembly-scale simulations. Therefore, it is necessary to utilize path-dependent failure criteria and detailed damage models for larger scale simulations.

2.8.4 Spot Weld Failure Simulation

In addition to the development of theoretical models for predicting the failure of spot welds, several researchers have worked on simulation of spot weld failure using Finite Element Analysis (FEA). Xiang *et al.* [128] and Malcolm and Nutwell [129] compared several material models and meshing strategies to investigate the effect of different spot weld FE models on failure prediction for automotive application. They reported that the configuration of elements within a spot weld (type, size, and arrangement), as well as the number of spot welds and their spacing, affects the failure behavior of groups of spot welds. In addition, physically meshed spot welds tend to affect predicted folding patterns, for example, in axial crush components. According to Xiang *et al.* [128] simulation results are in agreement with experiments when the spot weld is modeled as a rigid bar or by using common elements for upper and lower sheets.

Schneider *et al.* [130] and Tarigopula *et al.* [131] modeled high-strength steel crush tubes using a thin-wall approach and shell elements to calibrate the simulation parameters based on experimental results. Bier *et al.* [132] found that spot weld failure is a rate-dependent phenomenon and that weld stiffness changes under various loading conditions; therefore, they assigned elasto-plastic material models to capture rate-dependency and directional stiffness. Strong sensitivity to mesh size, weld rotation and element position were reported in Bier's work which caused numerical deviations from experimental results. Utilizing shell elements reduces computation costs but precludes modelling of through-thickness strains that have significant influence on the spot weld failure behavior. Seeger *et al.* [133] used discretized hexagonal solid elements for spot welds, coupled with a force-based failure

model to predict spot weld behavior in DP600 at the coupon- and assembly-level. Malcolm and Nutwell [129] examined such mesh orientation differences for different spot weld configurations using tied contact (Figure 2-20). Other researchers [134,135] used a similar tied contact approach to connect sheet metal shell elements to simplified solid elements for the spot weld region with improved local properties. However, the spot welds were still considered homogeneous and the alignment of the solid element spot weld mesh and the shell element sheet mesh was challenging.

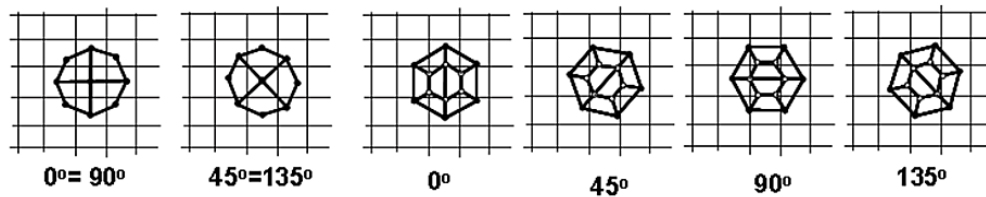


Figure 2-20. Rotational relationships between hexagonal solid elements (4 or 8 solid elements) for the spot weld and quadrilateral shell elements for the sheet [129].

The majority of available spot weld failure models in the literature use rigid constraints or beam elements (or a combination of shell and solid elements) due to simplicity and fast computation capabilities. However, it has been shown that such an approach does not account for microstructural variation through-thickness. Radakovic *et al.* [57] reported that solid elements with homogeneous material properties (e.g. hardness) can predict the failure behavior of spot welds in PF mode for several AHSS. However, the inconsistent results for IF mode was attributed to the fact that the HAZ was not considered in their calculations and all PF modes occurred in the BM for the selected materials. Wang *et al.* [136] used a strain-based criterion implemented in FEA to predict spot weld failure under complex loading conditions. They also implemented a relation between hardness and yield strength of the material to account for HAZ softening. Although they were able to capture HAZ softening in spot welds for HSLA 350, notable deviations from experimental results were observed due to mesh size effects. Dancette *et al.* [64] used a thermal gradient to estimate the strength and discretize the material properties within the HAZ. An integrated damage parameter was used to capture damage evolution within spot welds. It was found that the ductile fracture model does not work for the IF mode since the interfacial failure was considered to be completely brittle and should be defined by fracture mechanics. The available literature on failure modeling of spot welds is still limited with respect to failure damage evolution and HAZ modeling which opens a gap in understanding the failure behavior of spot welds.

2.9 Summary of Previous Work

The reviewed literature demonstrates the important role of hot-stamped steel in today's automotive research and its world-wide applicability to improve safety and performance of future vehicles. The process of hot-stamping and material development have been studied for decades and it is shown that PHS are potential materials for body structures and safety components due to their unique properties. However, the processing-microstructure-property relationship for the spot welds plays a vital role in maintaining the integrity and energy absorption of actual safety components. Since Usibor®1500-AS and Ductibor®500/1000-AS are the latest generations of press-hardened materials for such applications, it is important to develop a detailed understanding of spot weld failure. This understanding includes but it is not limited to spot weld process parameters for obtaining optimum properties, the role of microstructure in failure, local material properties of weld regions, and prediction of damage progression and failure considering the local properties.

There are some complexities in spot weld failure analysis of PHS associated with relationships between RSW process parameters, microstructural evolution, and mechanical properties of spot welds. Key requirements include understanding the effect of microstructure on failure behavior of spot welds, identifying the operative failure mechanisms and damage progression path, measuring local material properties, and last but not least predicting spot weld failure considering the microscale properties for PHS grades. Based on the preceding reviewed literature, it is clear that there is no comprehensive study on spot weld development, microstructural analysis, and evaluation of mechanical properties, and damage modeling of Usibor®1500-AS and Ductibor®500/1000-AS. Therefore, this research aims to address these gaps in the published literature and provide insight into experimental and numerical analysis of spot weld failure in PHS.

2.10 Research Objectives and Scope

2.10.1 Objectives

The goal of this research project is to provide insight into spot weld failure mechanisms with respect to local microstructure, and to develop a numerical modeling method for failure analysis and damage modeling of spot weld failure for PHS considering the local material properties. This research project contributes to the understanding of the failure microstructure-property relationship, identifying failure mechanisms and practical methods for qualitative and quantitative characterization of spot weld failure. The primary focus of this work is on PHS grades commercially known as Usibor®1500-AS,

Ductibor®500-AS and Ductibor®1000-AS in as-hot-stamped and in-die heated conditions as base materials used for automotive safety components. The specific objectives of this research are:

1. Optimize spot weld process for 1.2 and 1.6 mm thick hot-stamped and in-die heat treated PHSs.
2. Identify the effect of weld and base material microstructure on mechanical properties and failure behavior of the PHSs.
3. Identify the failure mechanisms and damage progression sequence with respect to local microstructure of spot weld regions under normal and shear modes
4. Develop a meso-scale failure model for prediction of spot weld failure and damage progression using local material properties

2.10.2 Research Scope

To achieve the objectives of this research outlined in Section 2.10.1, four inter-connected tasks were defined. A flow chart showing the progression of this research is shown in Figure 2-21. For Task 1, the main objectives were to develop spot weld process parameters for optimized spot weld quality according to AWS D8.9 [137] specifications for automotive sheet steel materials. In this task, the as-received materials were hot-stamped, weld lobes were developed based on a combination of experiment and process modeling, which resulted in selection of a common welding schedule for each material thickness.

In Task 2, the optimized spot welds were characterized by studying the microstructure and measuring hardness variation across the welds. One of the important deliverables of Task 2 was the accurately measurement of the spot weld geometries, *i.e.* sub-region shape, width and hardness variation, that were used to generate detailed spot weld models for FEA work in Task 4.

Task 3 consists of in-depth failure analysis of spot welds with respect to failure modes and mechanisms, location of failure, and development of a novel, practical method for *in-situ* observation of damage progression during spot weld failure. The results obtained from Task 3 were used to develop the meso-scale failure models in Task 4.

Task 4 consists of the major analytical part of the research which addressed the development of meso-scale spot weld failure model that can predict failure modes, location of failure, through-

thickness damage progression, and macro scale load-displacement response of spot welds under shear and normal load.

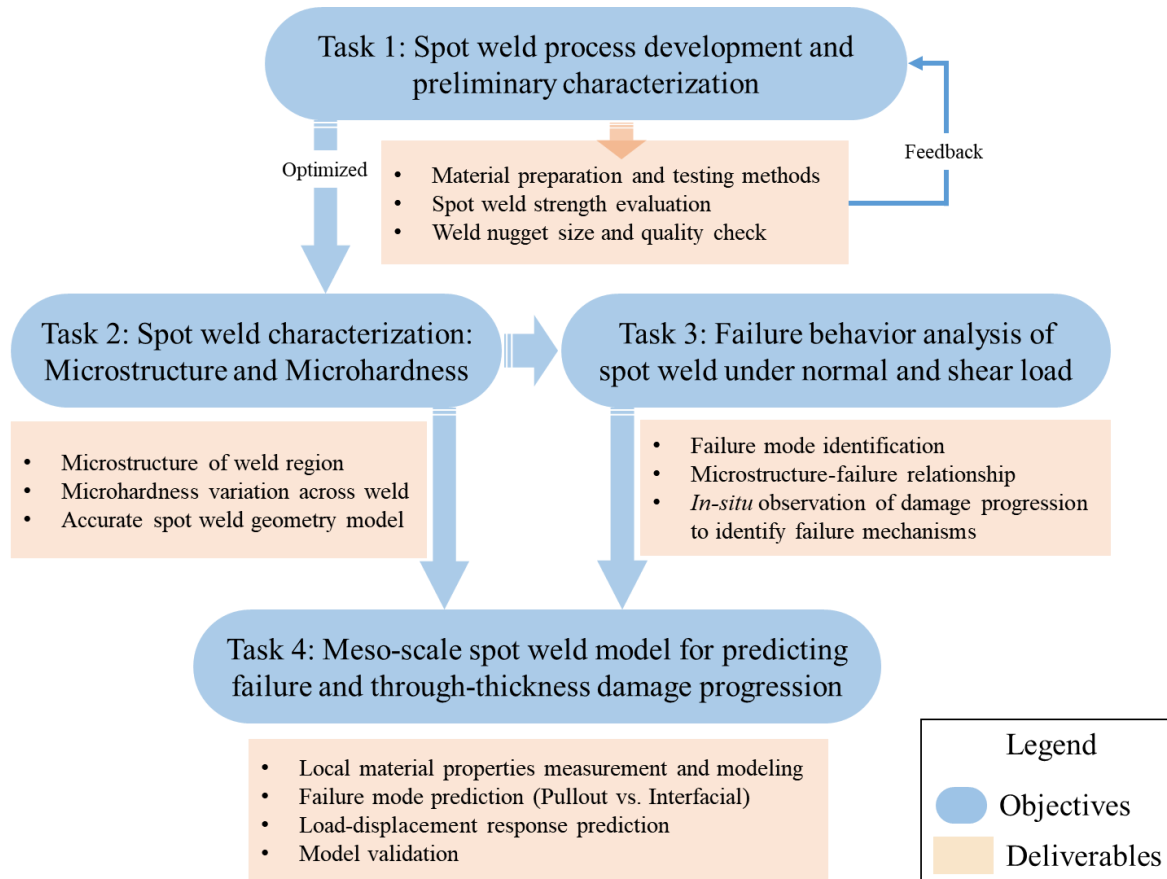


Figure 2-21. Flow chart of project progression showing the main objectives and deliverables for each task.

The balance of this document presents a synopsis of this research program, while the original research publications detailing the results are attached as appendices. Chapter 3 presents a high-level synopsis of the experimental methods adopted in this research. Task 1, comprising the weld process development for these alloys, is also covered in Chapter 3. Chapter 4 summarises the weld characterization and simulation results from Tasks 2, 3, and 4.

Chapter 3

Experiments and Methodology

3.1 Overview

Chapter 3 consists of the experiments and methods used for material preparation and resistance spot welding process development for the studied materials as required by objectives of Task 1. This chapter also includes preliminary microstructural observations, and mechanical testing procedures that are repeatedly used or referred to throughout the discussions.

3.2 Material Preparation

The materials used in the present research are Usibor®1500-AS, Ductibor®1000-AS, and Ductibor®500-AS, produced by ArcelorMittal, which offer a range of mechanical and microstructural characteristics. The nominal chemical compositions of the selected materials are listed in Table 3-1. The numeric designations indicate the nominal ultimate tensile strength after full-quench (hot stamping with chilled dies) and the term “AS” indicates the coating type (aluminum-silicon to hinder decarburization at high temperature [138,139]). The coating has a nominal weight of 70 to 80 g/m² on each side of the sheet. The sheet thicknesses considered were 1.2 and 1.6 mm for all materials.

Table 3-1 The chemical composition of the PHS selected for this research (wt.%)

Material	C	Mn	Ti	Nb	Al	Si	P	N	S	B
Usibor®1500-AS	0.226	1.21	0.030	0.002	0.051	0.250	0.016	0.005	0.001	0.003
Ductibor®500-AS	0.065	1.55	0.069	0.047	0.035	0.032	0.016	0.007	0.002	0.001
Ductibor®1000-AS	0.075	1.61	0.014	0.049	0.040	0.346	0.011	0.005	0.001	0.002

Throughout the research program, typical metallography techniques were repeatedly used to prepare cross-sectional samples of the sheet for microstructural analysis. The samples were cut using a 0.5 mm aluminum-oxide cut-off wheel in a Struers Accutom 5 precision cutter. Each cut section was hot mounted in conductive resin for optical and scanning electron microscopy (SEM). The samples were ground and polished using grit #600 to #4000 silicon-carbide sandpapers on a rotating polisher. Final polishing was performed on rotating polishing pads using 6, 3, and 1 μm polycrystalline diamond suspension as abrasive media. The microstructure was chemically revealed by a two-step etching technique which enhances the texture of images under partial microscope light. The samples were lightly etched with 2% Nital (2 ml HNO₃ + 98 ml Ethanol) for 3 to 5 seconds and immediately submerged in 12% aqueous solution of sodium-metabisulfite for about 30 seconds.

Figure 3-1 shows the optical micrographs for the as-received materials. The majority of the as-received microstructure for all three materials is composed of ferrite (white matrix) and the rest is a mixture of pearlite and bainite. Based on image analysis results, as-received Usibor[®]1500-AS consists of 70% ferrite and about 30% bainite and/or martensite. The Ductibor[®]1000-AS comprises 50% ferrite and the balance is a mixture of bainite and pearlite. Ductibor[®]500-AS has lower carbon and boron content; therefore, the driving force for diffusional transformations, *e.g.* austenite to ferrite, is higher during cooling resulting in 80% ferrite and 20% mixture of bainite/pearlite.

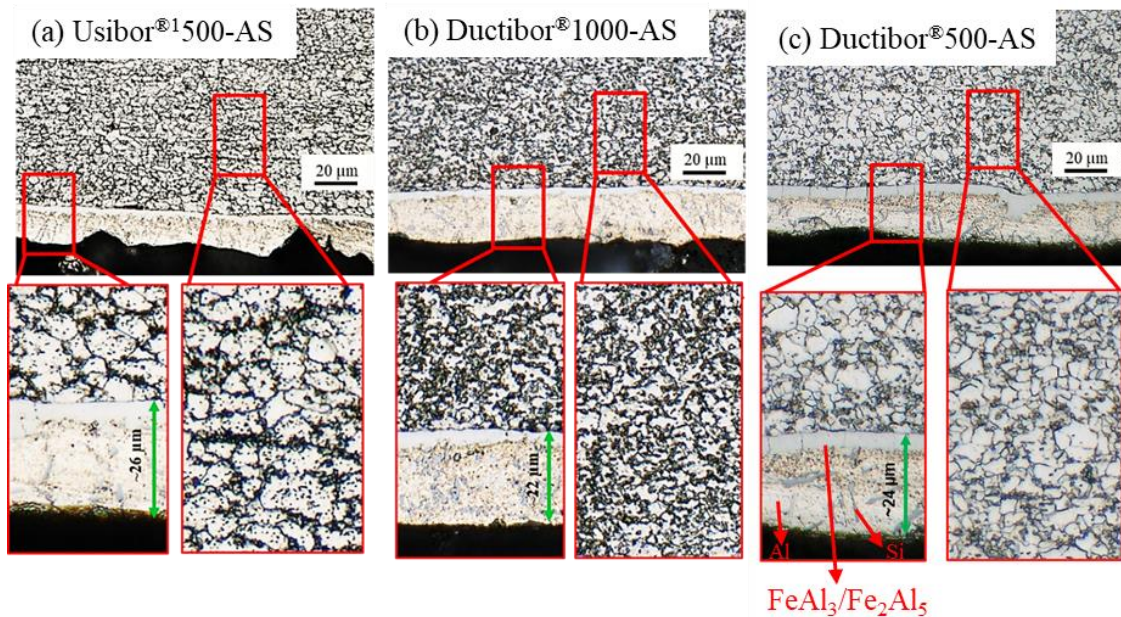


Figure 3-1. As-received microstructures of (a) Usibor[®]1500-AS, (b) Ductibor[®]1000-AS, (c) Ductibor[®]500-AS.

To prepare hot-stamped materials for spot welding, Usibor[®]1500-AS was hot stamped in three different conditions: fully quenched using a water-chilled tool or using in-die heated quenching at either 400 °C or 700 °C. This thermal treatment was done in accordance with the tailoring concept described by George [5] for producing functionally graded materials for automotive safety components. The Ductibor[®]1000-AS and Ductibor[®]500-AS were hot-stamped in a fully quenched condition only. The thermal treatment was performed by austenitizing 200 by 200 mm blanks at 930 °C for 6.5 min in a Deltech furnace with air atmosphere. Then, the blanks were rapidly transferred from the furnace to a 900-ton Macrodyne hydraulic press using an automated robotic transfer system. The total transfer time for each blank was 5 seconds. For the fully quenched (FQ) material conditions, the blanks were quenched under 60 tons of hydraulic pressure for 10 seconds using a pair of water-

chilled flat dies made of tool steel. For the in-die heated conditions, the flat dies were heated to a target quenching temperature of either 400 or 700 °C prior to quenching. The heating and quenching parameters represent typical industrial hot-stamping practice. The cooling rate for flat die quenching was reported by Samadian *et al.* [140] to be about 365 °C/s over the range of 700 to 400 °C using the cold dies. Using the heated dies for quenching the cooling rate is about 20 °C/s for quenching at 400 °C and it is in the order of 1 °C/s for quenching with 700 °C dies, as reported by Omer *et al.* [141]. The summary of the material conditions as well as the short form designations used for brevity in this synopsis are listed in Table 3-2.

Table 3-2 The summary of material conditions and hot-stamping parameters

Material	Heating		Quenching		Designation
	Temperature (°C)	Time (min)	Media	Temperature (°C)	
Usibor®1500-AS	930	6.5	Chilled Dies	11	U1500-FQ
	930	6.5	Heated Dies	400	U1500-400
	930	6.5	Heated Dies	700	U1500-700
Ductibor®500-AS	930	6.5	Chilled Dies	11	D500-FQ
Ductibor®1000-AS	930	6.5	Chilled Dies	11	D1000-FQ

The optical and electron microstructures of the various PHS materials after hot stamping for the range of die temperatures are shown in Figure 3-2. Quantitative image analysis was performed using ImageJ software to estimate the phase fractions present for each condition (listed in Table 3-3). The hot-stamped U1500-FQ and D1000-FQ conditions showed fully martensitic structures, while the D500-FQ condition consisted of 30% martensite within a ferritic matrix. Micrographs obtained from the U1500-400C condition show that the microstructure comprises about 40% bainite and 15% martensite, with the balance being ferrite. The U1500-700C material is composed of 70 % bainite, 10% martensite and 20% primary ferrite.

Microhardness measurement was frequently used to confirm the constitution of the microstructure and to correlate local material properties to the microstructure. Microhardness was measured using a diamond-shape Vickers indenter on a Clemex automatic hardness tester using 300 gr of force and 10 seconds of dwelling time. To obtain microhardness profiles across a weld, a fine indentation spacing of 50 µm was used. The measured phase fractions with maximum deviation of ±5% and corresponding average microhardness of the as-received and hot-stamped base materials are summarized in Table 3-3.

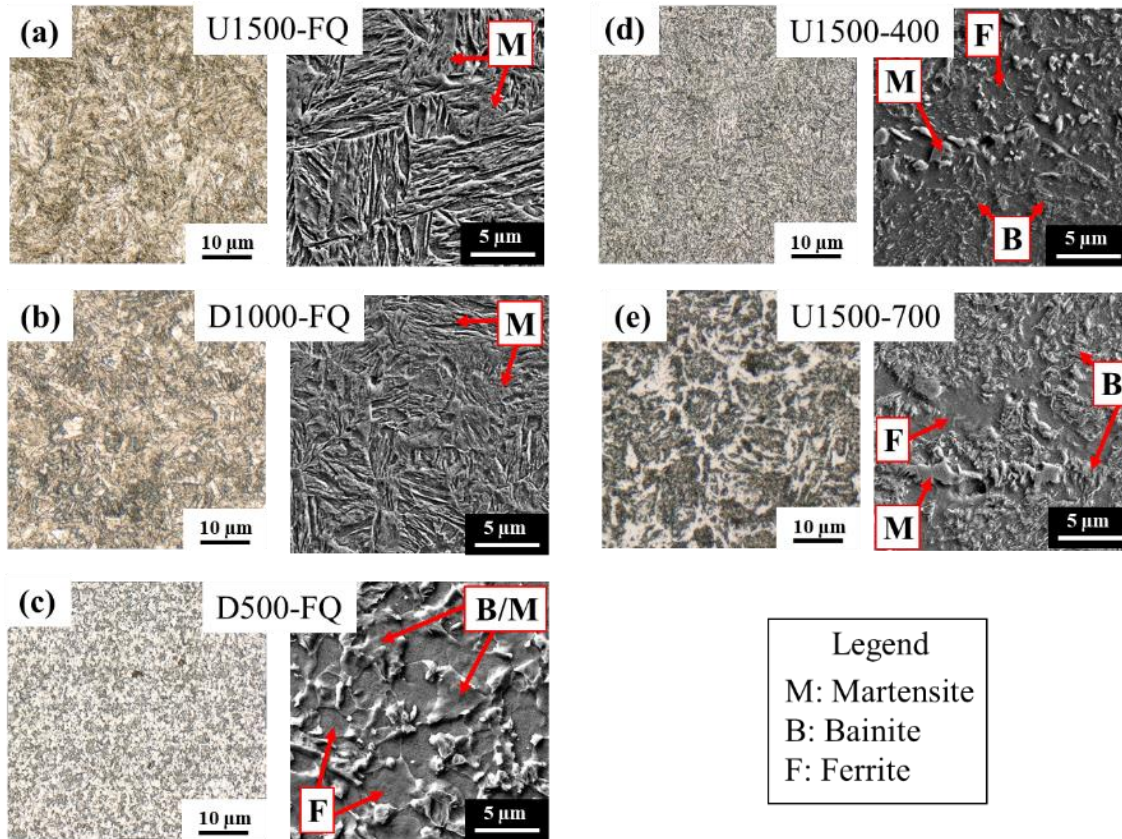


Figure 3-2. The optical and electron microstructures of selected PHS materials after hot stamping in different conditions.

Table 3-3 The average hardness values and phase fractions (F is ferrite, B is bainite, P is pearlite, and M is martensite) for the PHSs in the as-received and hot-stamped conditions

Material	Phase Constitution (Image Analysis $\pm 5\%$)	Vickers Hardness
Usibor [®] 1500-AS (as-received)	70% F + 30% B/M	210 \pm 6
Dictibor [®] 1000-AS (as-received)	50% F + 50% B/P	230 \pm 10
Ductibor [®] 500-AS (as-received)	80% F+20% B/P	181 \pm 7
U1500-FQ	100% M	497 \pm 9
U1500-400	45 % F + 40% B+15% M	262 \pm 7 [79]
U1500-700	20% F +70% B+10% M	206 \pm 6 [79]
D1000-FQ	100% M	375 \pm 5
D500-FQ	70% F +30% B/M	220 \pm 7

3.3 Spot Weld Process Development (Task 1)

To obtain an optimized set of welding parameters (to be used as the reference welding condition), a combination of experiments and software prediction was used. It is important to note that a large number of welds needed to be made with varying parameters and conditions for defining the boundaries of the welding lobe. Therefore, only the U1500-FQ and D500-FQ materials were selected for this analysis. The testing matrix was defined between 100 to 700 ms of welding time with 100 ms intervals, over the current range of 4 to 10 kA with 1 kA intervals, and the electrode force was set for every 0.5 kN between 2.5 and 4.5 kN. It is important to note that the welding parameters depend on the sheet metal thickness; therefore, the optimization was performed separately for 1.2 and 1.6 mm thicknesses. For the 1.2 mm materials, 24 sets of welding parameters were randomly selected within the defined range and the RSW was performed using a 144/180 kVA medium frequency direct current (MFDC) RSW machine with an air over oil force control system. A pre-pulse of 8 kA for 33 ms was used for all spot welds to displace the Al-Si coating from the interface prior to the main weld cycle. For all the spot welds, the initial squeeze time was 300 ms, final hold time was 1000 ms and the total flow rate of cooling water through the system was 8 L/min. Welds were made using Group A, Class II B-type electrodes (FB2500) with a 6 mm flat face [142]. The spot welds were cross-sectioned for metallographic analysis by cutting them across their diameter, the weld nugget size was measured, and the critical zones were identified for the randomly selected conditions.

To obtain a full welding window, the RSW process for the U1500-FQ and D500-FQ samples was simulated using the commercial SWANTEC SORPAS® 2D v.12.30 software over the whole range of welding parameters. The simulations included 245 distinct sets of welding parameters for each material condition for which the material databases were calibrated according to material cards provided by ArcelorMittal [143]. The comparison between the measured and predicted nugget size and weld strength can be found in Appendix A. The software was capable of predicting temperature gradients (used to identify the HAZ), nugget size, and shear-tension strength of the spot welds, based on a calibrated Swift-law constitutive equation based on the work of Eller *et al.* [144–146]. A side-by-side comparison was then done between the experimental measurements and the corresponding simulation results with respect to overall nugget shape, occurrence of expulsion, size of weld nugget, and HAZ width. An example of this comparison is shown in Figure 3-3 for the welds made at 7 kA, 700 ms, and 3.5 kN for the 1.2mm U1500-FQ and D500-FQ materials. A similar approach was used for 1.6 mm sheets to generate the welding lobes for each material condition.

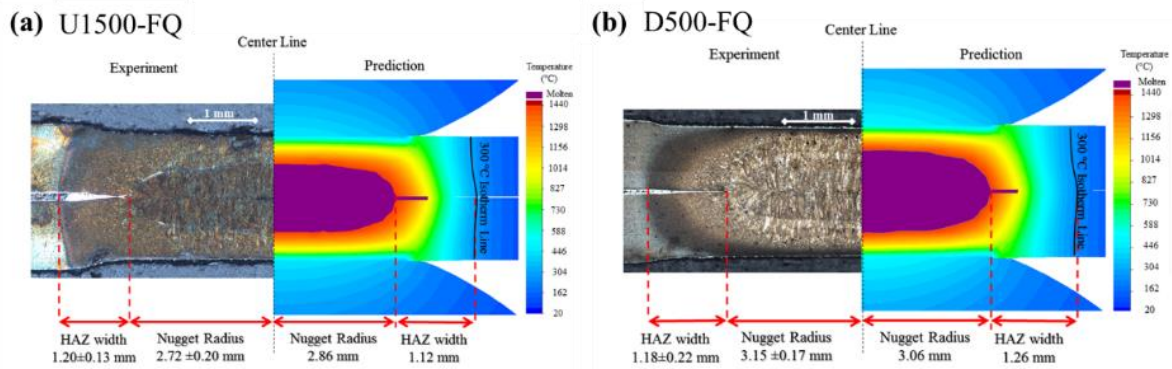


Figure 3-3. An example of side-by-side comparison of simulation results and experimental measurements for RSW at 7 kA, 700 ms, and 3.5 kN for (a) U1500-FQ and (b) D500-FQ.

The observations and results were checked against the AWS D8.9 standard [137] to determine the optimum welding settings. An example of the optimization results is presented as the 3D welding lobes in Figure 3-4. The green areas indicate acceptable welds with respect to different time, current and force values. For the sake of simplification and minimizing the involved process parameters for the next steps of the research, a unified set of welding parameters within the green area was selected for each material thickness. Table 3-4 summarizes the optimal welding parameters and resulting average weld nugget diameter that are purposely unified for each material thickness. Note that the difference in welding parameters for each material conditions were insignificant or replaceable with a similar set of settings so that the variations in weld nugget size were still negligible. More details about the spot weld process development and analytical modeling of spot weld strength can be found in Appendix A.

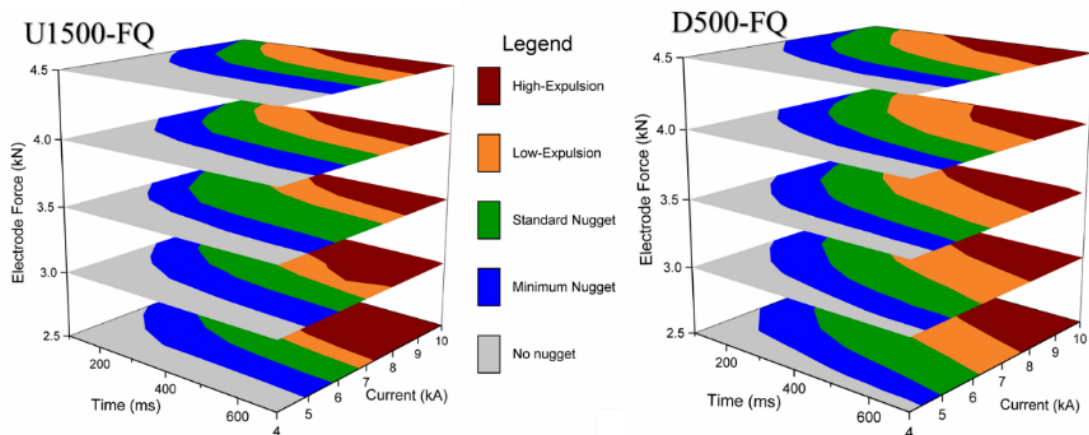


Figure 3-4. 3D welding lobes developed based on the validated simulation results.

Table 3-4 The optimized welding parameters (baseline) for different material thicknesses

Material Thickness (mm)	Pre-pulse		Main pulse		Force (kN)	Average Weld Size (mm)
	Current (kA)	Time (ms)	Current (kA)	Time (ms)		
1.2	8	33	7	400	3.5	6.02±0.15
1.6	10	33	8	500	3.5	6.11±0.23

In addition to the baseline weld process settings developed herein, a set of modified welding conditions was also considered for the 1.6 U1500-FQ and D1000-FQ material conditions as part of Task 3 and weld fracture modelling efforts Task 4. These parameters were developed to: (i) accentuate the formation of the transient softened zone in the U1500-FQ welds (weld schedule #1); (ii) suppress formation of the halo zone in the U1500-FQ welds (weld schedule #2); and (iii) promote interfacial failure under shear loading in the D1000-FQ welds (weld schedule #3). This effort is described in more detail in Chapter 4 of this thesis. The modified settings are listed in Table 3-5.

Table 3-5 The modified welding parameters used for promoting specific failure behavior

Weld Schedule	Used for	Pulses	Pulse Current (kA)	Pulse Time (ms)	Cooling between Pulses (ms)	Electrode Force (kN)
#1	U1500-FQ	1	8.5	500	0	3.5
#2	U1500-FQ	3	8	65	16	3.5
#3	D1000-FQ	1	7	400	0	3.5

3.4 Mechanical Testing

Mechanical properties of spot welds under shear and normal load were examined using standard lap-shear and cross-tension tests, respectively. Figure 3-5 shows the lap-shear and cross-tension test sample geometries recommended by AWS D8.1 [23]. Test coupons were extracted from hot-stamped blanks via waterjet cutting to minimize heat exposure. An MTS model 45 servo-electric universal tester equipped with a 100 kN load cell, model 661.20F-03, was used to perform the tests at a quasi-static rate. For both normal and shear loading, a constant crosshead speed of 10 mm/min was used in accordance with spot weld test specifications in AWS D8.9 [137]. Each test was repeated 3 times to assess repeatability of the data. More details on the mechanical testing procedure can be found in Appendix B.

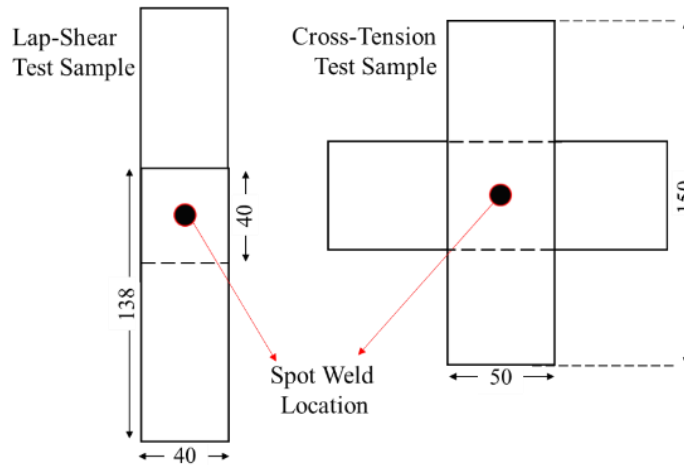


Figure 3-5. Lap-shear and cross-tension test sample geometries and dimension based on AWS D8.1 [23]. Dimensions are in mm.

For constitutive analysis of the materials, quasi-static uniaxial tensile tests were performed on sub-sized JIS-Z220-No.5 samples (as shown in Figure 3-6). The tensile tests were carried out using the MTS model 45 servo-electric universal tester at a nominal strain rate of 0.01 s^{-1} . Local strains were measured using stereoscopic DIC techniques, a pair of Point Gray Research GZL-CL-22C5M cameras, and the Correlated Solutions Inc. Vic3D DIC software. The virtual strain gauge length (VSGL) which accounts for the effect of DIC analysis parameters on the measured strains (see [147]), was kept at $\sim 0.25 \text{ mm}$ using constant step and filter size of 1 and 5 pixels for tensile tests, respectively. The tensile test coupons were sand blasted prior to testing to remove the alloyed Al-Si coating which degrades the adhesion of DIC paint to the substrate and can result in false-positives (cracking) during testing. The tensile specimens were extracted/tested along the transverse direction of the original sheets. The details of tensile testing procedure, sample geometry and test specifications can be found in Appendix E.

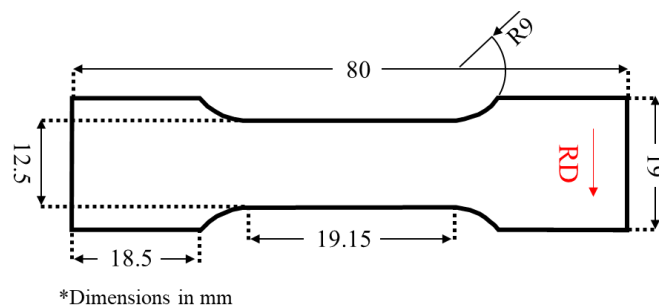


Figure 3-6. Sub-sized Tensile test specimen (dimensions are in millimeters)

For fracture characterization, V-bend testing was performed on 50 mm x 50 mm in accordance with test specifications from VDA 238-100 [148] as shown in Figure 3-7a. The V-bend tests were performed to measure fracture strain in plane strain (typically the lowest point on the fracture locus [77]) using a in inverted hydraulic test frame with a 0.2 mm radius punch and roller spacing of 3.7 mm (schematically shown in Figure 3-7b). In the V-bend test apparatus utilized for this study, the punch is stationary and the chamfered rollers descend at a constant velocity of 20 mm/min, which gradually bends the test sample. The stationary punch and chamfered rollers provide a fixed focal distance for the DIC measurements and full visibility of the deforming surface of the v-bend sample. Further details of the V-bend test setup are given by Cheong *et al.* [149] and in Appendix E. A pair of Point Gray Research GZL-CL-41C6M cameras and the Vic3D DIC software were used for local strain measurement. The VSGL was kept at ~0.3 mm for DIC analysis of the V-bend test results using a constant filter and step size of 2 and 5 pixels for all the measurements. The V-bend test coupons were extracted along the transverse direction of the original sheets and were sand blasted prior to testing to remove the alloyed Al-Si coating. The details of V-bend testing procedure, sample geometry and test specifications can be found in Appendix E.

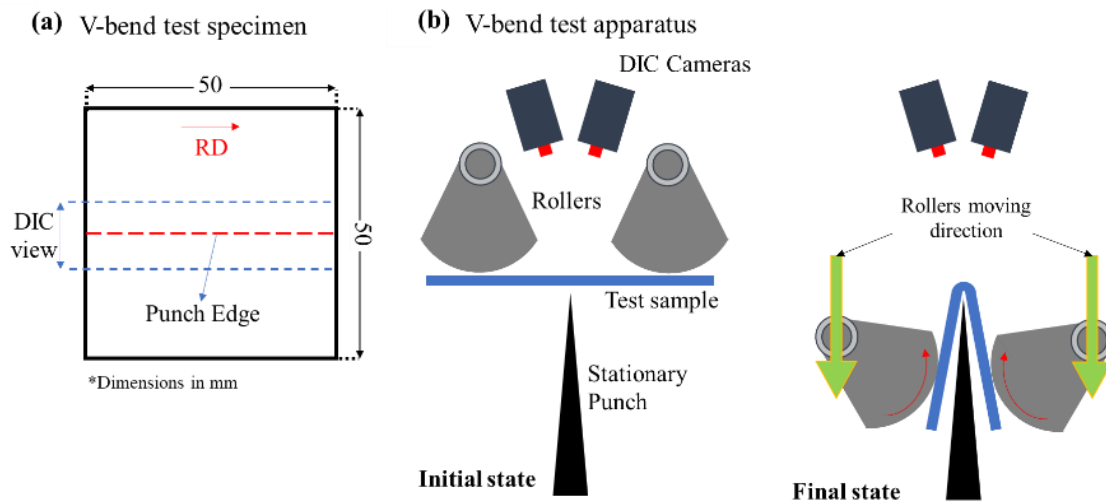


Figure 3-7. V-bend test specimen and testing apparatus in accordance with VDA 238-100 [148].

Chapter 4

Results and Discussion

4.1 Overview

This chapter presents the main results for Tasks 2, 3, and 4, as were defined in Section 2.10.2. A key aspect of Task 2 as the in-depth metallurgical examination of the spot welds to characterize the variation in microstructure and microhardness across the welds. The weld microstructural data was used to create detailed spot weld geometries for FEA, to select suitable conditions for characterization of local material properties, and to be able to correlate failure to the local microstructure in Task 3. The failure behavior of the spot welds was analyzed in Task 3 to identify failure modes, location of failure and mechanisms, and to measure load-displacement response during failure under normal and shear loading. One of the deliverables of Task 3 is the development of a novel testing technique for *in-situ* failure analysis and characterization of damage progression within spot welds which revealed the sequence of failure and cracking with respect to local microstructure. Finally, the results from Tasks 2 and 3 were used to develop detailed spot weld models that are discussed in the last section of Chapter 4. The meso-scale spot weld models reflect the microstructural details (spot weld sub-regions) based on the results in Task 2. The local material properties were measured using minimal numbers of tests required to estimate the constitutive and fracture behavior of each region. Finally, a hardness-mapping approach was used to assign local material properties of the weld material for FEA models. The simulation results were validated using standard lap-shear and cross-tension experiments obtained from Task 3 as well as the modified techniques for the *in-situ* failure analysis. Note that the majority of the results presented in this thesis correspond to welds in 1.6 mm materials unless otherwise noted. In the case of variations due to thickness difference, *e.g.* load-displacement curves, the results for both 1.2 and 1.6 mm materials are presented.

4.2 Spot Weld Characterization (Task 2)

4.2.1 Microstructure of Spot Welds

To obtain an understanding of the failure behavior of spot welds, it is necessary to examine the microstructure of sub-regions within the spot welds for different BM conditions. Figure 4-1 shows optical micrographs of the spot welds for different BM material conditions (1.6 mm thick). The FZ is martensitic for all of the material conditions due to melting and rapid cooling during spot welding.

The HAZ can be discretized into four different sections based on the microstructure. Closer to the FZ, the CG-HAZ has a coarse martensitic structure as the peak temperature reaches the austenite stability zone and is transformed into martensite during cooling. The FG-HAZ is the lower temperature range where austenite is formed during welding. However, due to a lower peak temperature and limited grain growth within this regime, compared to the CG-HAZ, the resultant microstructure is mostly fine martensite. The IC-HAZ is a multiphase region consisting of ferrite and tempered martensite, but the structure configuration and phase fractions vary for different material conditions. The IC-HAZ also may contain bainite and pearlite due partial transformation of austenite and relatively slower cooling rate depending on the specific alloy and welding conditions. In the SC-HAZ, preexisting martensite is tempered or bainite/pearlite is formed during cooling. The BM remains unaffected by the heat generated during the welding process (relevant details can be found in Appendix B)

The width and shape of the subregions within the spot welds depend on the initial microstructure of the BM. For example, the SC-HAZ, where martensite tempering occurs, is much wider for the material conditions with high amount of martensite in the BM. The difference can be seen by comparing the SC-HAZ for U1500-FQ (Figure 4-1a) in which the BM is 100% martensitic and D500-FQ (Figure 4-1c) where the BM has a maximum of 30% martensite. The SC-HAZ is also narrow (<0.3 mm) for U1500-700 and U1500-400 (Figure 4-1d and e) for which the microstructure of the BM mostly (>85% volume) consists ferrite/bainite phase (according to Table 3-3). Therefore, the sub-critical heating has a minimal effect of the stable/semi-stable phases. Comparing Figure 4-1a and b, the distribution of the phases and the width of the phases are very similar in U1500-FQ and D1000-FQ, respectively. However, the martensitic packets appear much larger in the D1000-FQ welds since it's carbon content is lower compared to U1500-FQ (Table 3-1), allowing for larger grains and microstructural features. Microstructure characterization of U1500-FQ spot weld is a main focus in the current work since the BM material has the highest hardness among the studied materials.

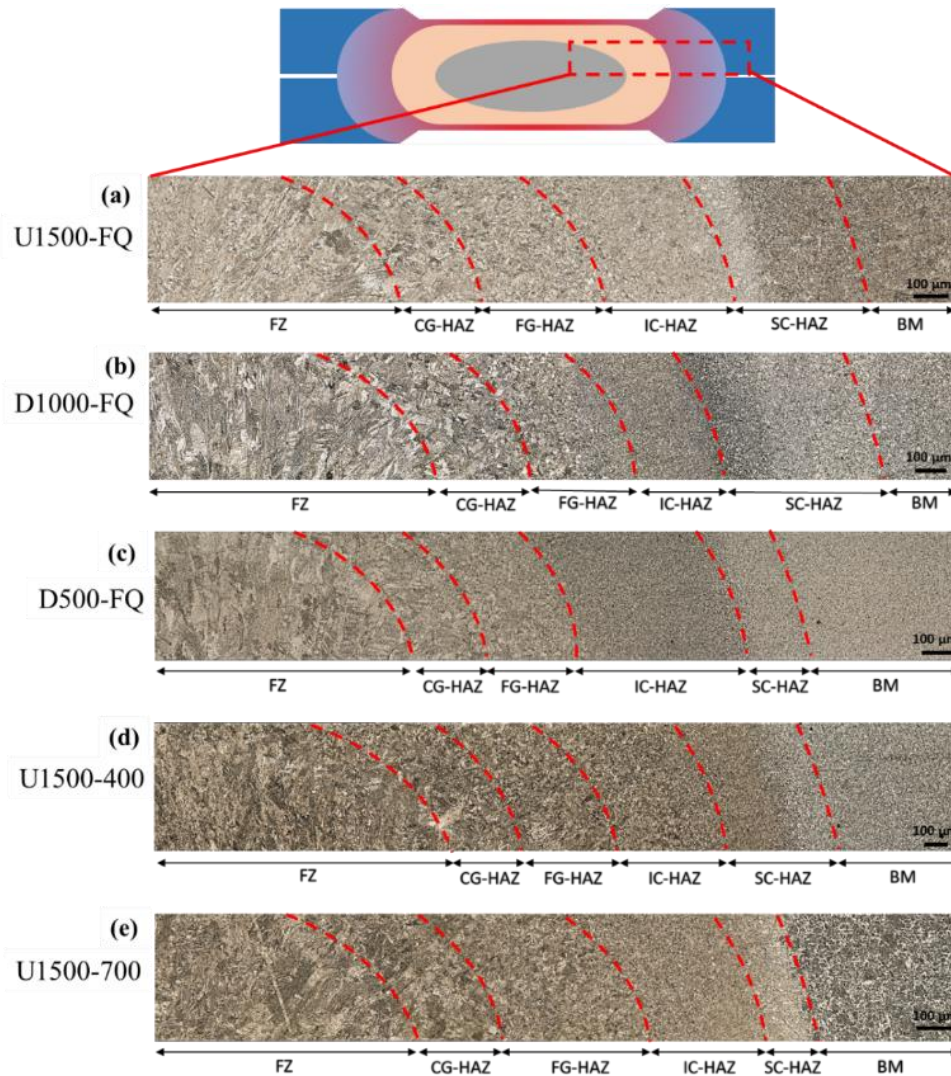


Figure 4-1. Optical micrographs of spot welds indicating the sub-regions within the spot welds for (a) U1500-FQ, (b) D1000-FQ, (c) D500-FQ, (d) U1500-400, and (e) U1500-700.

For a better understanding of microstructure configuration for the U1500-FQ spot weld, SEM images were captured from different subregions within the weld, as shown in Figure 4-2. The coarse martensitic structure in the CG-HAZ is seen in Figure 4-2a. The martensitic microstructure is much finer in the FG-HAZ (Figure 4-2b). The IC-HAZ (Figure 4-2c) consists of a mixture of ferrite and martensite with a scattered distribution of tempered martensite/bainite. Auto-tempering of the pre-existing martensite due to the slower rate of cooling is also possible in the IC-HAZ. The SC-HAZ (Figure 4-2d) shows a decomposed martensitic structure due to tempering.

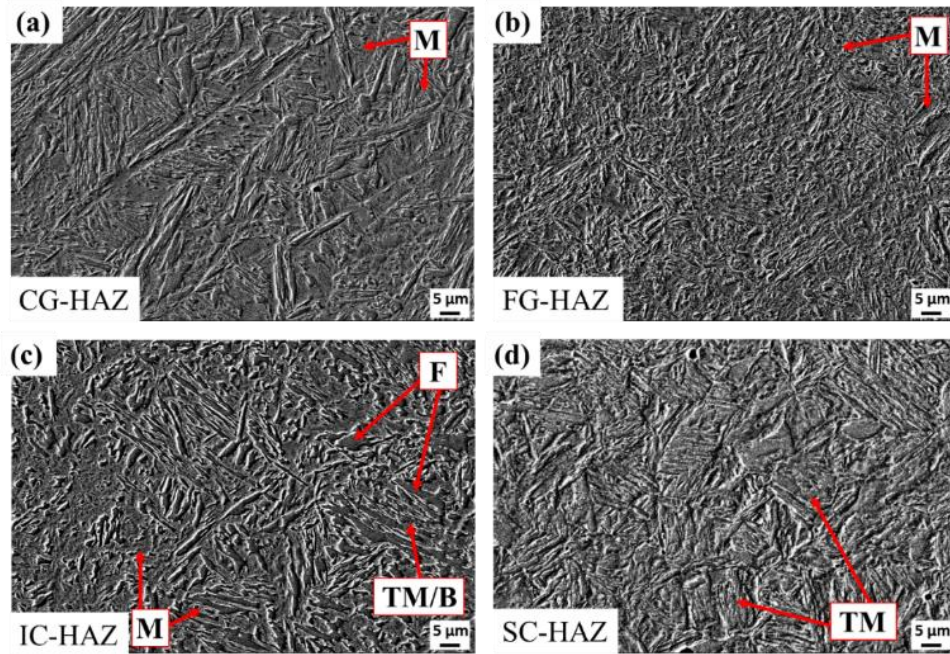


Figure 4-2. SEM images of spot weld subregions for U1500-FQ spot weld, (a) CG-HAZ, (b) FG-HAZ, (c) IC-HAZ, and (d) SC-HAZ. M: Martensite, F: Ferrite, TM: Tempered Martensite, B: Bainite

4.2.2 Microhardness Profiles

For quantitative analysis of the microstructure, the variation of microhardness was examined across the spot weld and was correlated with the observed microstructure. Figure 4-3 shows the microhardness profiles measured along a 30-degree line (schematically shown by the black arrow) for five different spot welds. To this end, the horizontal indentation spacing was kept at 0.05 mm along the path. Note that the boundaries of the sub-regions, shown by double arrows in Figure 4-3, are only approximate and the actual dimensions vary for different material conditions.

The measured hardness values for the FZ for the U1500-FQ, U1500-400, and U1500-700 welds are around 505 ± 6 HV as a result of martensite formation during rapid cooling. The hardness values of the FZ for the D500-FQ and D1000-FQ welds are about 400 ± 10 HV since both materials have lower carbon content compared to U1500. Moving from FG-HAZ towards the IC-HAZ leads to significant softening, mostly due to martensite decomposition and tempering, known as HAZ softening. The softening from the FZ hardness value is less extensive for the D500-FQ material due to smaller difference between the hardness of the FZ and BM. For U1500-FQ and D1000-FQ spot welds, the hardness increases as the measurements progress from the IC-HAZ towards the BM, since the BM

has the same hardness as the FZ (~ 505 HV) and softening due to martensite tempering becomes less effective closer to the BM. For the U1500-400 spot weld, the hardness increases slightly from 232 ± 4 to 270 ± 6 HV as measurements are taken from the IC-HAZ towards the BM. Spot welds in U1500-700 and D500-FQ do not show hardness variation over the IC-HAZ, SC-HAZ and the BM, indicating that the effect of martensite tempering is negligible. It is important to note that U1500-FQ spot weld shows a transient softening at the fusion boundary (FB) which is located at the interface of the FZ and the CG-HAZ (indicated by an orange arrow in Figure 4-3). For the optimum welding settings used to make the welds, the hardness drops by 30 HV for the U1500-FQ spot weld.

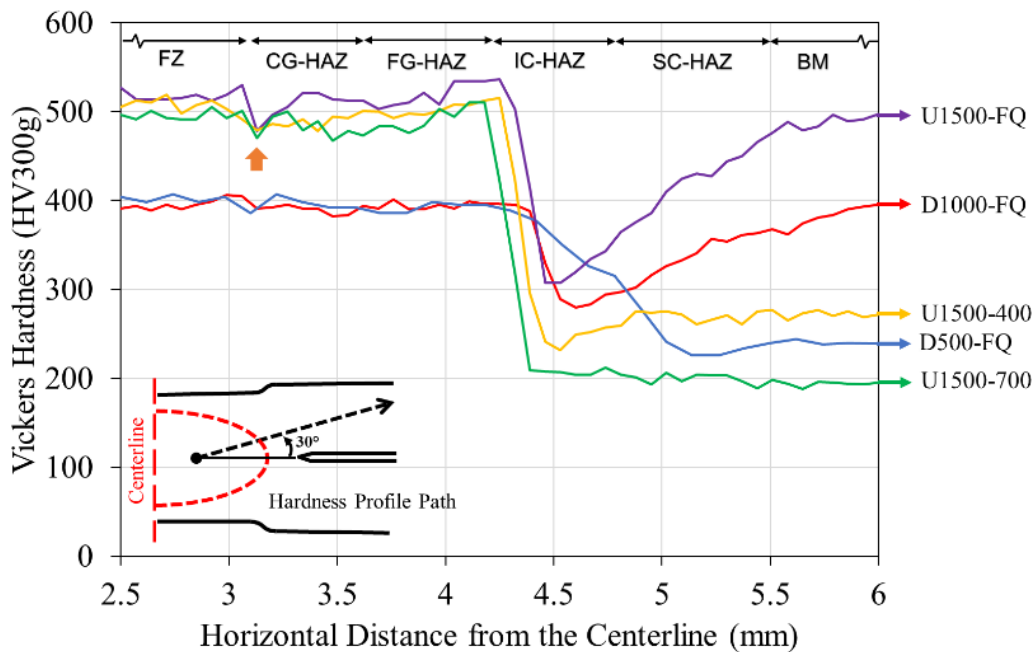


Figure 4-3. Microhardness profiles across the spot welds for different base material conditions.

4.2.3 Characterization of the Transient Softened Zone in U1500-FQ

The transient softened zone at the FB indicates that there is a mechanical non-uniformity close to the weld notch that can affect the failure behavior of the spot weld. Therefore, it is important to measure the extent of the softening at the FB and study its effect on failure. Using the two-step etching technique described in Section 3.2, the microstructure of the U1500-FQ spot weld was analyzed under partial illumination that creates a shallow angle to enhance microstructural texture. Figure 4-4 shows the micrographs obtained from the U1500-FQ spot weld under the partial light as well as Electron Backscatter Diffraction (EBSD) images. Different sub-regions within the spot weld and a

higher magnification image of the FB can be seen in Figure 4-4a. The area next to the FB that is seen as darker under the partial light corresponds to the transient softened zone observed in Figure 4-3. Due to its appearance under the microscope, hereafter, the transient softened zone is termed the halo ring in this work. The majority of previous work on spot weld characterization in this alloy (*i.e.* 22MnB5 steel) has not reported the presence of the halo ring [37,79,150]. Only in recent work by Sherepenko *et al.* [69,151] the halo ring was reported and its formation is attributed to carbon depletion of the FB during spot welding which leads to formation of soft martensite or delta-ferrite. The formation mechanism and properties of the halo ring are still unclear. However, the inverse pole figure (IPF) map obtained from the halo ring (shown in Figure 4-4b) shows a significantly larger structure next to the FB (within the HAZ) for the U1500-FQ spot weld. Based on the IPF results, the microstructural features within the halo ring are randomly oriented and have body-centered cubic (BCC) crystal structure similar to the martensitic FZ and Upper-HAZ regions. The Kernel Average Misorientation (KAM) map of the same area, indicates lower local misorientation within the halo ring compared to the FZ and U-HAZ. Note that the blue color in the KAM map has the lowest local misorientation, indicating a less distorted crystal structure. This finding is in line with the carbon depletion theory since lower carbon content would cause less distorted martensitic microstructure. More details on characterization of the halo ring can be found in Appendices B and D.

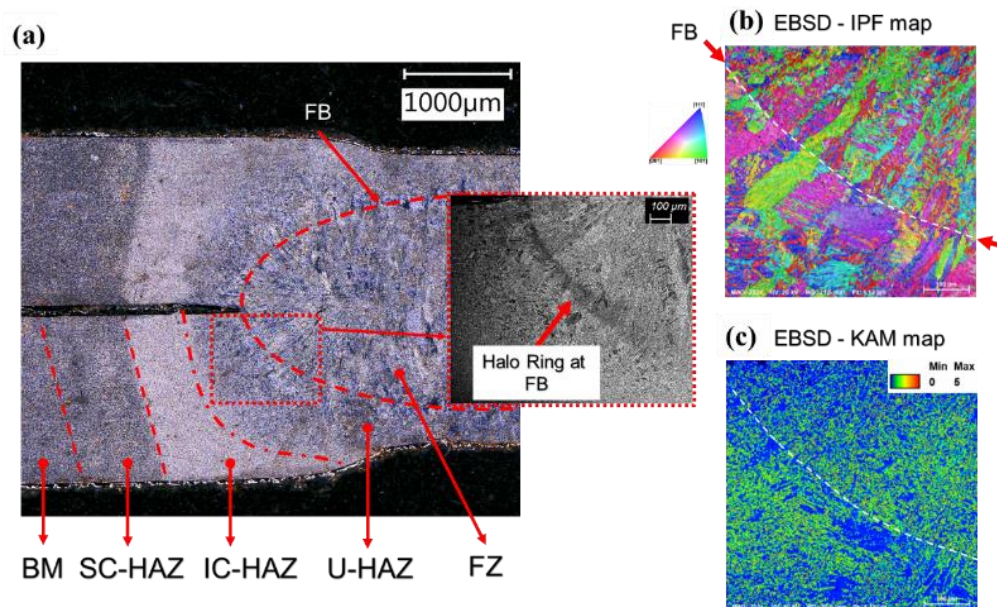


Figure 4-4. Microstructure of the U1500-FQ spot weld showing (a) the optical micrograph under partial light, (b) the EBSD - IPF map of the FB, and (c) the EBSD -KAM map of the FB.

4.3 Failure Behavior of Spot Welds (Task 3)

The failure analysis of spot welds in the present work is based on: (i) lap-shear and cross-tension tests performed to examine failure under shear and normal loading, respectively; and (ii) the modified KSII double half weld (DHW) specimens. The DHW results are given in Section 4.4, while this section presents the lap-shear and cross-tension results. More details on the DHW testing procedure and results can be found in Appendix C.

The failure behavior of the spot welds was studied by measuring the load-displacement response of the spot welds, examining the failure modes, and identifying the relationship between microstructure and failure based on the results obtained for Task 2 (Section 4.2). In this section, the spot weld failure test results including the failure modes and load-displacement curves are presented for all the material conditions. However, due to the importance of ultra-high strength spot welds in manufacturing of safety components, the main focus is on the effect of microstructure and loading condition on the failure behavior of U1500-FQ and D1000-FQ spot welds.

4.3.1 Load-displacement Curves and Failure Modes

The load-displacement curves obtained from the lap-shear and cross-tension tests are shown in Figure 4-5. Overall, the peak load values are higher for the thicker sheets. The peak loads under shear load for the U1500-FQ spot welds are about 19.1 and 31.7 kN for the 1.2 and 1.6 mm sheets, respectively. The D500-FQ spot welds show the lowest peak load and highest displacement prior to failure for the 1.2 mm thick sheets (Figure 4-5a). However, a slightly lower peak load was measured for welds in the 1.6 mm thick U1500-700 compared to those in the 1.6 mm D500-FQ sheet (Figure 4-5b).

The load-displacement responses under normal load (cross-tension tests) demonstrate rather different trends. For the 1.2 mm materials (Figure 4-5c), the D1000-FQ spot welds were the strongest, with an average peak load of 6.7 kN followed by the U1500-700 spot welds with 5.4 kN peak load. Interestingly, the measured peak load for D500-FQ and U1500-FQ spot welds were about the same value of 5 kN. For the 1.6 mm materials under normal loading (Figure 4-5d), the D500-FQ spot welds showed an unexpectedly high peak load value of 12.7 kN which was almost double the measured peak load for U1500-FQ at 6.7 kN. It is worth noting that for the cross-tension tests performed on the D1000-FQ samples, the test fixture had a smaller dimensional tolerance to minimize base metal slippage which led to a stiffer load-displacement response compared to other material conditions under normal loading.

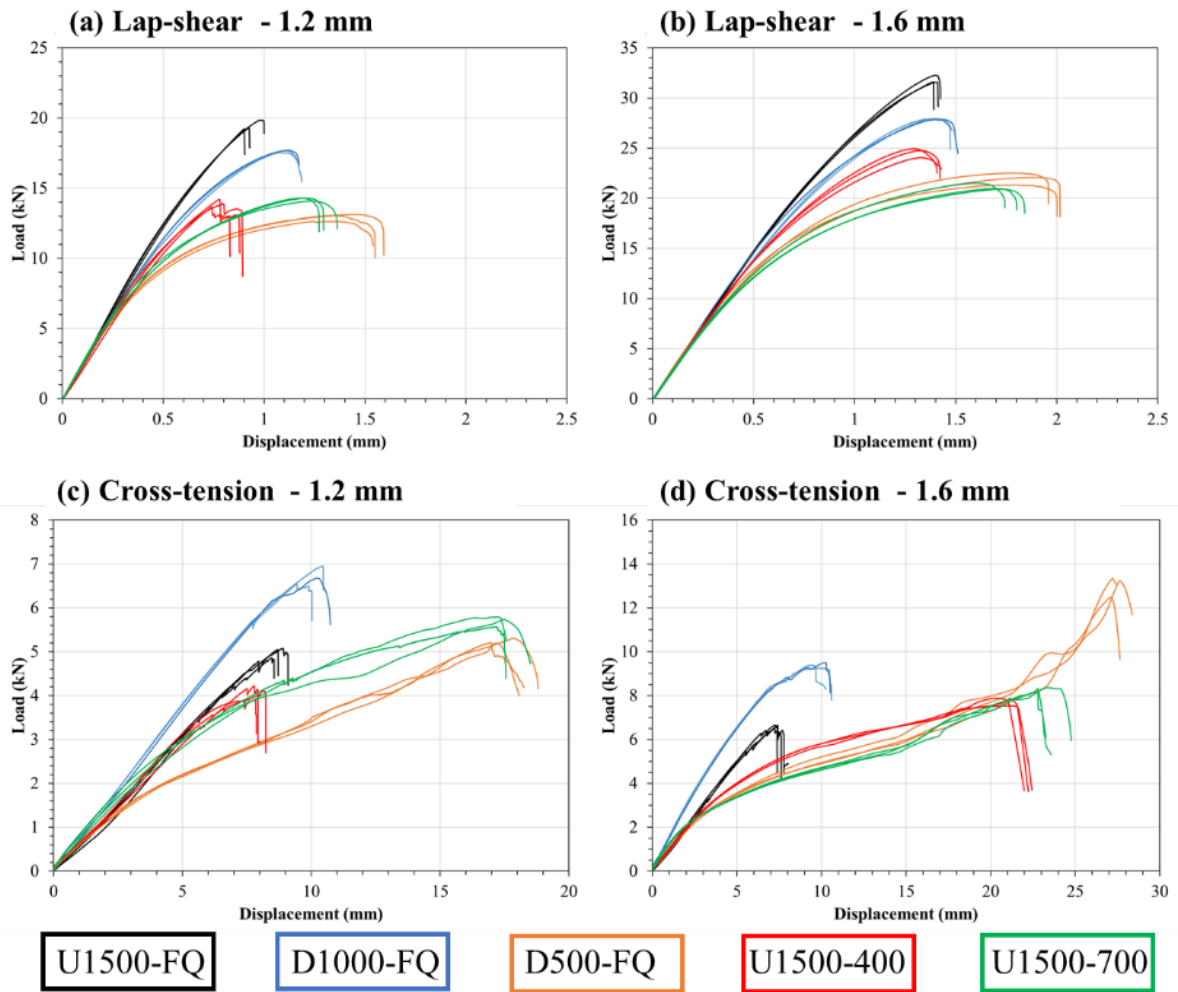


Figure 4-5. Load-displacement curves obtained from lap-shear and cross-tension tests for different material conditions and thicknesses.

The variation of measured peak load with displacement at failure is illustrated in Figure 4-6. As a general trend, the peak load values in lap-shear testing of spot welds made with a more ductile BM, *e.g.* D500-FQ, and U1500-700, are higher than those of fully martensitic U1500-FQ and D1000-FQ materials. However, this trend is not reflected in the cross-tension peak loads, for which the softer, more ductile conditions outperform welds in the strong BM. In addition, both the peak load and displacement at failure are greater for thicker sheets. For the lap-shear test (Figure 4-6a), the peak load for U1500-FQ and D1000-FQ are higher due to the martensitic microstructure of the weld region as well as the BM. For the cross-tension test (Figure 4-6b), however, the measured peak loads and

displacement to failure for the softer D500-FQ and U1500-700 spot welds are higher than those of U1500-FQ which may be related to role of the BM in global bending of the cross-tension samples.

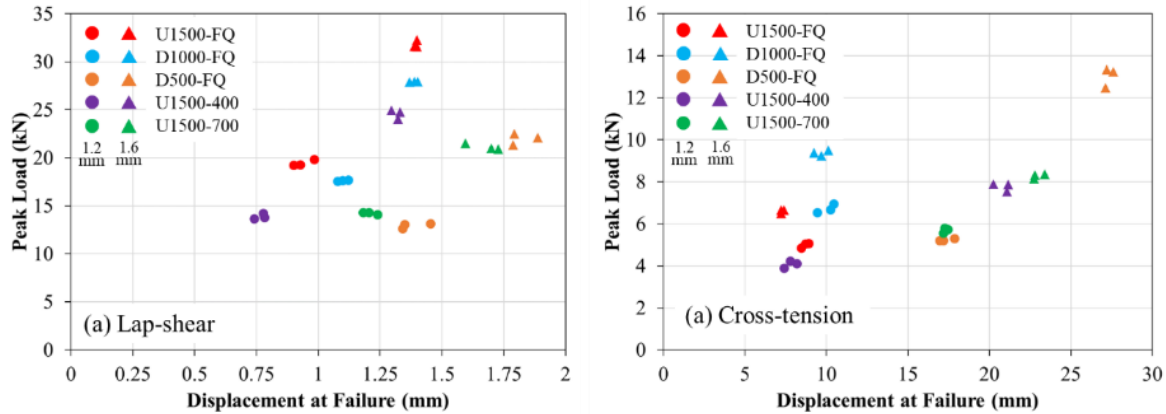


Figure 4-6. Relationship between the measured peak load and displacement at failure for different material conditions and sheet thickness (a) Lap-shear, and (b) Cross-tension.

Macroscopic observations of the failed samples showed significant out-of-plane rotation and base material bending for the D500-FQ spot weld. Figure 4-7 represents the side views of the failed samples for the D500-FQ and U1500-FQ spot welds tested in lap-shear and cross-tension loading. For the lap-shear tests (Figure 4-7a and b), out-of-plane rotation occurs for the more ductile D500-FQ, which causes gradual deviation from shear to a mixture of shear and normal loading on the spot weld. Some degree of out-of-plane rotation is inevitable during lap-shear testing which lowers the peak load for the spot welds with more ductile base metal (as shown in Figure 4-6a). Similarly, the BM bending during cross-tension testing of U1500-FQ is negligible due to the high stiffness of the base metal (Figure 4-7c). However, a maximum bending angle of 156° was measured in the base metal for the D500-FQ spot weld (Figure 4-7d). Bending gradually reduces the normal load component and imparts a shear component on the spot weld, which increases the strength of the spot weld [49,152]. The increase in load bearing capacity of the D500-FQ spot weld during cross-tension testing is seen in Figure 4-5d and Figure 4-6b. For more details on the effect of base material stiffness on load bearing capacity of the spot welds, please see Appendix A.

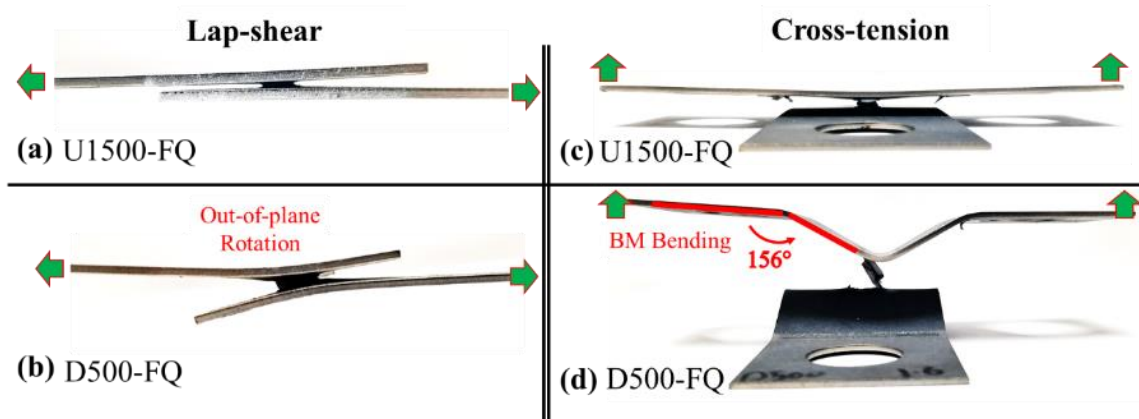


Figure 4-7. Macroscopic images of failed samples under shear and normal loads for U1500-FQ and D500-FQ spot welds.

Failure modes were identified by visual inspection of the failed samples based on the shape of the nugget and the location of failure. Figure 4-8 shows the most common failure modes for different spot welds, materials and loading conditions. The failure modes are identified based on the AWS D8.1 specification [23] which assigns a number based on the failure mode guide in Figure 4-8. All spot welds failed in pull-out mode; however, the type of the pull-out failure may vary based on the crack path and final shape of the weld nugget. Note that most of the spot welds fail in complete button pull (mode 1) or partial thickness fracture with button pull (mode 2). The fracture mode for the 1.6 mm spot weld in D500-FQ under normal loading is a combination of interfacial, button pull and partial thickness fracture which was identified as mode 4. Similarly, the 1.2 mm U1500-400 spot weld fails in mode 4 under normal loading. The only mode 5 failure mode was assigned to the weld in 1.6 mm U1500-400 under normal loading for which interfacial failure was observed in a noticeable area of the weld. Overall, it was found that failure occurs via partial thickness fracture and button pull out for the stronger BM in U1500-FQ and D1000-FQ welds. The tendency for partial through thickness fracture increases with increasing the sheet thickness. It is important to note that these welds were made using the optimized welding parameters in Task 1. Nevertheless, the repeatability of the failure modes was not perfect due to the effect of other factors such as microscopic defects, geometrical inhomogeneities, minor misalignment during testing, etc. For more details on the failure behavior of spot welds please see Appendix B.

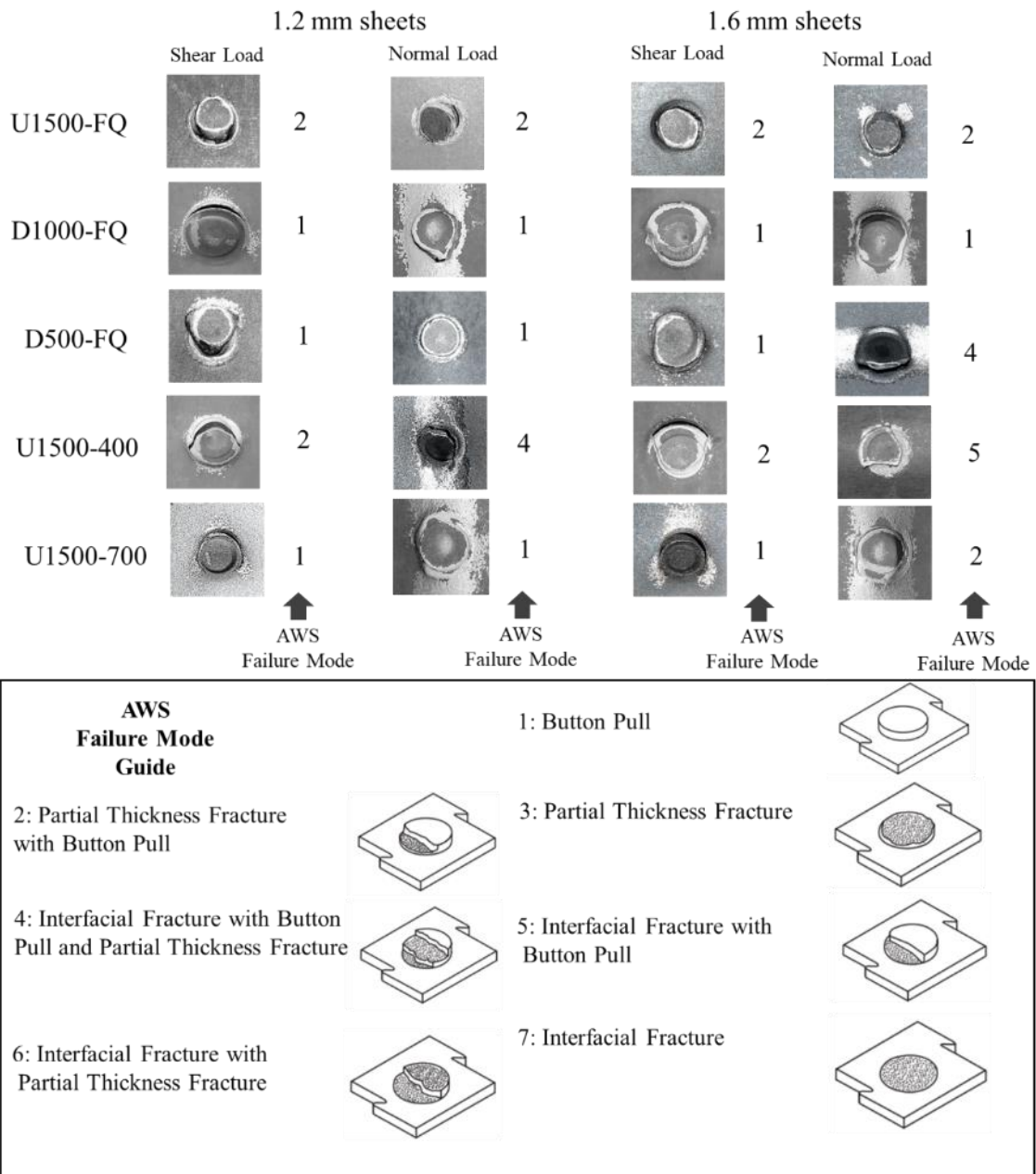


Figure 4-8. Identified spot weld failure modes for different spot welds, thicknesses and loading conditions based on AWS D8.1 specifications [23]

4.3.2 Role of the Halo Ring and Softened HAZ

As discussed in Section 4.2.3, the presence of the halo ring in the U1500-FQ spot welds can affect the failure behavior of the spot weld due to local transient softening close to the weld notch. Previous

research has suggested that spot weld failure occurs at the SC-HAZ due to the softening caused by martensite tempering [58,80]. Interestingly, in the current work, it was observed that spot weld failure for U1500-FQ occurred at the FB for both shear and normal loading conditions. The post-failure microstructures of the U1500-FQ spot welds under shear and normal loading are shown in Figure 4-9a and b, respectively. The red arrows indicate the curved failure paths which partially follows the FB. Based on the hardness measurements presented in Figure 4-3, the location of failure is the halo ring, where the minimum hardness was 470 HV, despite the hardness of the softened HAZ being lower at 307 HV. The interrupted lap-shear test at 90% of the peak load (image on right in Figure 4-9c) shows that S-shaped shear bands are formed at the FB prior to failure. This extensive shear deformation contrasts the undeformed halo band at the bottom of the sample (image on left in Figure 4-9c) which is not loaded. The observed S-shaped shear bands are not present at the free end of the bottom sheet. It is postulated that shear localization within the halo ring is triggered by the higher geometrical stress concentration at the weld notch even though the halo ring is much narrower and harder than the softened HAZ.

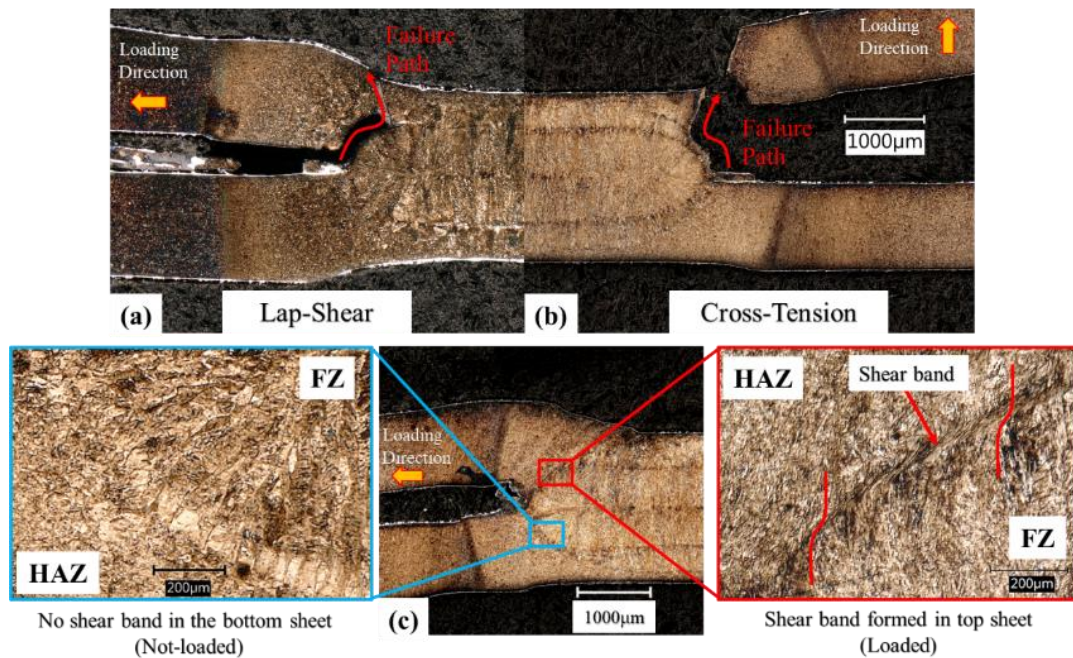


Figure 4-9. Optical micrographs of U1500-FQ spot weld showing (a) and (b) the post-failure microstructure and the location of failure, and (c) interrupted lap-shear test showing shear band formation along the halo ring.

To further investigate the contribution of the halo ring shear band to the fracture behavior of the spot weld, scanning electron microscopy (SEM) of the fracture surface of U1500-FQ spot weld was performed. Figure 4-10 shows the cross-section view and the fracture surface of the sample which failed in a Mode 2 (partial thickness fracture and button pull-out) at the FB under shear loading. Figure 4-10a shows the cross-section view of the failed weld nugget (along the loading direction) that was used to locate the shear band at the fracture surface. Figure 4-10b shows the overall shape of the weld nugget side of the fracture surface at low magnification. Figure 4-10c is a higher magnification image of the green rectangle in Figure 4-10b, showing the formation of shear bands along the fracture surface. Figure 4-10d shows a higher magnification image of the shear band region. Section A is the outer part of the shear band closer to U-HAZ which is partitioned by S-shaped micro-cracks due to shearing. The inner part of the shear band (Section B) which is closer to the FZ, is severely deformed due to shearing and failure. It is worth noting that sections A and B are both within the shear band where the S-shaped micro-cracks are formed; however, final fracture occurs in the inner section B due to geometrical constraints imposed by the weld nugget. Further details about the shear band formation at the halo ring can be found in Appendix B.

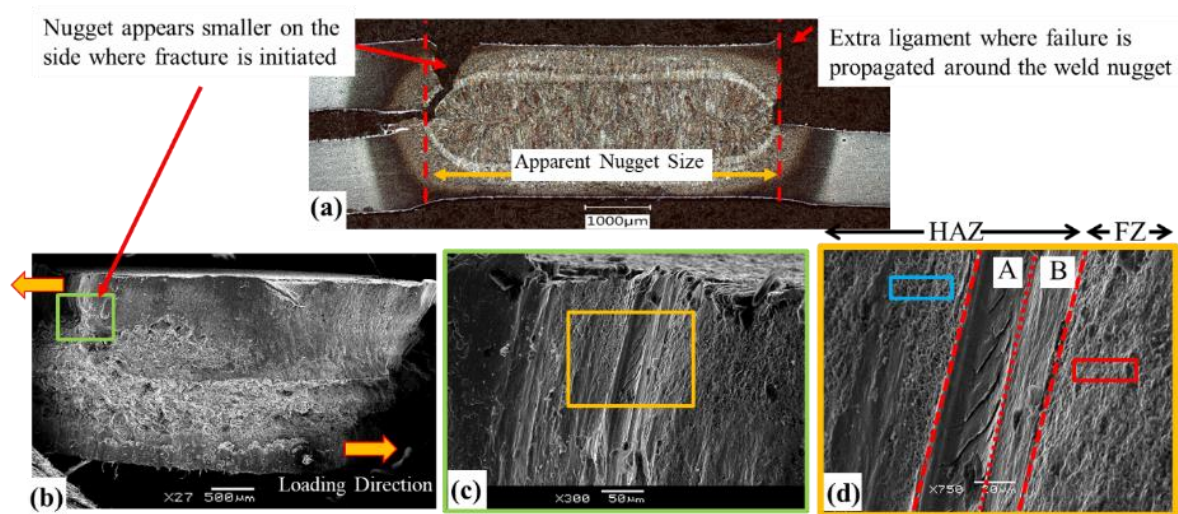


Figure 4-10. The optical and SEM micrographs obtained from U1500-FQ spot weld failed under shear loading showing failure due to shearing at the halo ring: (a) the non-symmetrical shape of the weld nugget after failure, which appears smaller on the side where failure is initiated (b) overall shape of the weld nugget, (c) higher magnification of the blue rectangle in (b), (d) Higher magnification image showing the S-shaped shear band (A) and heavily distorted band (B) due to failure.

4.4 *In-situ* Failure Analysis and Damage Accumulation (Task 3 Cont.)

Although the microstructural observations in the previous section provide some insight into the failure behavior and fracture paths during failure, the failure mechanisms and damage progression cannot be understood solely based on post-failure analysis. From a technical standpoint, the direct observation of spot weld failure is quite challenging since damage accumulates within an enclosed space close to the weld notch and failure proceeds through the thickness of the sheets. In this section, a novel technique for *in-situ* failure analysis of spot welds is proposed based on modified testing geometries coupled with DIC strain measurement techniques. Note that the *in-situ* failure analysis was only performed for the 1.6 mm U1500-FQ and D1000-FQ materials. In addition, the RSW process parameters were intentionally varied to promote or suppress formation of the halo ring and the resulting failure modes were characterized [52].

4.4.1 Modified Test Coupon Geometries

Two new specimen geometries were developed for the *in-situ* examination of the spot weld cross-section during welding, one considering failure under shear loading and the other under normal loading, as described in the following.

4.4.1.1 Modified Lap-shear Test Sample

As specified by the AWS D8.9 [137], failure behavior of spot welds under shear loading is typically evaluated using the lap-shear test in automotive sheet steel materials. In the present work, the standard geometry of the lap-shear test sample (shown in Figure 3-5) was set as reference or baseline condition for strength evaluation for both materials under shear loading to which the results using the modified geometry could be compared.

The modified lap-shear test sample geometry developed in the present work is shown in Figure 4-11. The modification includes an increased width of the original coupon from 40 to 70 mm, the use of two spot welds made with 30 mm spacing in the middle of the overlapped section, and two straight water-jet cuts at the centerline of the welds along the length of the sample that serve to create a window for DIC analysis. Note that the samples were thoroughly dried with forced air after cutting to ensure moisture is not trapped between the sheets and around the welds which could cause crevice corrosion. The removed sections of the sample after water-jet cutting are highlighted in red in Figure 4-11. Note that the final width of the modified test coupon is equal to width of the standard lap-shear

test sample. The modified lap-shear test sample consists of two half-welds on the sides and is accordingly named the “double half-weld (DHW) lap-shear test” coupon. An additional step was taken to prepare the sides of the DHW lap-shear sample for speckle paint for DIC imaging, and to reveal the microstructure of the welded region for the DHW lap-shear test sample. To this end, the edges areas were ground (#1000 grit size) and polished using a hand drill with small rotating sandpaper/pad heads. More details of fabrication of the DHW lap-shear test sample can be found in Appendix C.

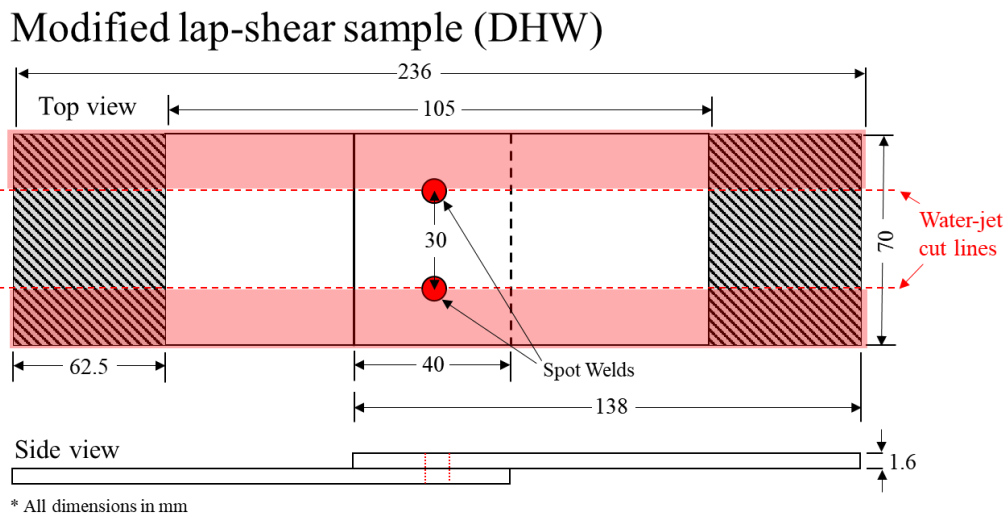


Figure 4-11. Schematic of the modified double half-weld lap-shear test geometry.

4.4.1.2 Modified Normal Loading Test Sample

The behavior of spot welds under normal loading is usually evaluated using the standard cross-tension test according to AWS D8.9 [137], as shown in Figure 3-5. Due to the nature of the test design, significant rotation and bending in the base material is expected [48]. Bending of the base material during the standard cross-tension test is inevitable (as shown in Figure 4-7) and may lead to a very complex loading condition. To minimize the base material bending effect, it is suggested by AWS C1.1 standard [153] to use a U-shaped specimen, known as the 90-degree KSII test sample [154]. In this part of the study, the conventional KSII test coupon geometry, adopted from AWS C1.1 and shown in Figure 4-12a, was adopted as the reference condition. Figure 4-12b shows the geometrical modifications made to the conventional KSII test coupon. In the next step, two U-shaped coupons were assembled as shown in Figure 4-12c, and two spot welds were made with 30 mm

spacing. The top view image in Figure 4-12c shows the final cut lines which go through the centerline of the welds. Using a programmed water-jet cutter and a custom designed fixture, the modified KSII test samples were cut to expose the central cross-sectional area of the weld for DIC imaging (Figure 4-12d). The new test sample consisting of two half-welds is termed the “DHW KSII test” sample. To prepare the cross-section prior to painting the DIC speckle pattern, as well as for microstructural observation, the face of the half-weld was ground using a rotating hand grinder to #1000 grit sandpaper and polishing pads. More details on the DHW test sample fabrication and accurate dimensions are presented in Appendix C.

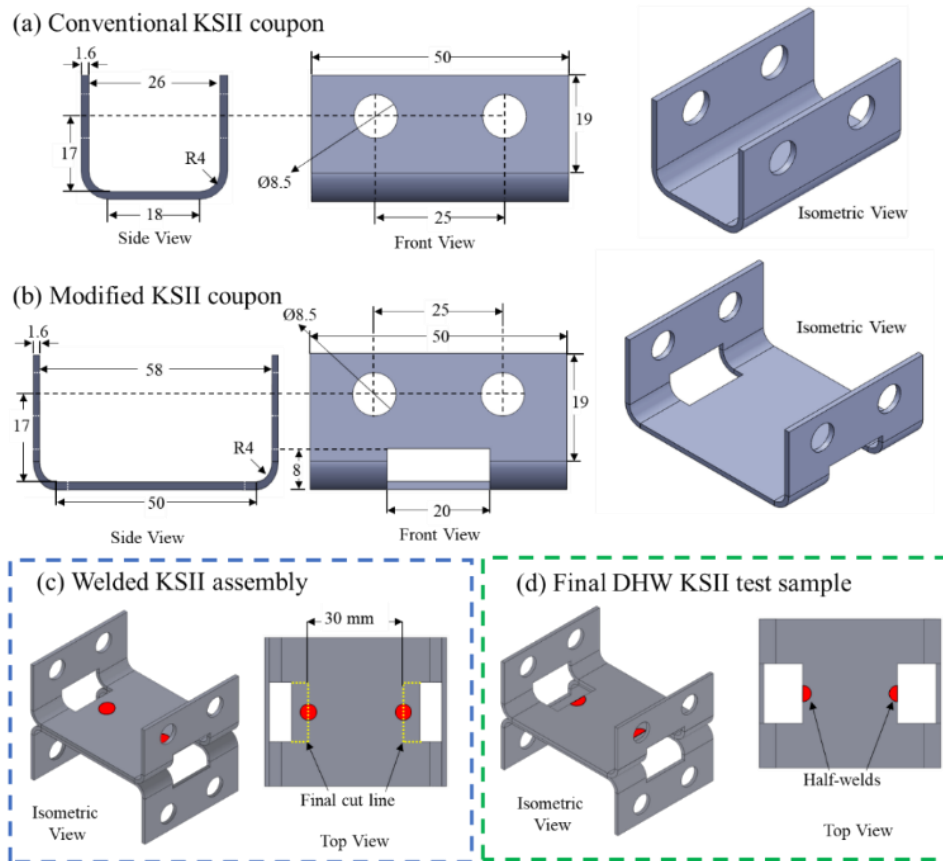


Figure 4-12. Schematic for KSII (U-shaped) test coupon, (a) conventional KSII coupon (adopted from AWS C1.1 standard [153]), (b) modified KSII pre-weld coupon, (c) welded modified KSII assembly, and (d) Final DHW KSII test sample.

4.4.2 Modified RSW Parameters

The RSW process parameters for this part of the research were modified to amplify the effect of the halo ring (cases with and without the halo ring) on failure in the U1500-FQ welds and to promote

interfacial failure (mode 7) in the D1000-FQ spot welds. Note that the spot welding parameters were intentionally selected such that the effect of the halo ring on mode 2 failure in U1500-FQ spot welds could be examined and interfacial failure in D1000-FQ was promoted. To this end, spot welds were made using 8.5 kA of current with a long pulse of 500 ms to amplify the formation of the halo ring in the U1500-FQ welds and a 400 ms single pulse weld at 7 kA to promote interfacial failure in the D1000-FQ spot welds. Note that all the created spot welds had 6.0 ± 0.2 mm nugget size.

4.4.3 DIC Results and Real-time Failure Analysis

Using the DHW testing technique coupled with DIC analysis, the stages of crack initiation, propagation and final fracture of the spot welds were captured under shear loading. The tests were performed using two different sets of samples: the speckle painted samples for local strain mapping and the macro-etched samples which revealed the location of failure with respect to weld regions. The evolution of the major Hencky (logarithmic) strain and damage progression for the U1500-FQ samples (with the halo ring) under shear loading are shown in Figure 4-13. The schematic illustration of the weld regions and corresponding hardness values for the key points are shown in Figure 4-13a5 from which the local softening of the halo ring can be discerned (HV=443). Based on the DIC results, strain accumulation first occurred in the load-bearing sheets (indicated by red arrows oriented in the loading direction in Figure 4-13a1) near the weld notch, at $t=1.91$ s (corresponding to a crosshead displacement, d , of 0.32 mm), which is sufficient to open up the weld notch. The asymmetrical loading of the joint quickly leads to rotation of the weld and progressively increases the magnitude of the localized strain adjacent to the weld notch (Figure 4-13a2). In Figure 4-13a3, cracking initiated at the notch and has propagated partially through the thickness of the top-right sheet. Final fracture occurs rapidly since the next image, taken only 0.03 s later, reveals complete detachment of the cross-section (shown in Figure 4-13a4). Similar to the standard tensile shear test, the U1500-FQ half-weld fails in pull-out mode under shear loading, as shown in Figure 4-8.

Figure 4-13b shows four stages of the failure process obtained from another DHW lap-shear test on the same U1500-FQ alloy, but with the macro-etched surface condition instead of paint speckling. The FZ, HAZ and BM regions are shown in Figure 4-13b1 at $t=0$ ($d=0$ mm) prior to the start of the test. After the initiation of the loading, the first indication of damage progression is observed at the weld notch opening, as seen in Figure 4-13b2. According to Matsuda and Kodama [155], there is a pressure-bonded area, termed the “corona bond”, at the weld notch of spot welds that is a weak metal bond but may transmit load and thereby alter the notch opening and crack propagation path. Later

during the test ($t=5.86$ s, $d=0.96$ mm), the path of the crack that initiated at the weld notch diverges from the plane of the sheet interface, to a new path that propagates around the weld nugget, as seen in Figure 4-13b3. The sequence of imagery in Figure 4-13b3 clearly demonstrates the change in the direction of the crack propagation path to propagate around the FZ, following the transient softened halo ring (443 HV). Final fracture occurs rapidly in the load bearing sheet (within about 30 ms of the previous image) as shown in Figure 4-13b4. Note that crack propagation is also observed at the corresponding location within the bottom-right sheet, although the top-right sheet is already detached. The secondary failure location shown in the inset image in Figure 4-13b4 is a manifestation of the halo crack propagation around the weld nugget by this time. In the presence of the halo ring, failure did not occur in the SC-HAZ (Softened HAZ) despite the fact that it has a lower hardness than the halo ring.

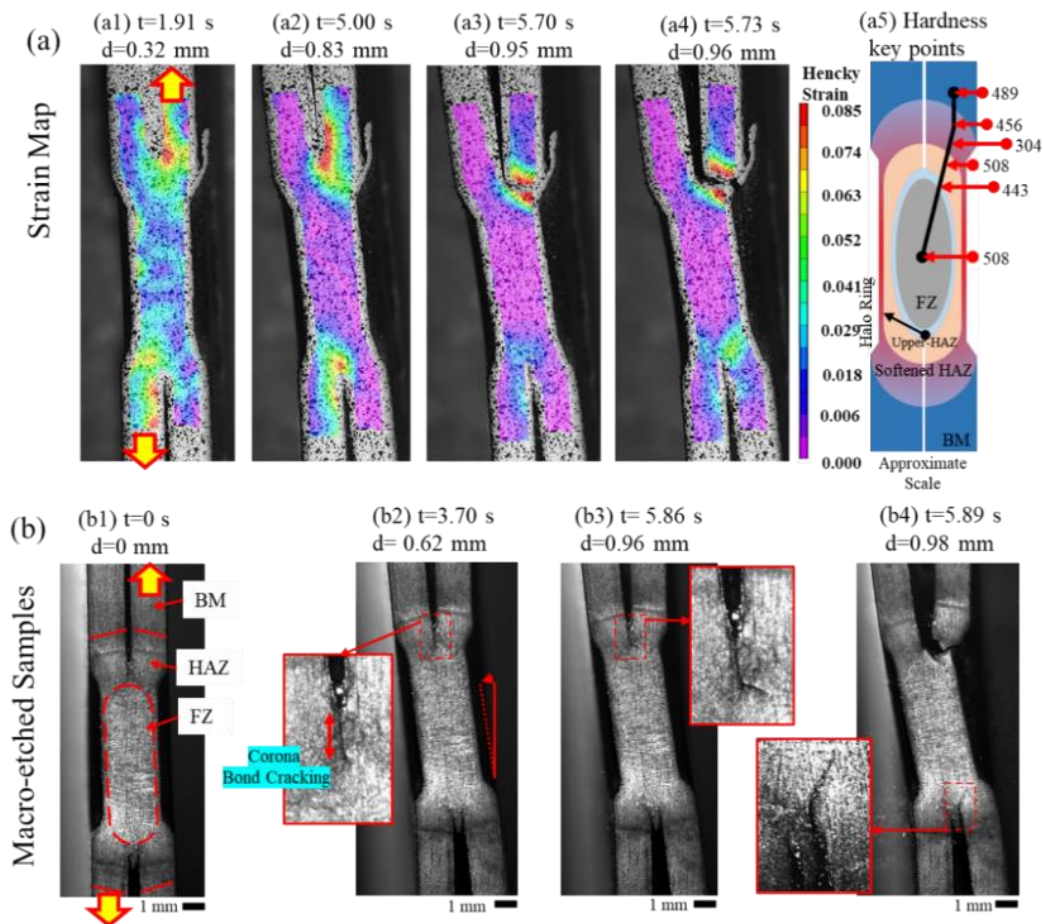


Figure 4-13. DIC results for a U1500-FQ DHW lap-shear test sample that exhibited mode 2 pull-out failure under shear loading (a) strain map, (b) macro-etched samples.

While pull-out failure is generally viewed as an indicator of a higher toughness weld, interfacial failure is often observed in advanced (and ultra) high strength steels and is permitted by AWS D8.1 [23] for alloys such as the current D1000-FQ and U1500-FQ. Therefore, it is important to understand the mechanism and damage progression for interfacial failure. Using the aforementioned modified welding schedule for this part of the work (Section 4.4.2), spot welds in U1500-FQ do not exhibit interfacial failure due to the very high hardness of the weld zone and the presence of halo ring which serves as a weaker crack path, as discussed above. However, using the modified welding parameters, interfacial fracture was found to be the dominant failure mode for the current spot welds in D1000-FQ under shear loading. The DIC results for the DHW lap-shear test considering D1000-FQ welds are shown in Figure 4-14.

At the initial stages of shear loading ($t=2.72$ s, $d=0.45$ mm, shown in Figure 4-14a1), strain localization occurs in the load bearing sheets, similar that seen prior to pull-out failure in the U1500-FQ alloy (shown in Figure 4-13a1 and a2). Asymmetrical loading led to rotation of the weld and subsequently the weld notch opened with further deformation (Figure 4-14a2). Although strain accumulation appears to be localized through the thickness of the load bearing sheets, at $t=5.13$, $d=0.85$ mm (Figure 4-14a3), an average strain of about 2% is developed along the plane of sheet interface of the weld. Figure 4-14a4 and a5 show the evolution of strain localization along sheet interface of the weld which leads to the interfacial failure shown in Figure 4-14a6. Based on the DIC results, the shear strain magnitude increases over a period of 270 ms indicating a strain development leading to ductile failure as opposed to a sudden fracture. Figure 4-14a7 shows a schematic illustration of the weld regions and key point hardness values for clarification.

In contrast to previous reports on the brittle nature of interfacial failure [31,156], there is no evidence of a brittle interfacial failure due to rapid crack propagation from these results. *In-situ* images captured from macro-etched DHW lap-shear test samples for D1000-FQ material are shown in Figure 4-14b. The red arrows in Figure 4-14b1 show different regions within the weld area at $t=0$ s. During the test, rotation of the weld occurred due to the asymmetrical load distribution around the weld nugget (Figure 4-14b2). Up to $t=3.70$ s ($d=0.62$ mm), a crack at the weld notch propagated toward the weld zone, in a manner similar to corona debonding for pull-out failure (shown in Figure 4-13a2). By comparing Figure 4-14b2 and b3, it was seen that the crack progression within the

weaker corona bond is arrested once the crack slightly penetrates the weld nugget. Following this arrest, strain localization and shear band formation develop at the sheet interface as seen in Figure 4-14a3 and a4. Figure 4-14b4, shows the occurrence of failure at the plane of sheet interface as a result of the shear strain concentration. Based on the features on the fracture surface (Figure 4-14c), the fracture surface of the outer fracture zone corresponds to the corona debonding cracking and initial crack propagation through the FZ. The outer fracture zone is characterized with cleavage facets and sharp fracture surface features (the left-hand side image in in Figure 4-14c), which indicates brittle fracture. The right-hand side image in Figure 4-14c, in the inner shear zone that is located at the center of the weld and corresponds to the sheared section of the FZ after the crack arrest. The inner shear zone was characterized with elongated cones and dimples (the left-hand side image in Figure 4-14c) as result of ductile fracture at the final stages of damage progression. The outer crack zone, which surrounds the inner shear zone, matches with the DIC analysis results indicating that the observed interfacial failure in the D1000-FQ DHW lap-shear specimens is initiated by crack propagation towards the weld nugget (crack zone) and is proceeded by ductile shearing along the interface of the sheets (shear zone).

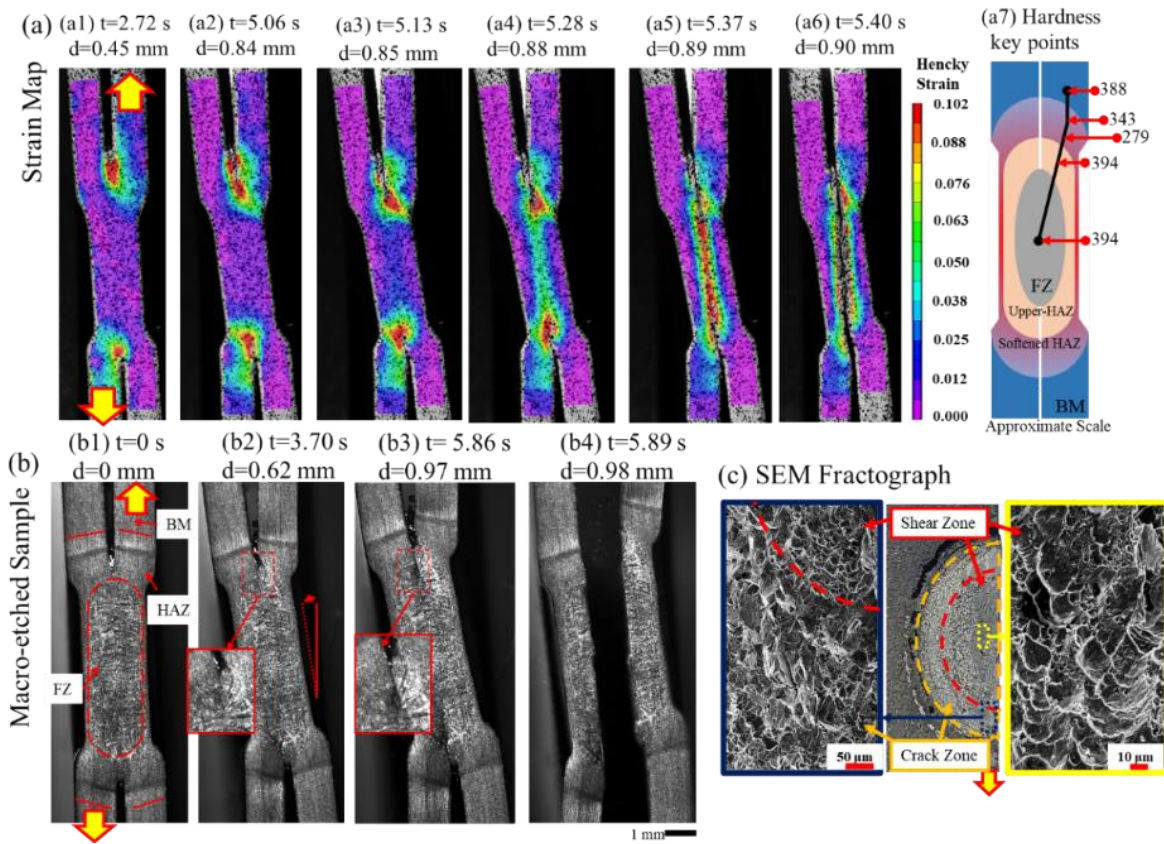


Figure 4-14. DIC results for a D1000-FQ DHW lap-shear test sample that exhibited mode 7 interfacial failure under shear loading (a) strain map, (b) macro-etched samples, and (c) SEM Fractograph.

The *in-situ* failure results for the U1500-FQ DHW KSII (opening mode) test are shown in Figure 4-15. Strain localization at the weld notch was seen at the early stages of the test, as seen in Figure 4-15a1 (at $t=1.86$ s, $d=0.31$ mm). After 16.50 s ($d=2.75$ mm) into the test, the corona bond on the left side of the weld (shown by red arrows in Figure 4-15a2) completely detaches and strain localization is slightly shifted to the bottom sheet. Figure 4-15a3 shows the initiation of crack at the weld notch and damage progression along a curved path and through the thickness of the sheet. The weld regions and key point hardness values for the U1500-FQ spot weld is shown schematically in Figure 4-15a4. According to the macro-etched images in Figure 4-15b, damage proceeds with crack initiation at the weld notch (corona bond) and its propagation towards the FZ (Figure 4-15b2). Similar to the observations for the shear condition in Figure 4-15a3, the failure path under normal loading is also redirected around the weld nugget where the halo ring is present (Figure 4-15b3). At the late stages of

loading (Figure 4-15b4), the crack branches again through the thickness of the sheet which leads to final failure.

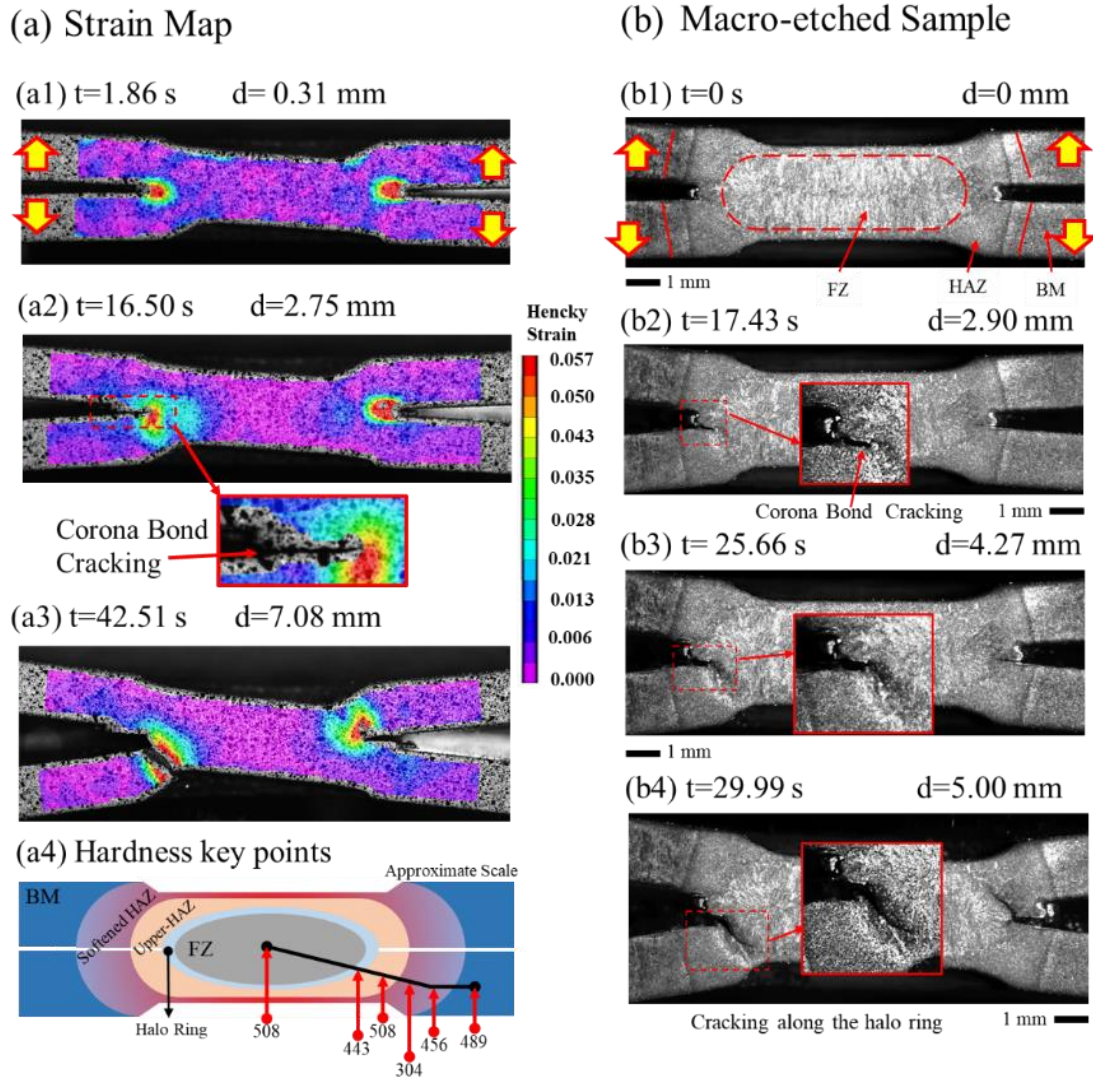


Figure 4-15. DIC results for a U1500-FQ DHW KSII test sample that exhibited mode 2 pull-out failure under normal loading (a) strain map, (b) macro-etched samples.

Figure 4-16a shows the strain contour plots obtained from the D1000_FQ DHW KSII tests. At the early stages of the test, strain localization occurs at the weld notch (Figure 4-16a1). After about 35 s (d=5.9 mm) into the test, the stresses at the weld notch led to corona bond cracking/opening, as shown in Figure 4-16a2. At this stage, the maximum strain is about 8% in front of the crack (at least at the resolution of the DIC measurement), which then proceeds towards the weld zone. As seen in

Figure 4-16a3, failure proceeds through the thickness of the bottom sheet just below the right weld notch. The weld regions and key point hardness values are shown schematically in Figure 4-16a4. It is important note that the through thickness cracks are initiated at the weld notch and do not seem to follow a specific path around the weld nugget, possibly due to the absence of a halo ring in the D1000-FQ welds.

The failure mechanisms and the *in-situ* damage progression with respect to the D1000-FQ weld regions were observed using the macro-etched DHW KSII (opening mode) test samples, as shown in Figure 4-16b. The initial state of the spot weld prior to testing and the FZ, HAZ, and BM regions are identified on the etched macro-structure as labeled in Figure 4-16b1. Similar to other loading conditions, damage progression starts with corona bond cracking as observed at $t = 18.24$ s ($d = 3.03$) into the test (Figure 4-16b2). The crack is redirected towards the thickness of the sheets, as shown by arrows in the inset image of Figure 4-16b3. The final fracture occurs along an irregular cracking path that does not follow a specific microstructural feature or weld region boundary since there is no microstructural inhomogeneity (such as the halo ring) in the case of the D1000-FQ welds (Figure 4-16b4). This observation matches with the hardness measurement shown in Figure 4-3, which indicates a smooth transition from the FZ to HAZ (in the absence of a halo ring) that is 394 ± 6 HV for both regions.

According to the literature, spot welds with no halo ring at the fusion boundary would typically fail at the softened HAZ where the hardness is a minimum due to extensive martensite tempering [31,78]. However, failure at the circumference of weld nugget is reported for spot welds in fully martensitic materials (similar to D1000-FQ) in the absence of the halo ring, although the softened HAZ has a much lower hardness [41,66]. The reason for failure at the fusion boundary is related to the geometrical constraints at the weld notch imposed by the martensitic FZ and upper-HAZ, as well as a relatively high peak load at failure for martensitic microstructures which promote failure at the weld notch.

Using the DHW testing coupled with DIC techniques for the *in-situ* failure analysis, it was found that the presence of the transient softened zone at the fusion boundary not only affects the failure mode (pull-out vs. interfacial) but also changes the location of failure, cracking path, and final fracture which all translate into variations in the mechanical properties of the spot welds. The *in-situ* failure analysis results address the majority of the objectives in Task 3 of the project and explain the operative failure mechanisms and are applied to validate the modeling results in Task 4. More details

on the *in-situ* failure analysis of spot welds, damage progression mechanisms, and microstructure-failure correlation can be found in Appendix C.

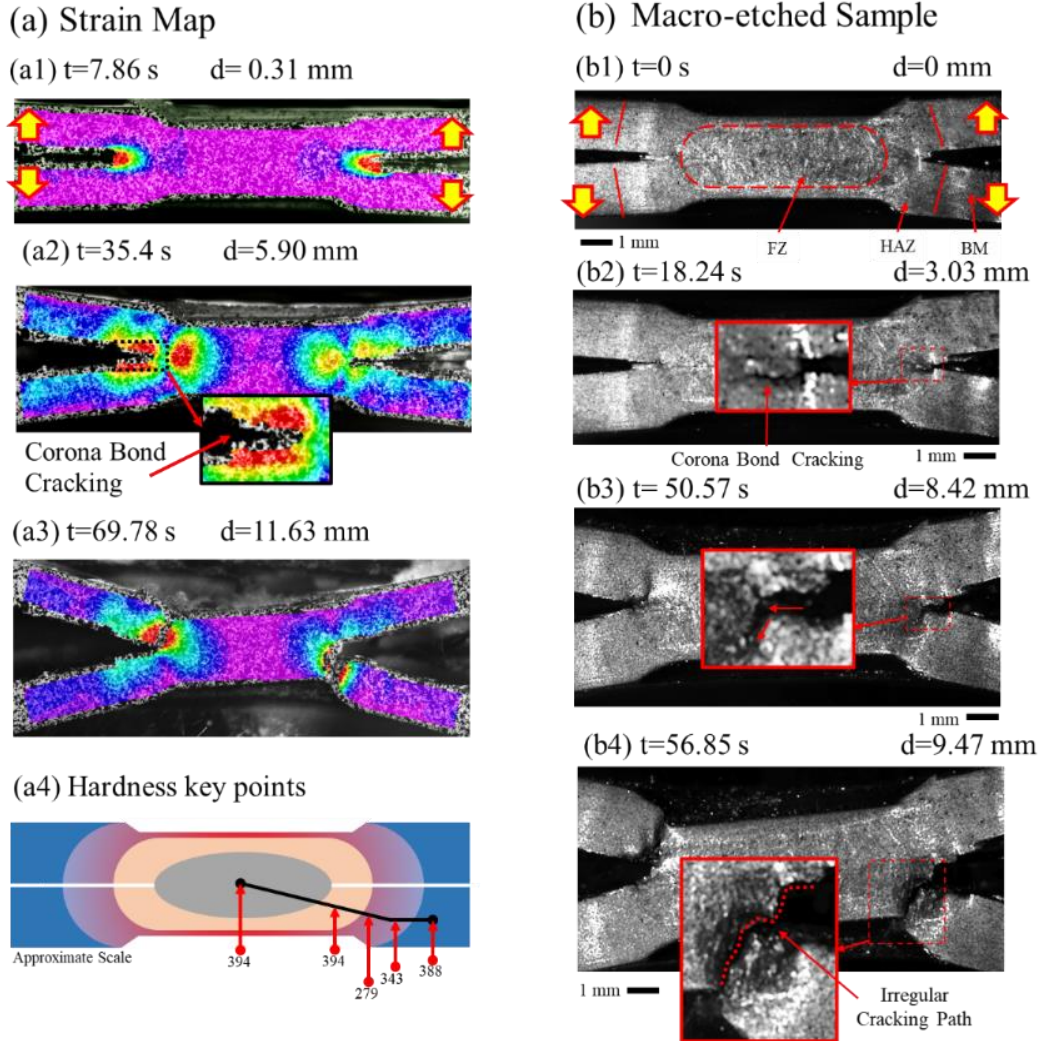


Figure 4-16. DIC results for a D1000-FQ DHW KSII test sample that exhibited mode 2 pull-out failure under normal loading (a) strain map, (b) macro-etched samples.

4.5 Meso-scale Spot Weld Damage Modeling (Task 4)

Using the microstructural observations (Task 2) and failure analysis results (Task3), it is now possible to develop the meso-scale spot weld failure models which are the final objective of the present research (defined under Task 4). Considering the variation of hardness (as a measure of local mechanical properties) across the weld region, a hardness-based mapping approach was used to

develop detailed spot weld models. To this end, the local flow and fracture properties of each region were assumed to be proportional to its average hardness. A similar approach was previously used by Bardelcik *et al.* [157] for developing constitutive flow models for quenched boron steel with tailored properties. It was shown that the flow stress behavior of the 22MnB5 steel, which was heat-treated at different temperatures, can be estimated using mathematical relationships between its hardness and empirical calibration constants. Eller *et al.* [146] used the hardness-based approach to develop a general expression for fracture locus prediction for 22MnB5 steel with 5 hardness grades ranging from 600 to 1500 MPa of strength. Simply, the fracture strains were approximate using linear interpolation based on local hardness values.

In this part of the work, hardness-based approximations of local properties were used to estimate flow stresses and fracture strains of the different regions within spot welds. To develop a detailed meso-scale model for damage progression and failure prediction, the weld nugget geometry was created using the actual dimensions of the weld regions (from Task 2). The local material properties were then assigned to the model based on the measured hardness-mapped constitutive and fracture models. Finally, failure modes, location of failure, damage progression, and load-displacement response of spot welds under shear and normal loading are predicted using FEA. The results for Task 3 are also used to calibrate and validate the simulation results. Note that only the 1.6 mm U1500-FQ and D1000-FQ spot welds were selected for the failure modeling due to both their industrial and academic importance. As part of this work, the welding process settings were altered to produce three as-welded conditions, described as:

- “U1500-FQ-no-halo” spot welds in which the welding process was altered to suppress formation of the halo ring;
- “U1500-FQ-with-halo” spot welds in which the halo ring was enhanced; and,
- “D1000-FQ” spot welds in which the welding process was altered to promote interfacial shear under shear loading.

The welds were tested and modelled under lap shear and cross-tension loading. The characterization experiments and modeling considerations are summarized in the following sections, while greater detail is provided in Appendix E.

4.5.1 Selected Spot Weld Conditions for Modeling

To establish a proper modeling approach for damage progression and failure behavior modeling of spot welds in the present work, a detailed examination of microstructure and local mechanical properties of the weld region was conducted. Failure modeling was performed for the U1500-FQ and D1000-FQ spot welds using the modified welding parameters mentioned in Section 4.4.2. For further emphasis on the effect of the halo ring on failure behavior of the U1500-FQ spot welds, a multi-pulse welding schedule was used to eliminate the halo ring while maintaining the same weld nugget size of 6.0 ± 0.2 mm. To eliminate the formation of the halo ring in U1500-FQ material, 3 pulses of 8kA for 65 ms each and 16 ms of cooling time between each pulse was used (weld schedule #2 in Table 3-5). Therefore, a U1500-FQ-no-halo spot weld was added to the existing U1500-FQ-with-halo and D1000-FQ as discussed in Section 4.4.2 for the modeling study. Here, the goal is to demonstrate the potential of the meso-scale failure models in the prediction of different failure modes. The microstructural analysis and microhardness measurement results for the selected spot welds can be found in Appendix C.

4.5.2 Hardness-mapping Modeling Approach

To generate a detailed spot weld model that accounts for local material properties, the spot weld was discretized into several isolated sub-regions based on the hardness distribution, as shown in Figure 4-17. The weld region was described using four major hardness key points; the BM/FZ material, the minimum hardness point in the HAZ (T1) and two intermediate points indicated as T2 and T3 which were used to represent the gradual hardness changes within the HAZ. The hardness of the BM, FZ and the U-HAZ are the same for each material condition (highlighted in red in Figure 4-17). Therefore, the BM, FZ, and U-HAZ were assumed to possess the same mechanical properties. In addition to these, three hardness “grades” were targeted for each material to reproduce the tempered martensite within the HAZ. The target hardness values were selected based on the hardness measurements (shown in Figure 4-17) representing different regions within the HAZ.

Finally, in order to assign properties for the halo ring in the U1500-FQ-with-halo welds, it is recognized that the halo ring essentially comprises a carbon-depleted martensite region [69,151]. This is similar in nature to D1000, which is a relatively low carbon (0.08 wt.%) hot stamped alloy (compared to U1500 with 0.23 wt.% C). Note that the minimum hardness for the halo ring was measured to be 402 HV which is close to the hardness of the as-hot-stamped D1000-FQ (~395 HV). As a result, the halo ring was modelled by assigning the properties of D1000-FQ. The balance of the

HAZ, for both BMs, comprises a tempered martensitic microstructure. Three reference points were selected from welds in each BM, corresponding to the minimum hardness in the HAZ (T1) and two intermediate values, indicated as T2 and T3 in Figure 4-17, which were used to capture the variation in hardness and mechanical properties within the HAZ. The hardness range for T1, T2, and T3 was defined for each BM based on the hardness difference between S-HAZ and the BM.

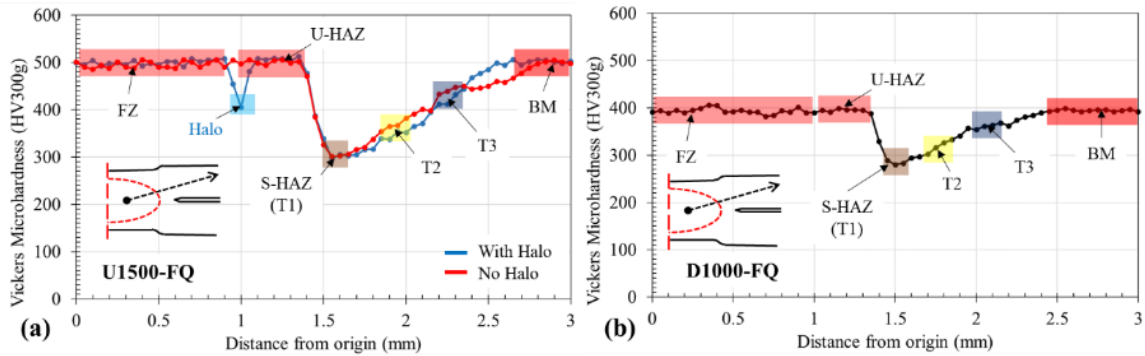


Figure 4-17. Spot weld region discretization based on hardness and definition of local material conditions for (a) U1500-FQ, and (b) D1000-FQ.

In order to characterize the constitutive and fracture behavior of the HAZ, U1500 and D1000 blanks were thermally processed (tempered) to produce tempered martensite microstructures with hardness levels matching those at points T1-T3 in each weld. The blanks were first austenitized and quenched between flat dies following the hot stamping thermal cycle described in Section 3.2 to form fully martensitic microstructures. Next, the as-hot stamped blanks were tempered by heating to temperatures below the critical austenite formation temperature (approximately 730 °C), holding for 60 seconds and then rapidly quenched. The specific temperature used to reproduce each area of interest was chosen experimentally so that the tempered samples had the same hardness as the areas of interest. The specifications for the heat-treatment and the average measured hardness for each target hardness value are listed in Table 4-1. The degree of softening from the initial as-hot stamped hardness of either 501 HV (U1500-FQ) or 395 HV (D1000-FQ) increases with tempering temperature which is consistent with a Rosenthal-type temperature field during spot weld [158,159]. The three resulting hardness levels are very close (within ± 7 HV) to the target values measured at locations T1-T3 for each BM; thus, the as-tempered coupons were used to determine the constitutive and fracture behavior of the HAZ needed to model the fracture behavior of the welds.

Table 4-1. Heat-treatment specifications, target and measured hardness values for recreated HAZ materials

Material Condition	Initial State: U1500-FQ				Initial State: D1000-FQ			
	Temperature (°C)	Time (s)	Targeted Hardness (HV)	Measured Hardness (HV)*	Temperature (°C)	Time (s)	Targeted Hardness (HV)	Measured Hardness (HV)*
T1	550	60	305	311	600	60	285	278
T2	500	60	355	350	500	60	320	324
T3	400	60	415	421	400	60	355	357

* Average measured hardness for 10 indents for each material condition.

4.5.3 Spot Weld Failure Model Description

Using the actual dimensions of the weld and microhardness measurements in Task 2 (Section Chapter 14.2), the meso-scale spot weld models were developed based on a hardness-mapping approach for local material properties of the weld regions. The detailed weld geometry considering the dimensions of the sub-regions for the studied spot weld conditions were created in Altair® HyperMesh Desktop 2019 software using 3D solid elements. Numerical simulation of the failure of the three spot weld conditions under shear and normal loading was undertaken using the LS-DYNA R10.0 commercial finite element package. For the cross-tension tests, a quarter-symmetry model was used, while a half-symmetry assumption was adopted for the lap-shear tests.

A reduced physical domain, *i.e.* partial test coupon geometry, was modelled in order to simplify the problem and reduce run time. Figure 4-18 shows photographs of the actual samples and the grip areas (above) compared to the meshed domain (below). The blue dashed lines and the highlighted regions correspond to the extent of the finite element model, respectively. Due to the high stiffness of the BMs for both U1500 and D1000 (martensitic microstructure), the observed additional bending for the cross-tension specimen and out-of-plane rotation for the lap-shear specimens outside of the meshed regions were considered to be small and were neglected. Therefore, using the reduced physical domain for the simulation, a realistic compliance can be obtained. It is assumed that the remaining parts of the test coupons, *e.g.* the grip area and clamped sections, have no effect on spot weld failure. More details about the simulation process and boundary conditions can be found in Appendix E.

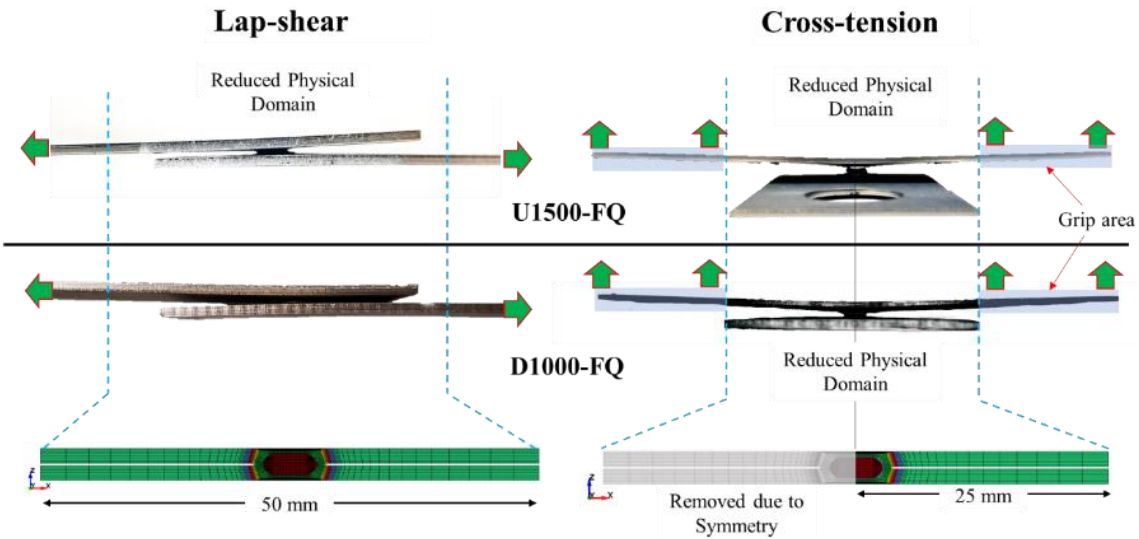


Figure 4-18. Correspondence between actual test specimen and the reduced physical domain for simulation.

An example of the meshing strategy and local property assignment is shown in Figure 4-19 for the cross-tension model for the U1500-FQ-with-halo spot weld. The nominal element size within the weld region (excluding the elements associated with the BM) is 0.06 mm. To assign the local material properties, the weld geometry was discretized into separate zones representing different sub-regions with the spot weld (as shown by different colors in Figure 4-19c). The local material properties were assigned to isolated sections of the model based on the average measured hardness, as shown in Figure 4-19c for the U1500-FQ-with-halo spot weld condition as an example. The hardness values assigned to each region (as shown in Figure 4-19c), for the three welding conditions, are listed in Table 4-2.

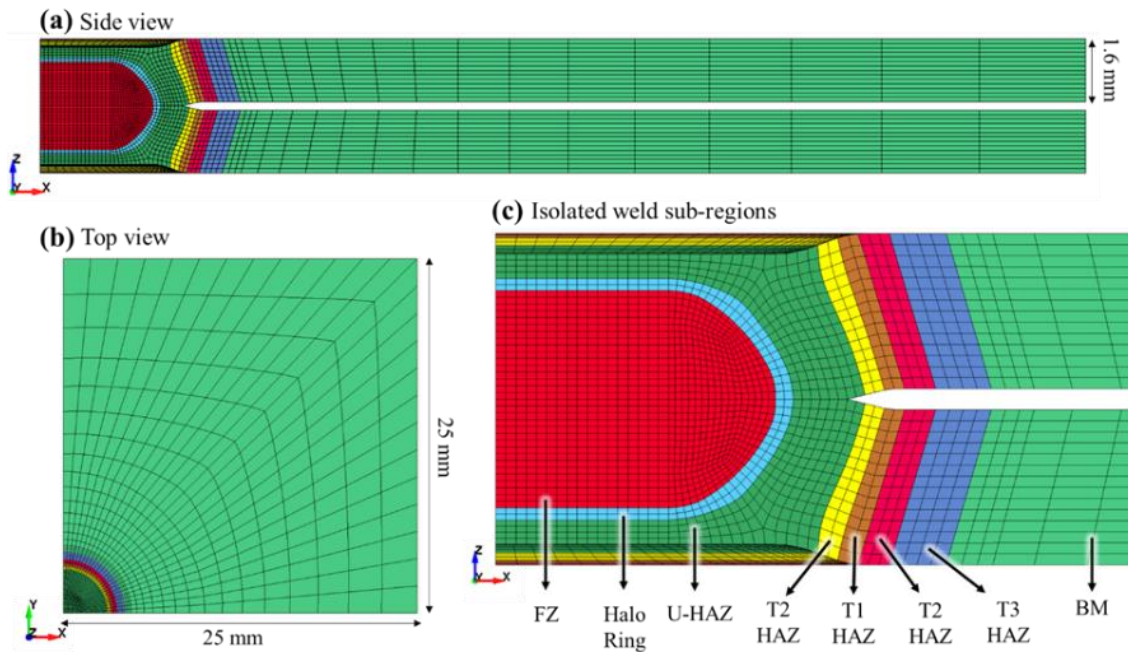


Figure 4-19. Detailed weld geometry for U1500-FQ-with-halo and isolated sub-region within the weld (Quarter symmetry model for normal loading test).

Table 4-2. Hardness values assigned to different weld regions shown in Figure 4-19

	FZ	Halo Ring	U-HAZ	T3-HAZ	T1-HAZ	T2-HAZ	BM
U1500-FQ-with-halo	505	395*	505	415	305	355	505
U1500-FQ-No-halo	505	Same as FZ	505	415	305	355	505
D1000-FQ	395	Same as FZ	395	355	285	320	395

* Important note: Considering that the halo ring is a carbon depleted region [151], the properties of the as-hot-stamped D1000-FQ was used to define the halo ring in U1500-FQ-with-halo spot weld.

4.5.4 Local Material Property Measurement

For developing the material cards to be used in FEA, the constitutive flow models and fracture loci for different loading states are required for all materials associated with the welding regions. To start, the constitutive models and fracture loci for as-hot-stamped U1500-FQ and D1000-FQ base metals were assigned based on previous work by Samadian *et al.* [160] and Lee [161], respectively. The constitutive response and fracture behavior of the tempered materials (listed in Table 4-2) were characterized by performing quasi-static uniaxial tensile tests on sub-sized JIS-Z220-No. 5 samples and plane-strain v-bend tests, as shown in Figure 3-6 and Figure 3-7, respectively. The tensile data

were used to develop constitutive models and the v-bend results were used to develop fracture loci describing the local material properties required for FEM. Details regarding the measurement setups and parameters used for DIC analysis can be found in Appendix E.

4.5.4.1 Constitutive Models

Figure 4-20 show the engineering stress-strain (S-E) curves obtained from tensile tests for U1500 and D1000 in the tempered martensite conditions. Also plotted, are the corresponding curves for as-hot-stamped U1500 material, adopted from Samadian *et al.* [162], and D1000 from Lee [161]. The ultimate tensile strength of the U1500-FQ condition is approximately 1600 MPa, compared to 1100 MPa for the D1000-FQ condition. The UTS drops as the material undergoes more severe tempering by increasing the tempering temperature.

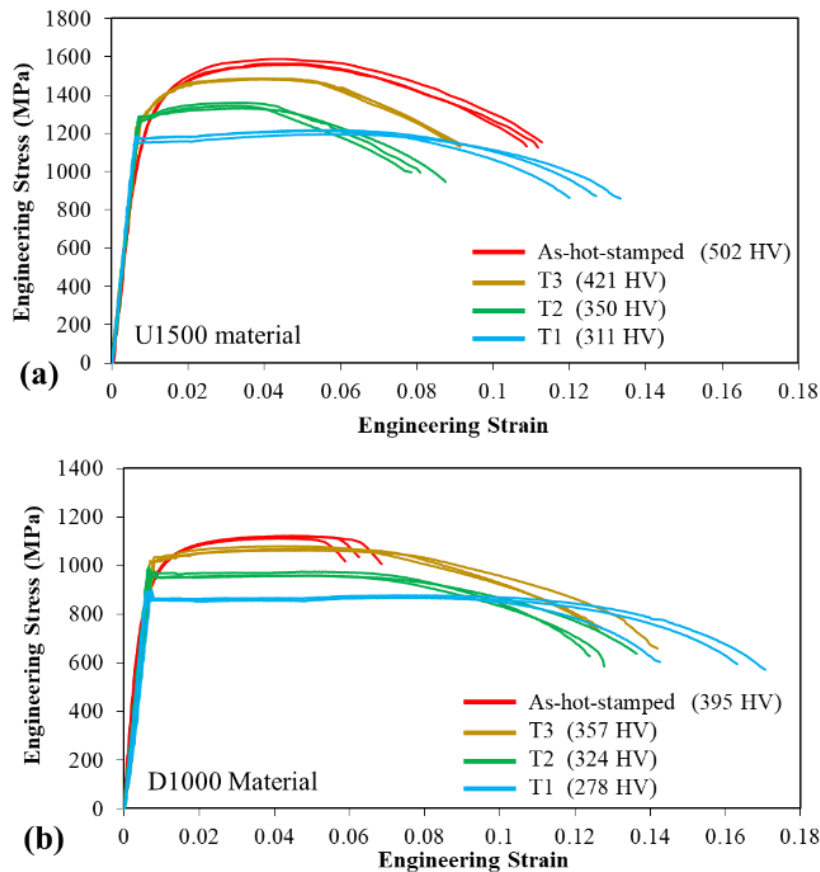


Figure 4-20. Engineering stress-strain curves for hot-stamped U1500 and D1000 adopted from Samadian *et al.* [162] and Lee [161] and the tempered HAZ materials.

Figure 4-23 shows the measured flow stress at 5% elongation, extracted from the tensile test results shown in Figure 4-20b and c. It is evident that a linear relationship between the hardness and the measured stress at 5% elongation exists for each alloy, shown in Figure 4-23 along with the R-squared values for the linear fits (0.97 and 0.93 for U1500 and D1000, respectively). Therefore, the flow stress for the HAZ material conditions (tempered martensite microstructure) can be correlated to the hardness variation.

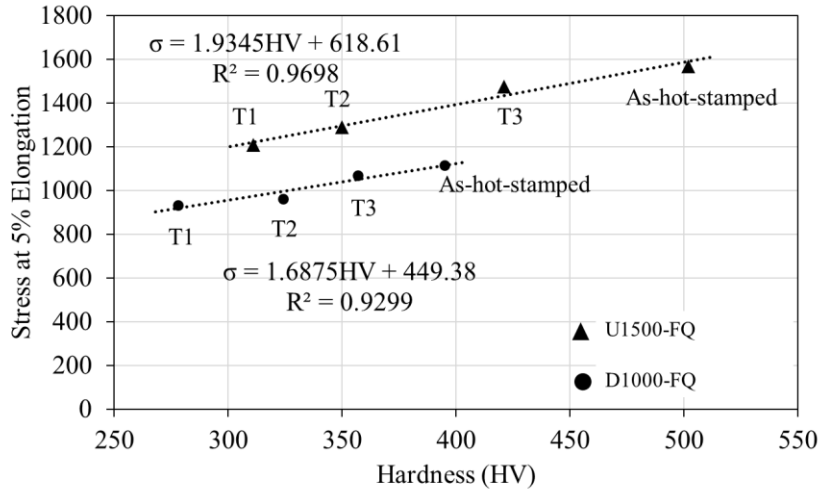


Figure 4-21. Linear relationship between stress at 5% elongation with hardness for as-hot-stamped and tempered martensitic (HAZ) conditions. As-hot stamped tensile data for U1500-FQ due to Samadian et al. [32] and for D1000 due Lee [42]

To develop constitutive models for the various sub-regions, needed for the FEM simulations, the measured engineering stress-strain (S - E) curves (Figure 4-20b and c) were converted to true stress ($\bar{\sigma}$) vs. equivalent plastic strain ($\bar{\epsilon}$) data using:

$$\bar{\sigma} = S(1 + E) \quad \text{Equation 4-1}$$

$$\bar{\epsilon} = \frac{\sqrt{2}}{3} \sqrt{6\epsilon_1^2 + 6\epsilon_2^2 + 6\epsilon_1\epsilon_2} \quad \text{Equation 4-2}$$

where ϵ_1 and ϵ_2 are the major and minor plastic strains calculated from the DIC results. The $\bar{\sigma} - \bar{\epsilon}$ curves are shown as solid lines in Figure 4-22. This data was utilized for the BM, FZ and U-HAZ, as described in Section 4.5.3. The curves were extrapolated past the necking point to larger strains using a weighted hardening law described by Ling [163]. The dashed lines in Figure 4-22 show the modified Hockett-Sherby [164] curves fit to the experimental data and can be described as:

$$\bar{\sigma} = C_1 - (C_1 - C_2)\exp(-C_3(\bar{\epsilon}_p)^{C_4}) + C_5\sqrt{\bar{\epsilon}_p}$$

Equation 4-3

where C_1 to C_5 are calibration parameters. The model calibration was performed for all the material conditions considered in the present work using the OriginPro analytical software and adopted a Levenberg–Marquardt (also known as damped least-squares) procedure for which the resulting calibration parameters are listed in Table 4-3. According to the calculated mean square errors (R^2), which are equal to or higher than 0.97. Note that the material properties were considered to be isotropic [141].

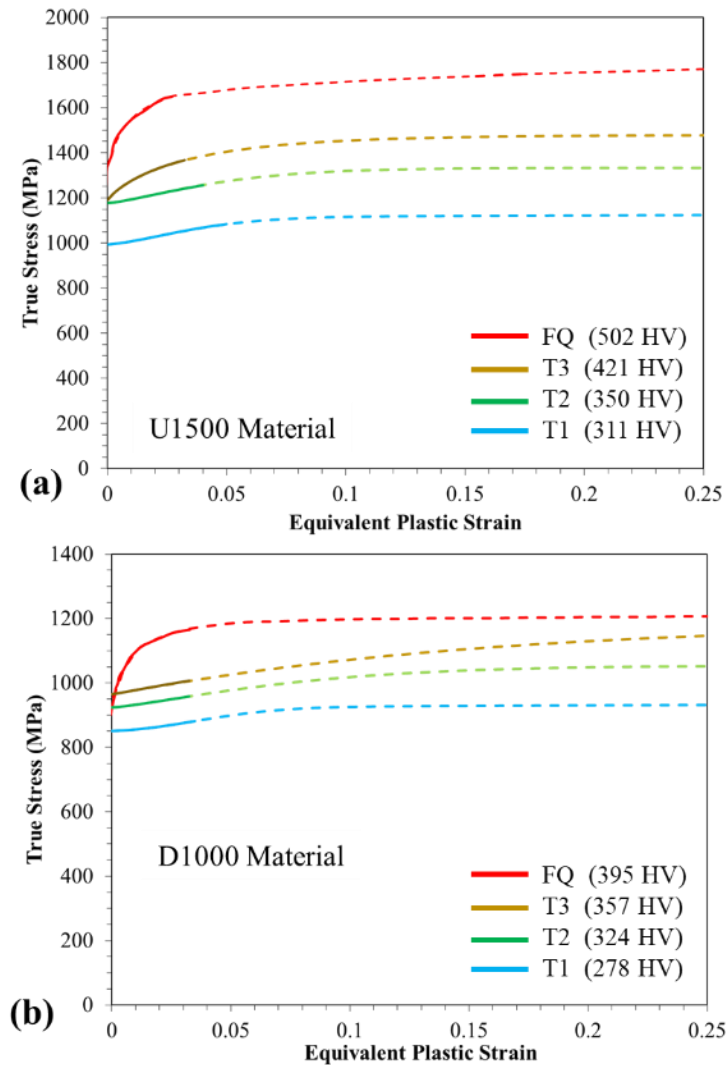


Figure 4-22. True stress versus equivalent plastic strain curves and fitted modified Hockett-Sherby constitutive models to the engineering stress-strain data in using Equation 4-3.

Table 4-3. Calibrated constants for the modified Hockett-Sherby material model (Equation 4-3)

Material	Condition	C_1 (MPa)	C_2 (MPa)	C_3	C_4	C_5 (MPa)	Mean Square Error (R^2)
U1500	FQ	1687	1360	14.1	0.66	170.24	0.99
	T1	1116	961	20	0.91	18.11	0.98
	T2	1332	1148	20	0.95	0	0.99
	T3	1480	1133	10.4	0.63	0	0.99
D1000	FQ	1177	854	19.9	0.64	56.05	0.97
	T1	924	825	20	0.93	17.68	0.98
	T2	1055	931	20	1.24	0	0.99
	T3	1176	975	8.8	1.16	10.36	0.99

4.5.4.2 Fracture Characterization

Figure 4-23 shows the measured fracture strains from V-bend tests for the HAZ and as-hot-stamped conditions for the U1500 and D1000 materials (the plane strain fracture strains for the U1500-FQ and D1000-FQ material condition were adopted from Samadian *et al.* [162] and Lee [161], respectively.) It can be seen that there is a linear relationship between the hardness and the measured fracture strain in plane strain for each alloy, shown in Figure 9 along with the R-squared values for the linear fits which are seen to be close to unity (≥ 0.97). Therefore, the plane strain fracture strains for the HAZ material conditions (tempered martensite microstructure) can be correlated to the local hardness.

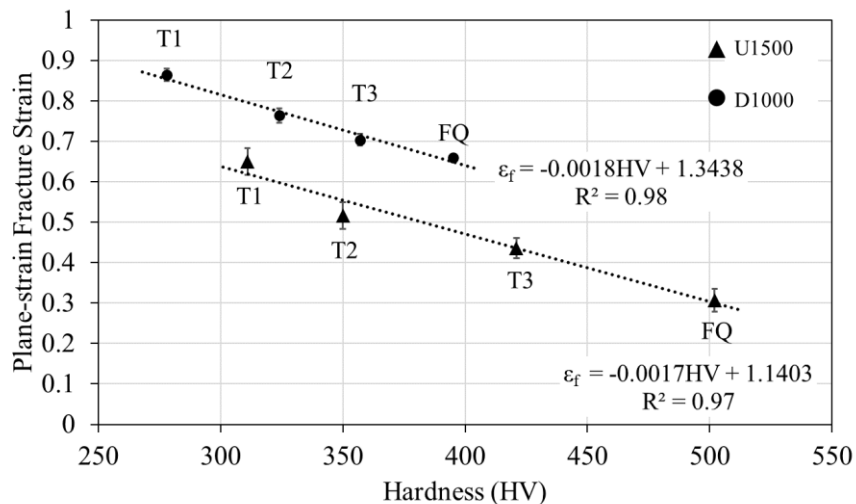


Figure 4-23. Linear relationship between fracture strain in plane-strain condition with the hardness of hot-stamped materials (Adopted from [162] and [161]) and HAZ material conditions.

In the absence of measured fracture strains for a broad range of stress states, the fracture loci for the as-hot-stamped (FQ) material were adopted as reference conditions. The fracture loci for the tempered martensite HAZ material conditions, *i.e.* T1, T2 and T3, were approximated by linearly translating the corresponding BM fracture loci based on the measured plane-strain fracture strain from the v-bend experiments. This assumption was made to minimize the testing needed for fracture characterization of the HAZ samples. The scaled 2D fracture loci are shown in Figure 4-24 and are appropriate for plane stress conditions, typical of sheet metal deformation, for which a unique relationship exists between the stress triaxiality (η) and Lode parameter ($\bar{\theta}$), as given by Wierzbicki and Xue [165]:

$$\bar{\theta} = -\frac{27}{2}\eta\left(\eta^2 - \frac{1}{3}\right) \quad \text{Equation 4-4}$$

in which η is defined as the ratio of hydrostatic stress to von Mises equivalent stress and $\bar{\theta}$ is the Lode angle parameter which takes the effect of deviatoric stresses into account [101]. The adopted fracture loci for U1500-FQ and D1000-FQ (shown as solid lines in Figure 4-24a and b, respectively), were linearly shifted to match the measured fracture strains in the plane-strain condition from the v-bend experiments (triaxiality of 0.57), plotted as symbols in the figures. The shifted fracture curves for the HAZ material conditions are shown as dashed lines.

Within the spot weld and HAZ, a fully three-dimensional stress state exists, thus, the available two-dimensional fracture loci (Figure 4-24) were used to fit a three-dimensional fracture locus for each material condition. For this purpose, the Bai-Wierzbicki fracture locus [166] was adopted, which is expressed as:

$$\begin{aligned} \varepsilon_f(\eta, \bar{\theta}) = & \left[\frac{1}{2}(D_1 e^{-D_2 \eta} + D_5 e^{-D_6 \eta}) - D_3 e^{-D_4 \eta} \right] \bar{\theta}^2 \\ & + \frac{1}{2}(D_1 e^{-D_2 \eta} + D_5 e^{-D_6 \eta}) \bar{\theta} + D_3 e^{-D_4 \eta} \end{aligned} \quad \text{Equation 4-5}$$

in which ε_f is the fracture strain and D_1 to D_6 are calibration constants. To illustrate the process used to fit the three-dimensional fracture loci, the failure strain versus triaxiality data from the two-dimensional plane stress fracture locus for each material condition (from Figure 4-24) were replotted as a function of triaxiality and Lode parameter, using the relationship between triaxiality and Lode parameter, described by Equation 4-4. Each fracture locus was discretized as 100 data points spaced out using increments in triaxiality of 0.01 over a triaxiality range of -1/3 to 2/3. This data set was then

used to fit the three-dimensional Bai-Wierzbicki fracture surface (Equation 5) for each material condition using a Levenberg–Marquardt procedure available in the OriginPro software [167,168].

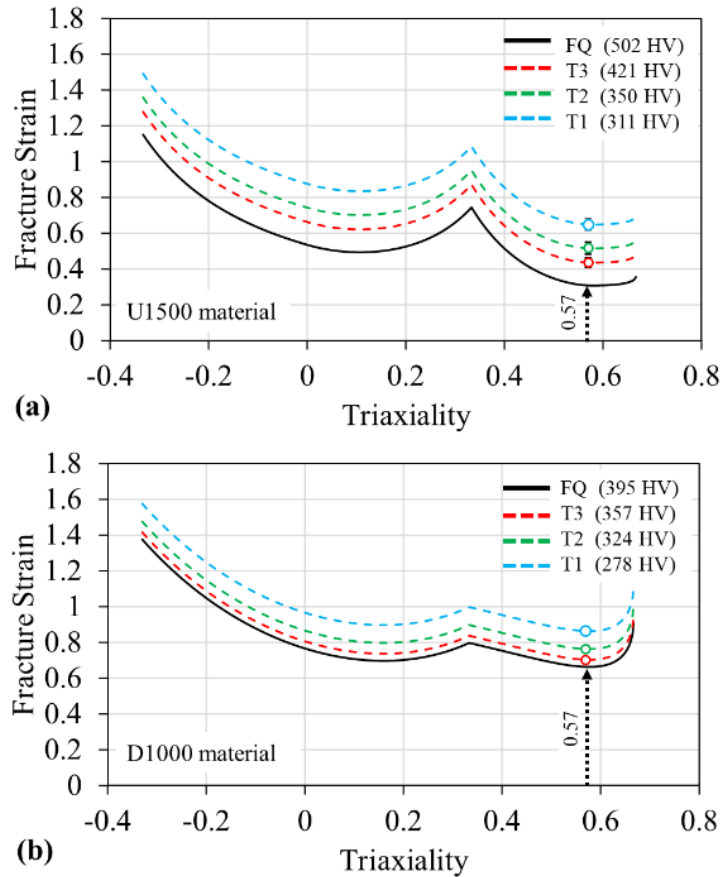


Figure 4-24. Fracture loci for hot-stamped U1500 and D1000 (adopted from [162] and [161]) and HAZ materials using linear interpolation based on hardness.

The resulting three-dimensional fracture loci are shown as contour plots in Figure 4-24. The calibrated constants of the Bai-Wierzbicki fracture surface are listed in Table 4-4, along with the calculated mean squared error which was equal to or larger than 0.95 for all fits indicating that the three-dimensional fits match with the two-dimensional fracture curves relatively well. It is worth noting that the three-dimensional fracture loci were extrapolated to a triaxiality level of 2 to encompass more severe stress states for numerical simulation purposes. Although the higher triaxiality values were not experimentally calibrated, it was assumed that the Bai-Wierzbicki model is still valid over the extended range. More details on the local material property measurements, constitutive modeling and fracture characterization can be found in Appendix E.

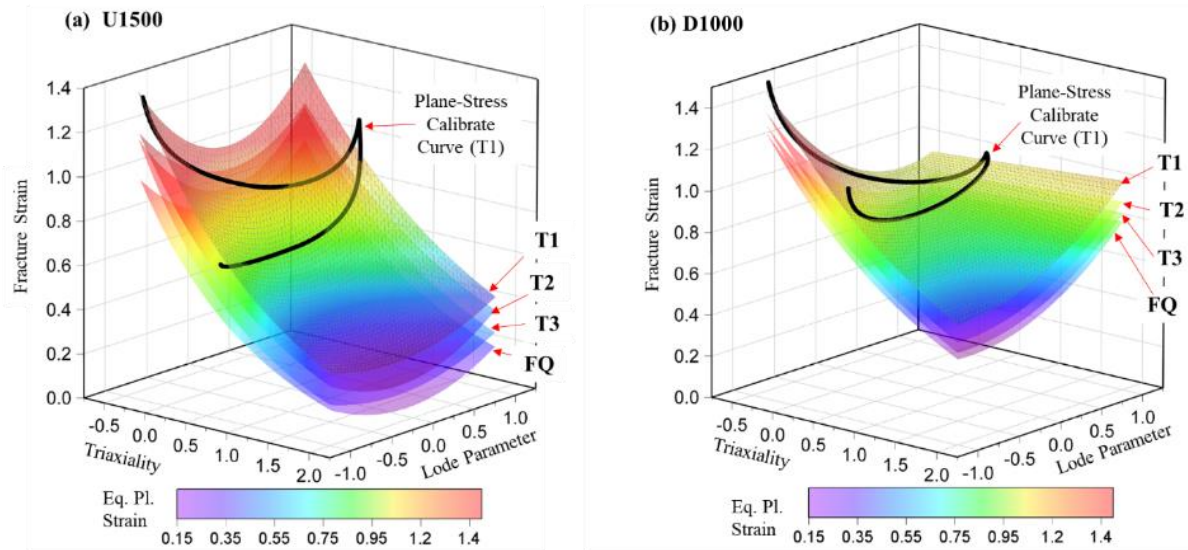


Figure 4-25. 3D Bai-Wierzbicki fracture loci calculated from the 2D plane stress fracture loci in Figure 13 (a) U1500, and (b) D1000. The plane stress loci corresponding to the T1 material condition are also plotted for each alloy (solid curves).

Table 4-4. Calibrated constants for the Bai-Wierzbicki fracture surface equation (Equation 4-5)

Material	Condition	D_1	D_2	D_3	D_4	D_5	D_6	Mean Square Error (R^2)
U1500	FQ	0.76	0.74	0.51	1.07	0.76	0.96	0.96
	T1	1.10	0.48	0.85	0.56	1.13	0.62	0.96
	T2	0.97	0.55	0.72	0.68	0.99	0.72	0.96
	T3	0.89	0.61	0.63	0.80	0.90	0.80	0.96
D1000	FQ	0.75	-0.04	0.75	0.20	1.09	0.48	0.99
	T1	0.95	-0.03	0.95	0.16	1.30	0.40	0.98
	T2	0.85	-0.04	0.85	0.18	1.20	0.44	0.98
	T3	0.79	-0.04	0.79	0.19	1.13	0.47	0.98

To implement failure in LS-DYNA for the hot-stamped and HAZ materials, the evolution of damage was predicted using the GISSMO criterion described by Equation 2-5, as was discussed in Section 2.8.2. The damage exponent, n , was set equal to 2 as recommended by Samadian *et al.* [162] and Lee [161] for U1500 and D1000, respectively. Here, the failure strain, $\bar{\epsilon}_f$, for a given triaxiality and Lode angle parameter, is determined by the fracture loci in Figure 4-25, given by Equation 4-5 and the constants in Table 4-4. This damage-based approach is utilized since the fracture loci in Figure 4-25 are strictly valid for under proportional loading paths, while the GISSMO approach given by

Equation 4-5 accounts for non-proportional loading. In the finite element simulations, when D reaches a value of unity, the corresponding element is flagged as failed and is deleted. In view of the rather fine element size (~ 0.06 mm), mesh regularization was not considered [169] and mesh convergence studies were left for future work.

4.5.5 Meso-Scale Spot Weld Failure Simulation

Using the local material properties in Section 4.5.4 and the detailed spot weld geometry previously discussed in Section 4.5.3, the damage accumulation and failure were simulated for normal and shear loading of the 1.6 mm U1500-FQ and D1000-FQ spot welds. The goal of this part of the work is to be able to predict spot weld failure considering the micro-scale features such as the location of failure and through thickness damage progression, as well as macro-scale behavior including failure mode (*i.e.* pull-out, partial pull-out, and interfacial) and global load-displacement response. To validate the simulation results, the results were compared to the experimental results obtained in Task 3. In the following sections, the results are categorized and discussed with respect to the loading and material conditions.

4.5.5.1 Spot Weld Failure under Normal Loading

The predicted failure behavior of spot welds under normal loading (CT) is shown in Figure 4-26. The contour plots of damage parameter are on the right and the failure path with respect to the spot weld sub-regions for spot welds under normal loading is on the left side of each plot. As seen in Figure 4-26a to c, damage is initially accumulated at the weld notch for the U1500-FQ-with-halo sample leading to weld notch cracking, also known as corona debonding [52]. Then, damage proceeds along the halo ring as seen in Figure 4-26b. Final failure occurs by abrupt fracture of the HAZ material when the remaining ligament become critically small (Figure 4-26c). This predicted behavior corresponds to a mode 2 partial thickness fracture with button pull in accordance with AWS D8.1 [23].

In the absence of the halo ring, however, the failure occurs along an irregular path parallel to loading direction (Figure 4-26d and e). Although the location of final failure appears to be similar for the samples with and without the halo ring, the fracture surface of the sample without the halo ring propagates through the softened HAZ (Figure 4-26f) compared to the sample with the halo ring (Figure 4-26c). For the D1000-FQ spot weld (Figure 4-26g to i), the level of damage accumulated next to the actual failure path is significantly higher than that of U1500-FQ spot welds, which reflects

the higher fracture strain and lower flow stresses for the D1000-FQ material. Similar to the U1500-FQ-no-halo sample, the failure path for the D1000-FQ spot weld remains parallel to the loading direction in the absence of a transient softened zone at the fusion boundary. Again, the predicted failure mode matches with the description of mode 1 button pull-out failure in accordance with AWS D8.1 [23]. Overall, the predicted failure behavior of the spot welds under shear loading are significantly affected by the local material properties.

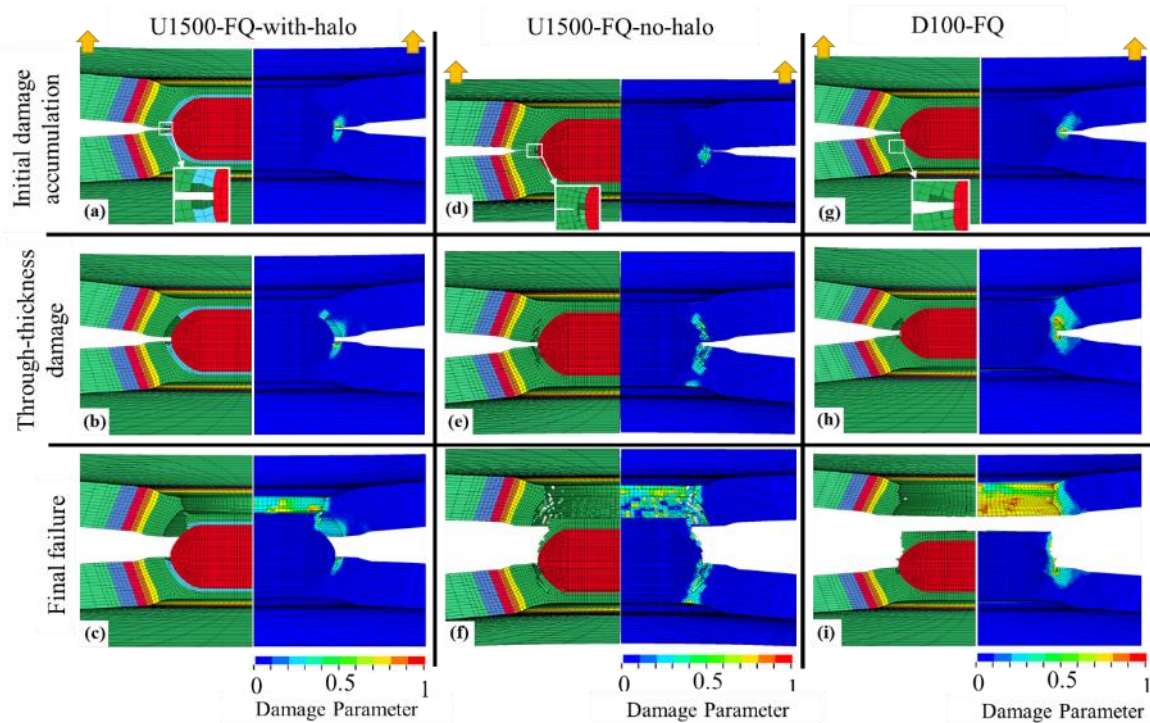


Figure 4-26. Failure simulation results for spot welds under normal loading showing the location of failure and damage progression through the thickness for (a), (b) and (c) U1500-FQ-with-halo, (d), (e) and (f) U1500-FQ-no-halo, and (g), (h) and (i) D1000-FQ spot welds. Loading direction is shown by orange arrows.

4.5.5.2 Spot Weld Failure under Shear Loading

The shear load simulation results for the spot weld failure are shown in Figure 4-27. For the U1500-FQ-with-halo spot weld (Figure 4-27a to c), damage is initially accumulated at the weld notch. As seen in Figure 4-27b, the damage is gradually accumulated along the halo ring leading to a curved failure path at the fusion boundary. The final fracture occurs due to rapid fracture through the thickness of the sheet as the remaining ligament becomes critically small (Figure 4-27c). This prediction matches with the description of mode 2 partial thickness fracture with button pull in the

AWS D8.1 [23]. In the absence of the halo ring, damage accumulation occurs within the softened HAZ for the U1500-FQ-no-halo spot weld (Figure 4-27d to f). Note that the failure location depends on the presence of the halo. When the halo is present, failure occurs at the fusion boundary (Figure 4-27c), however, in the sample without the halo, failure occurs through the softened HAZ (Figure 4-27f) leading to mode 1 button pull-out failure mode. Although both failure modes are categorized as pull-out, due to the difference in the location of failure, the type of pull-out failure under shear loading is altered by the presence of the halo ring. For the D1000-FQ spot weld (as shown in Figure 4-27g to i), after initial damage accumulation at the weld notch, local shearing is predicted at the interface of the sheets which leads to mode 7 interfacial failure of the D1000-FQ spot weld.

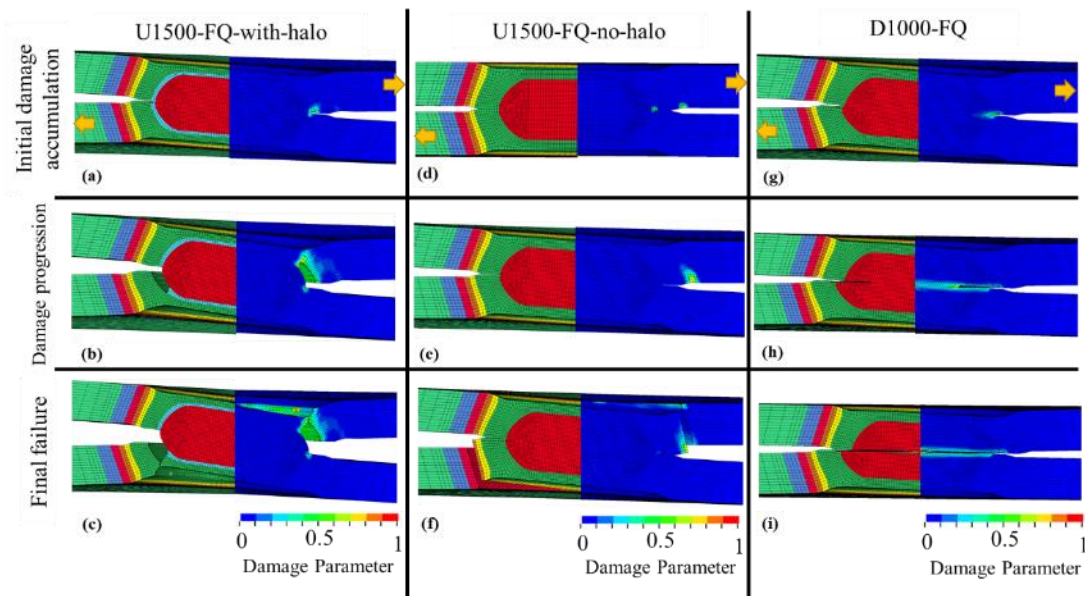


Figure 4-27. Failure simulation results for spot welds under normal loading showing the location of failure and damage progression through the thickness for (a), (b) and (c) U1500-FQ-with-halo, (d), (e) and (f) U1500-FQ-no-halo, and (g), (h) and (i) D1000-FQ spot welds. Loading direction is shown by orange arrows.

4.5.5.3 Comparison with Experiment

To validate the simulation results, direct comparison of the predicted and observed failure characteristics of the spot welds was performed. From Figure 4-26 and Figure 4-27, all spot welds are predicted to fail in one of two pull-out modes (mode 1 pull-out or mode 2 partial thickness failure), with the exception of the D1000 spot weld which failed inter-facially under shear loading (mode 7).

These predictions align well with the observed failure modes that are evident in the post-failure macro-images shown in Figure 4-8.

For more in-depth analysis of spot weld failure and prediction capabilities, the cross-sections of the spot welds were examined after failure and compared with the predicted results (as shown in Figure 4-28). It was seen that the overall predicted path and location of failure matched with the experiments for all the spot welds studied in the present work. In the presence of the halo ring in the U1500-FQ welds (Figure 4-28a and d), failure occurred along the fusion boundary, which had a local hardness of 402 HV and was lower than the BM hardness of 505 HV. The results indicate that the models are capable of capturing this rather complex failure mode (mode 2 partial thickness fracture with button pull), accounting for the presence of the halo ring. The failure through the halo ring, which is a 100 μm wide region surrounding the FZ of U1500-FQ, is explained in detail in Appendix B. It should be noted that the hardness of the halo is still higher than that of the softened HAZ, which had a hardness of 305 HV; nevertheless, failure occurred within the halo ring due to local material inhomogeneity and strain accumulation.

By eliminating the halo ring in the U1500-FQ welds, failure occurred parallel to the normal load starting from the weld notch towards the surface (Figure 4-28b). However, the U1500-FQ-no-halo welds fail at the softened HAZ under shear loading (as shown in Figure 4-28e) which is the weakest part of the weld according to the hardness measurements (Figure 4-28b). The predicted failure at the softened HAZ for the U1500-FQ-no-halo case matches the experiment as well as the mode 1 button pull-out failure described by AWS D8.1 [23]. The predicted failure path is mostly dominated by the rather low strength at the softened HAZ (which has local material properties corresponding to the softest T1 region) with a minimum hardness of 278 HV (Table 4-2).

In the D1000-FQ spot weld, failure is initiated at the weld notch and propagates through the thickness under normal loading, as shown in Figure 4-28c. This is in agreement with the identified failure mode for the D1000-FQ spot weld under normal loading in Figure 4-8 and the definition of mode 1 partial button pull-out failure. With the weld dimensions in the present work, the weld in D1000-FQ failed interfacially under shear loading (Figure 4-28f).

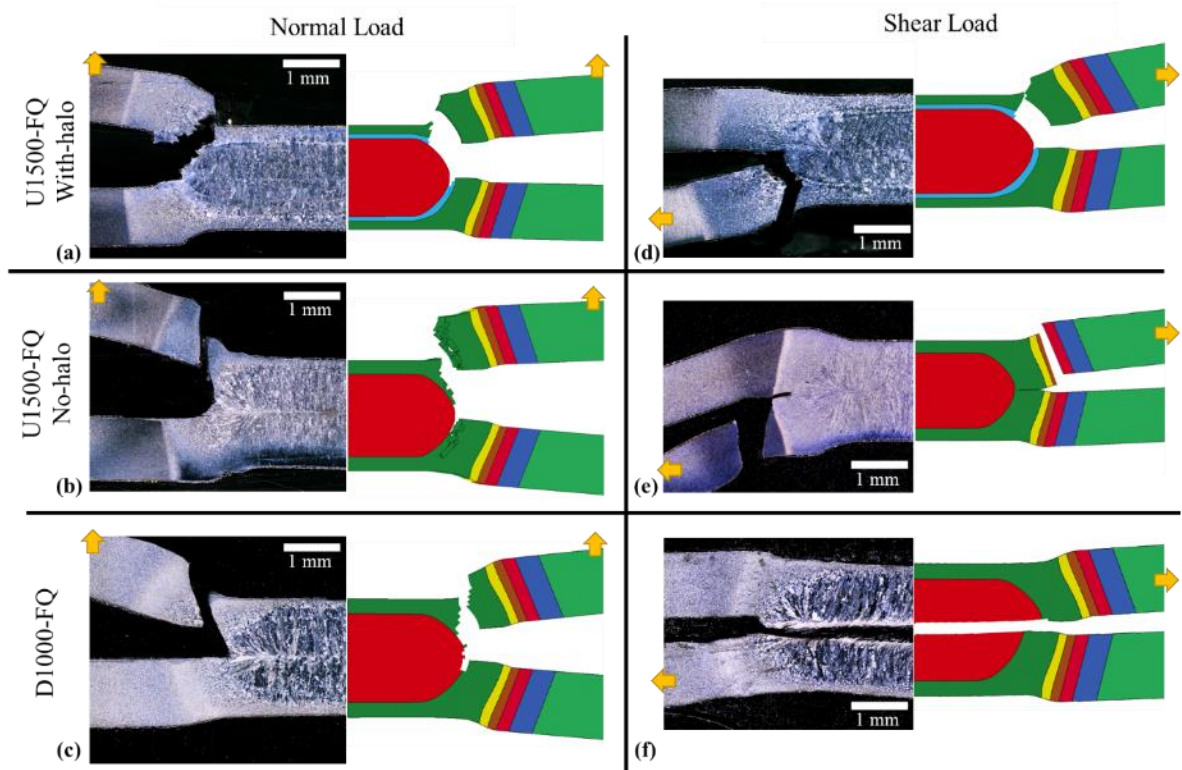


Figure 4-28. Predicted versus experimentally examined cross-section of spot welds showing the location of failure under (a), (b) and (c) Normal loading, and (d), (e), and (f) shear loading for different spot weld conditions.

It was previously shown in Section 4.4.3 that the interfacial failure exhibited shear-dominant plastic flow, which contrasts the common assertion that interfacial failure occurs as a brittle fracture [31,156]. The predicted failure behavior agreed with the experimental observations in the present work and showed that the D1000-FQ spot weld failed under shear loading, as seen by the predicted effective plastic strain field shown in Figure 4-29. The sheared edge of the fractured surface along the center line of the weld is clearly seen in Figure 4-29a. The effective plastic strain contour for the same test condition (Figure 4-29b) shows extensive plastic deformation within the elements adjacent to the fractured edge. In addition to the major shearing at the center, there is a degree of thinning at the softened HAZ (indicated by orange arrows in Figure 4-29a) as a result of a competition between strain accumulation at the weld notch and the softened HAZ at the early stages of the test. Some thickness reduction was predicted at the softened HAZ where the plastic strain was on the order of 0.13. Thus, localization initiated at the HAZ, however, shearing across the weld nugget proved to be the dominant failure mode.

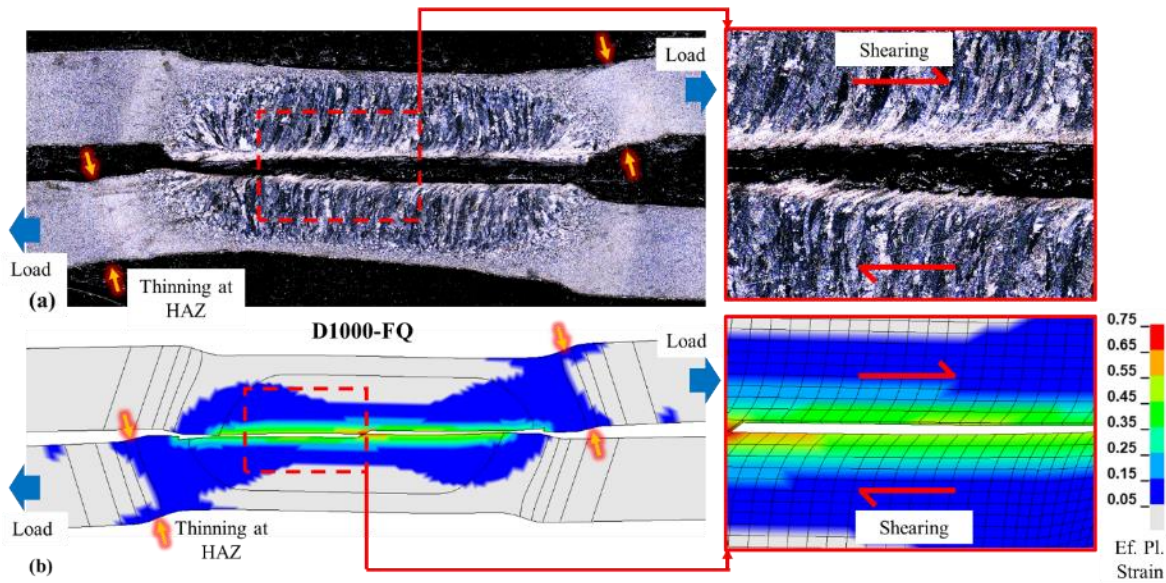


Figure 4-29. Post-failure analysis of interfacial failure in D1000-FQ spot weld.

4.5.5.4 Strain History and Stress State at the Onset of Failure

The strain-stress state history of the critical element, defined here as the element at which failure (and element deletion) first occurs, as described by Equation 4-5, provides insight regarding the conditions leading to onset of failure within the studied spot welds. Figure 4-30 shows an example of the predicted strain-stress state history leading to failure under lap shear loading for the U1500-FQ-with-halo. Also plotted is the three-dimensional Bai-Wierzbicki failure surface and the plane stress failure locus for the critical element. Finally, additional plots of strain versus triaxiality and strain versus Lode parameter are plotted to assist in visualizing the stress state history.

Under shear loading, the U1500-FQ-with-halo spot weld exhibits mode 2 partial thickness fracture and pull-out and the critical element is located at the halo ring (as indicated in the mesh plot inset in Figure 4-30). Based on the strain-stress state history, the triaxiality increases rapidly to values of 1.7 during the early stages of deformation, decreasing to approximately 0.85 at fracture. After the initial transient, the Lode parameter is approximately 0 for the majority of the deformation history. Thus, the stress state within the weld is severe, due to the high predicted triaxiality, which can be attributed to the differing microstructures within the weld region, with the softer phases experiencing a high degree of constraint imposed by the surrounding harder phases.

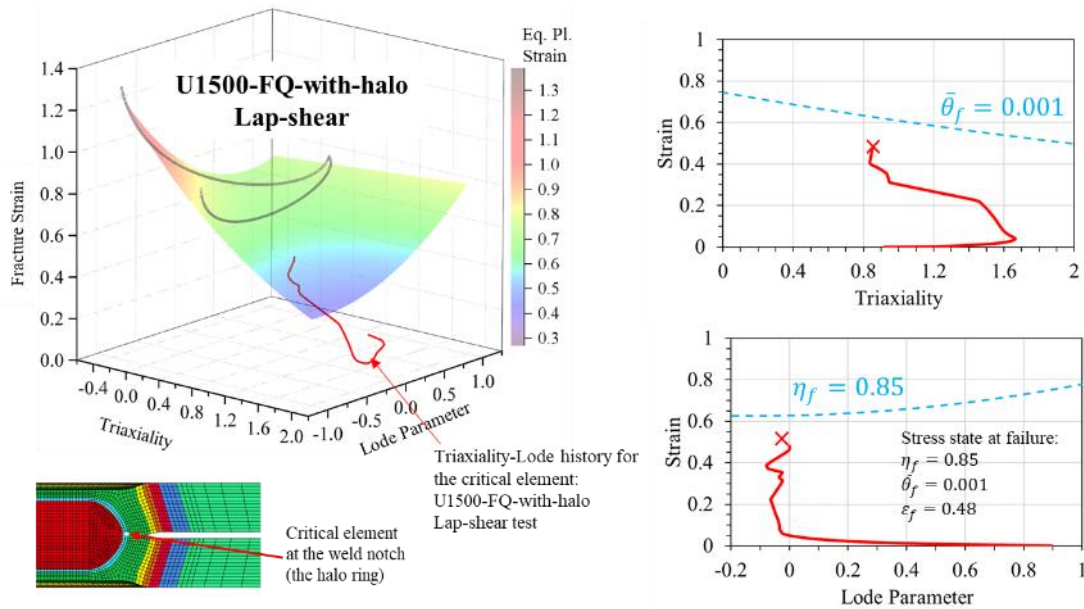


Figure 4-30. Predicted strain-stress state history of the critical element for U1500-FQ-with-halo spot weld in lap-shear test. Critical element is shown in the inset finite element mesh.

With one exception, the other loading cases (not shown for brevity) all exhibited pull-out failure modes with predicted strain-stress state histories that had high triaxiality levels that were similar to that show in Figure 4-30. In this regard, the shear-dominated failure mode of the lap shear-loaded D1000-FQ spot weld was distinct from the other load cases. Figure 4-31 shows the predicted strain-stress state history results for the D1000-FQ spot weld; for this case, the critical element is located at the centerline of the weld, within the FZ. The interfacial failure (mode 7) occurs as a result of shearing along the interface of the sheets (Figure 4-28). The strain-stress state history corresponds to a pure shear condition, with triaxiality and Lode parameter values close to zero. This observation confirms the shearing mechanism of interfacial failure for the D1000-FQ spot weld under shear loading (lap-shear).

The high triaxiality predicted for the U1500-FQ-with-halo spot weld lies well beyond the highest triaxiality encompassed by the fracture calibration data which is limited to biaxial tension under through-thickness plane stress conditions ($\eta=0.66$, $\bar{\theta} = 0$). Thus, the current Bai-Wierzbicki failure surfaces represent extrapolations and there exists a need to develop additional high triaxiality experiments to more accurately characterize the fracture limits of the phases present in the weld region. It is also important to restate that the fracture limits of the halo ring were assumed to

correspond to that of the D1000-FQ condition. Direct measurement of the fracture limits of the halo ring will prove difficult given its extremely small thickness (104 μm) [34].

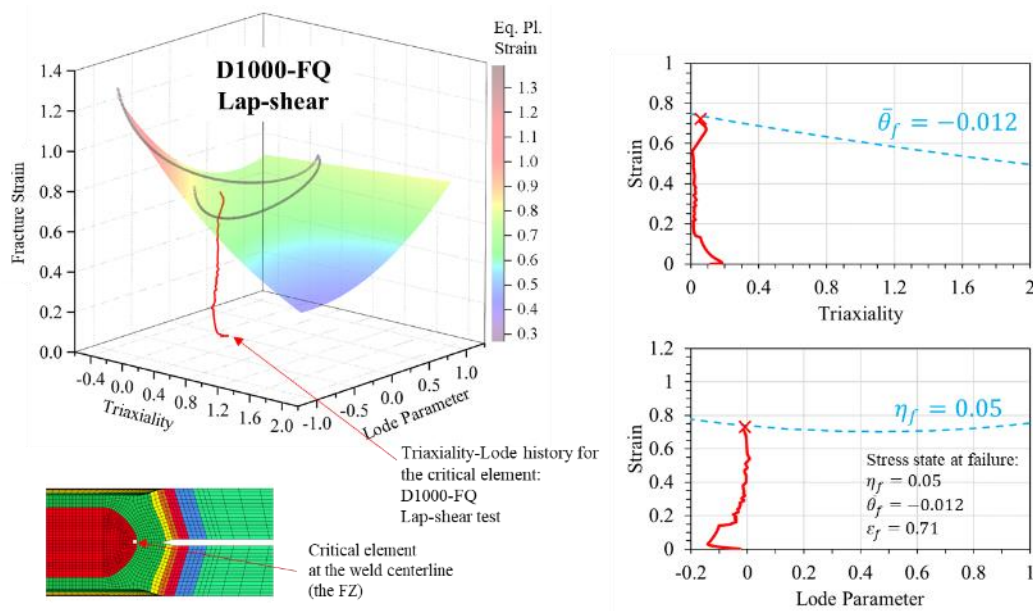


Figure 4-31. Predicted strain-stress state history of the critical element for D1000-FQ spot weld in lap-shear test. Critical element is shown in the inset finite element mesh.

4.5.5.5 Load-Displacement and Absorbed Energy Prediction

The predicted and measured load-displacement and total absorbed energy for the lap-shear and cross-tension tests are compared in Figure 4-32. Overall, the load-displacement response of the studied spot welds matches well with the experiments (within $\pm 9\%$ relative error). In addition, the predicted load and displacement corresponding to the onset of failure are also within 6.3% of the measured values. The detailed meso-scale models developed in this work are able to predict the non-linearity of the load-displacement response during both the loading phase as well as post-failure energy absorption, which is difficult to capture with the existing structural spot weld models that employ beam and shell element formulations, as reported in studies by Tolton [49], Khandokar *et al.* [170], and Sadigh *et al.* [171].

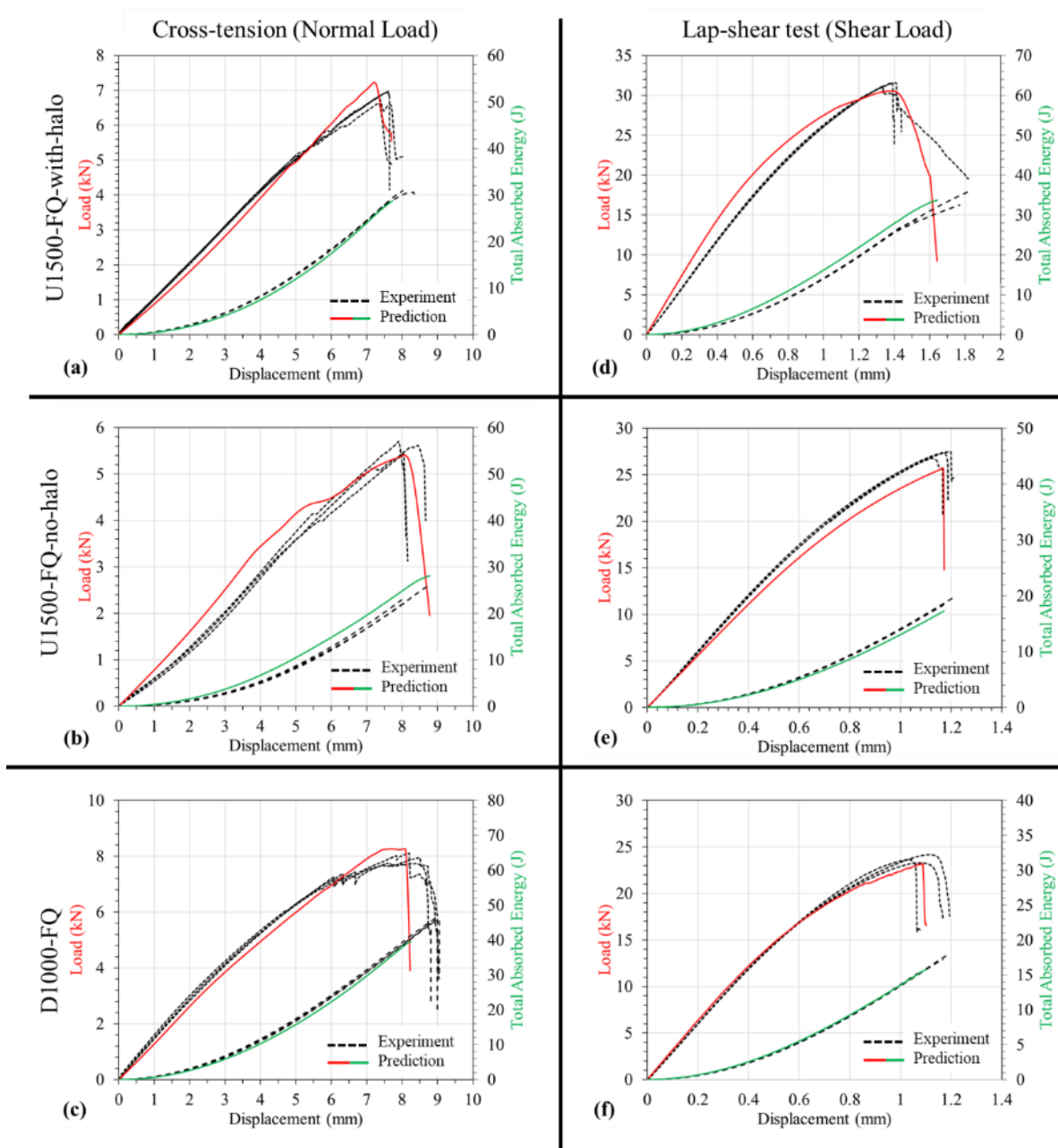


Figure 4-32. Comparison of predicted and experimental load-displacement curves for different spot welds under (a), (b) and (c) under normal, and (d), (e), and (f) under shear loading.

The capability of the developed 3D meso-scale models in predicting the peak load value for the spot welds is demonstrated in Figure 4-33. In terms of the overall prediction accuracy, the predicted peak loads are within $\pm 7\%$ relative error range. According to the calculated errors, all the peak load data for shear loading are underestimated with relative error between 2.2 and 5.4 %; with the U1500-

FQ-no-halo condition having the highest error. On the other hand, the peak load values for normal loading are overestimated within the relative error range between 3.2 and 6.3 %, with the maximum error calculated for the U1500-FQ-AS-with-halo spot weld. The potential sources of error include the relatively coarse discretization of the weld region and the reduced simulation domain size considered in the current models. Despite these modest errors, the current meso-scale models capture the rather diverse failure modes and resulting fracture paths, failure loads and energy absorption rather well. More details about the meso-scale spot weld failure models, simulation results and validations can be found in Appendix E.

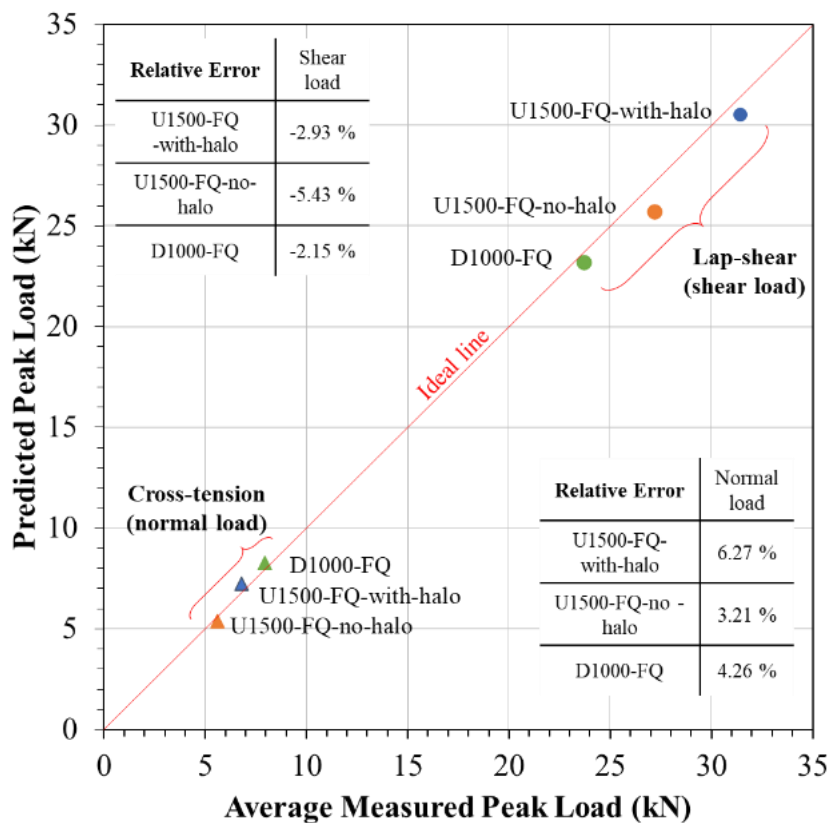


Figure 4-33. Predicted versus measured peak load data for different spot welds and loading conditions.

4.6 Summary

Experimental characterization of spot weld failure is a challenging task due to the complex loading conditions around the weld nugget and limited available techniques for *in-situ* failure analysis. As a

result, most current spot weld failure models only consider global behaviour of spot welds, such as peak load, for failure prediction. Therefore, the effects of microstructure, local material properties, and through-thickness damage progression on failure behavior of spot welds are neglected in the current models.

In the present research, four different tasks were executed to build-up the required foundations for developing a meso-scale spot weld failure model which is capable of through thickness damage prediction based on the local material properties of the weld region. According to Figure 2-21, several deliverables were targeted these tasks to address the main goal of each task. For Task 1, the goal was to develop RSW process parameters for expulsion-free spot welds with optimum strength for several hot-stamping automotive steel grades and thicknesses. To this end, a systematic optimization process (combination of experiment and modeling) was performed on the heat-treated materials and unified sets of RSW parameters were reported for each material thickness.

For Task 2, the microstructure of the spot welds was examined and sub-regions within the welds were identified. A correlation between microstructure and microhardness was established which was used as the basis for generating the spot weld geometry in Task 4. For the hot-stamped materials studied here, martensite tempering is the main cause of softening at the SC-HAZ. Additionally, a transient softened zone, referred to as the halo ring, was found in the U1500-FQ spot welds creating local material nonuniformity within a narrow band at the fusion boundary.

Using the results from Task 2, an in-depth analysis of failure under shear and normal loading was performed in Task 3 with respect to the local microstructure of subregions. It was found that the presence of the halo ring for the U1500 spot welds alters the failure path and slightly affects the total absorbed energy during failure. To address one of the main goals of the present work under Task 3, a novel testing technique that uses DHW specimens was coupled with DIC analysis which allowed for *in-situ* through-thickness damage progression analysis. The capability of the DHW testing technique for failure analysis was demonstrated by promoting different failure modes, including partial pull-out, complete pull-out, and interfacial failure, using modified RSW parameters. It was found that failure occurs along the halo ring in the U1500-FQ spot welds leading to partial pull-out failure. In contrast to the common assertion that interfacial failure occurs as brittle fracture, the *in-situ* failure analysis showed shear-dominant type of failure for interfacial failure of the D1000-FQ spot welds.

In Task 4, meso-scale spot weld models were developed by discretizing weld regions based on microstructure-failure relationships found in Task 2 and Task 3. To this end, local material properties

(including constitutive flow models and fracture surfaces) for the FZ, BM, and HAZ were experimentally measured and modeled to be used in FEA. The variations of local material properties were correlated to hardness/microstructure change within spot weld subregions and mapped over the detailed spot weld geometry. The developed meso-scale failure models were used to predict microscopic failure path and damage progression, as well as macro-scale failure modes and load-displacement response of spot welds under shear and normal load. The predictions in Task 4 were compared and validated against the experimental results obtained in Task 3, showing good agreement at both the macroscopic level (load-displacement) and capturing the failure paths at the microscopic level rather well.

Chapter 5

Conclusions and Future Work

5.1 Conclusions

The present study established methods for experimental spot weld failure analysis and numerical failure prediction by taking the effect of microstructure and local material properties into account. For the first time, the sequence of crack propagation and through-thickness damage progression during spot weld failure were measured through the cross-section and numerically modeled using a hardness/microstructure mapping approach. This was identified partially through the use of a novel *in-situ* failure characterization technique coupled with DIC, as well as finite element simulation failure in which local material properties were assigned based on hardness to the detailed meso-scale spot weld models with fine 3D elements. Based on the predictions, the state of stress in the weld zone can be quite severe (triaxiality higher than unity), largely due to the interactions between the adjacent hard and soft zones during deformation, which highlights the need for future high triaxiality fracture characterization. The main conclusions are described in detail below:

1. For the studied spot welds in the hot-stamped materials, *i.e.*, U1500, D1000, and D500, HAZ softening occurred due to martensite tempering and/or decomposition of the BM within the SC-HAZ. For the U1500-FQ spot weld a transient softened zone at the fusion boundary, referred to as the halo ring, was observed which is thought to form due to carbon depletion during the spot welding process. Using a multi-pulse RSW schedule with 65 ms pulses, the halo ring was eliminated while maintaining the same weld size.
2. Macrostructure observations revealed that all of the spot welds created by the optimized welding settings fail in pull-out mode (partial through-thickness pull-out or complete pull-out) under normal and shear loading. However, the failure path and location of failure depends on the microhardness variation across the weld and sheet thickness. It was found that failure occurs via partial thickness fracture and button pull out for U1500-FQ and D1000-FQ with stronger BM. The tendency for partial through thickness fracture increases with increasing the sheet thickness.
3. Failure within the softened HAZ was the dominant location of failure under shear loading for all spot welds created with the optimized setting, the typical failure location for spot welds in AHSS grades, except the U1500-FQ spot welds. Failure in the U1500-FQ spot weld was

observed at the halo ring which is a ~100 μm wide region around the weld nugget with the minimum hardness of 472 HV although it is not the lowest hardness point of the weld. Due to the geometrical constraints and high strength of the fusion zone, the majority of the spot welds failed via pull-out close to the CG-HAZ under normal loading.

4. Post-failure optical and electron microscopy on an interrupted lap-shear test revealed that failure occurs via shear band formation at the halo ring, which has not been reported before for the U1500-FQ material. S-shaped shear patterns were found on the fracture surface of the weld next to the nugget, indicating severe shearing during failure at the halo ring.
5. The novel DHW testing samples coupled with DIC technique showed that spot weld failure in U1500-FQ initiates at the weld notch by corona debonding regardless of the spot weld microstructure. However, in the presence of the halo ring, fracture follows the curvature of the halo ring leading to partial thickness fracture with button-pull out failure. In the absence of the halo ring, failure occurs parallel to the normal load or within the softened HAZ under shear loading which decreases the strength of the spot weld.
6. The DHW testing method also enabled *in-situ* observation of interfacial failure for the first time. A modified RSW setting was used to promote interfacial failure in the D1000-FQ welds. The results showed extensive shearing at the centerline of the weld nugget after initial corona debonding at the weld notch. This interpretation of interfacial failure is in contrast with the common understanding that interfacial failures are brittle in nature. Post-failure fractographs showed ductile fracture at the central region of the weld nugget, as evidence of the plastic shear-dominant mechanism of interfacial failure.
7. The models were able to predict the microscopic location of failure and through-thickness damage progression as well as macro-scale failure mode and load-displacement response of the spot welds (within 6.3% of measured failure loads).
8. The predicted strain-stress state histories revealed high triaxiality levels (in the range of 0.95 to 1.7) for the welds experiencing pull out failure modes. These high levels of triaxiality are attributed to constraint on deformation of the softer phases imposed by the adjacent harder regions including the FZ and upper-HAZ. The current Bai-Wierzbicki failure surfaces represent extrapolations from the measured data, thus, there exists a need to develop

additional high triaxiality experiments to more accurately characterize the fracture limits of the phases present in the weld region.

5.2 Recommendation for Future Work

The following future work is recommended as next steps to strengthen the understanding of spot weld failure behavior analysis and numerical modeling:

- The presence of the transient softened zone at the fusion boundary for U1500 material was observed in the present work. However, the root cause of its formation, microstructure, chemical composition, and practical methods to control the width and hardness of the softened zone are left for future work. Based on the results in the present work, it is expected that the state of the transient softened zone could affect the failure behavior significantly.
- In the current study, the local material characterization was performed using the indirect method by reproducing the HAZ materials. Several simplifying assumptions were made to minimize the number of required experiments. In-depth fracture characterization of the HAZ using micro-scale testing methods is recommended for future work which should improve predictions of spot weld failure response.
- The present work was mostly focused on the development of hardness-mapping methodology for spot weld failure modeling. Therefore, the required material cards for the discretized geometry were manually implemented into LS-DYNA. An important feature that should be added in future is the development of User-defined Material (UMAT) subroutines for automatic and smooth allocation of material properties to the spot weld geometry. UMATs can be used to define new spot weld geometries as RSW parameters change and to update the constitutive flow models and fracture limit strains.
- To establish the foundation for the modeling methodology and the experimental techniques for failure analysis, coupon size testing and simulation were used in the present work. Considering the application of the hot-stamped automotive steels for large parts, component level testing and meso-scale simulation would be valuable.
- The predicted strain-stress state histories revealed high triaxiality levels for the welds experiencing pull out failure modes. The observed range of triaxiality is higher than the

range for typical sheet metal fracture characterization. Therefore, additional high stress triaxiality tests are required to calibrate the fracture loci for spot weld failure.

Letters of Copyright Permission

Letters of Copyright Permission

Figure 2-1

Source: Karbasian H, Tekkaya AE. A review on hot stamping. J Mater Process Technol 2010;210:2103–18. <https://doi.org/10.1016/j.jmatprotec.2010.07.019>. Figure 2

ELSEVIER LICENSE TERMS AND CONDITIONS

Jan 18, 2022

This Agreement between Dr. Alireza Mohamadizadeh ("You") and Elsevier ("Elsevier") consists of your license details and the terms and conditions provided by Elsevier and Copyright Clearance Center.

License Number	5231441055657
License date	Jan 17, 2022
Licensed Content Publisher	Elsevier
Licensed Content Publication	Journal of Materials Processing Technology
Licensed Content Title	A review on hot stamping
Licensed Content Author	H. Karbasian,A.E. Tekkaya
Licensed Content Date	Nov 19, 2010
Licensed Content Volume	210
Licensed Content Issue	15
Licensed Content Pages	16
Start Page	2103
End Page	2118
Type of Use	reuse in a thesis/dissertation
Portion	figures/tables/illustrations
Number of figures/tables/illustrations	1
Format	electronic
Are you the author of this Elsevier article?	No
Will you be translating?	No
Title	Characterization and microstructure-based modeling of spot weld failure in hot stamped steel
Institution name	University of Waterloo
Expected presentation date	Jan 2022
Portions	Figure 2
Requestor Location	Dr. Alireza Mohamadizadeh 200 University Avenue N2L 3G1 Waterloo, ON N2L 3G1 Canada Attn: Dr. Alireza Mohamadizadeh
Publisher Tax ID	GB 494 6272 12
Total	0.00 CAD
Terms and Conditions	

Figure 2-2

Source: Merklein M, Wieland M, Lechner M, Bruschi S, Ghiotti A. Hot stamping of boron steel sheets with tailored properties: A review. J Mater Process Technol 2016;228:11–24.

<https://doi.org/10.1016/j.jmatprotec.2015.09.023>. Figure 3 and Figure 7

ELSEVIER LICENSE TERMS AND CONDITIONS

Jan 18, 2022

This Agreement between Dr. Alireza Mohamadizadeh ("You") and Elsevier ("Elsevier") consists of your license details and the terms and conditions provided by Elsevier and Copyright Clearance Center.

License Number	5231450647224
License date	Jan 17, 2022
Licensed Content Publisher	Elsevier
Licensed Content Publication	Journal of Materials Processing Technology
Licensed Content Title	Hot stamping of boron steel sheets with tailored properties: A review
Licensed Content Author	Marion Merklein,Michael Wieland,Michael Lechner,Stefania Bruschi,Andrea Ghiotti
Licensed Content Date	Feb 1, 2016
Licensed Content Volume	228
Licensed Content Issue	n/a
Licensed Content Pages	14
Start Page	11
End Page	24
Type of Use	reuse in a thesis/dissertation
Portion	figures/tables/illustrations
Number of figures/tables/illustrations	2
Format	electronic
Are you the author of this Elsevier article?	No
Will you be translating?	No
Title	Characterization and microstructure-based modeling of spot weld failure in hot stamped steel
Institution name	University of Waterloo
Expected presentation date	Jan 2022
Portions	Figure 3, Figure 7
Requestor Location	Dr. Alireza Mohamadizadeh 200 University Avenue N2L 3G1 Waterloo, ON N2L 3G1 Canada Attn: Dr. Alireza Mohamadizadeh
Publisher Tax ID	GB 494 6272 12
Total	0.00 CAD
Terms and Conditions	

Figure 2-4

Source: Online source <https://www.weldcor.ca/public/ckfinder/userfiles/files/FIGURE%20R-8.png> public access.

Re: Contact Request from WeldCor

Leroy Billesberger <leroy@weldcor.ca>

Mon 2022-01-17 6:22 PM

To: Alireza Mohamadizadeh <[REDACTED]>

Cc: Sales <Sales@weldcor.ca>

Hi Alireza

Feel free to use whatever information you want from our website. There's no need for a formal letter. Have a great day

Regards

Leroy Billesberger

President

WeldCor Supplies Inc

#8, 401 Pakwa Place

Saskatoon, SK S7L 6A3

Ph 1-306-974-9750

1-855-WeldCor (935-3267)

www.WeldCor.ca

Sent from my iPhone/iPad

On Jan 17, 2022, at 5:11 PM, Alireza Mohamadizadeh <a6mohama@uwaterloo.ca> wrote:

CAUTION:

This email originated from outside of the organization. Do not click links or open attachments unless you recognize the sender and know the content is safe.

Name	Alireza Mohamadizadeh
Company	University of Waterloo
Address	200 University Avenue
City	Waterloo
Country	CA
Province/State	ON
Postal Code/Zip Code	N2L 3G1
Email	[REDACTED]
Phone	[REDACTED]
Comments	<p>Hi,</p> <p>My name is Alireza Mohamadizadeh and I am writing to you from the University of Waterloo. I would like permission to include the material listed below in my PhD thesis. My project is on Characterization and microstructure-based modeling of spot weld failure in hot stamped steel.</p> <p>The material I wish to use: https://www.weldcor.ca/public/ckfinder/userfiles/files/FIGURE R-8.png</p> <p>As part of this project, the source for this material is clearly credited. Material is impartial in nature and is used, copied, and stored for educational purposes only.</p> <p>Please let me know how I can ask for this permission. I can send a separate formal letter to you email address if provided.</p> <p>Looking forward to hearing from you,</p> <p>Regards,</p> <p>Alireza Mohamadizadeh PhD Candidate Mechanical Engineering University of Waterloo</p>

Figure 2-5

Source: Zhang H, Senkara J. Resistance Welding: Fundamentals and Applications. Second Edi. CRC press; 2011. Figure 5.29

CCC Marketplace™

This is a License Agreement between Alireza Mohamadizadeh ("User") and Copyright Clearance Center, Inc. ("CCC") on behalf of the Rightsholder identified in the order details below. The license consists of the order details, the CCC Terms and Conditions below, and any Rightsholder Terms and Conditions which are included below.

All payments must be made in full to CCC in accordance with the CCC Terms and Conditions below.

Order Date	09-Jan-2022	Type of Use	Republish in a thesis/dissertation
Order License ID	1175767-1	Publisher	CRC Press
ISBN-13	9781439853719	Portion	Image/photo/illustration

LICENSED CONTENT

Publication Title	Resistance welding : fundamentals and applications	Country	United States of America
Author/Editor	Zhang, Hongyan, Senkara, Jacek.	Rightsholder	Taylor & Francis Group LLC - Books
Date	01/01/2012	Publication Type	Book
Language	English		

REQUEST DETAILS

Portion Type	Image/photo/illustration	Distribution	Canada
Number of images / photos / illustrations	5.29	Translation	Original language of publication
Format (select all that apply)	Electronic	Copies for the disabled?	No
Who will republish the content?	Academic institution	Minor editing privileges?	No
Duration of Use	Life of current edition	Incidental promotional use?	No
Lifetime Unit Quantity	Up to 499	Currency	CAD
Rights Requested	Main product		

NEW WORK DETAILS

Title	Characterization and microstructure-based modeling of spot weld failure in hot stamped steel	Institution name	University of Waterloo
Instructor name	Alireza Mohamadizadeh	Expected presentation date	2022-02-08

ADDITIONAL DETAILS

Order reference number	N/A	The requesting person / organization to appear on the license	Alireza Mohamadizadeh
-------------------------------	-----	--	-----------------------

Figure 2-7

Source: Pouranvari M, Sobhani S, Goodarzi F. Resistance spot welding of MS1200 martensitic advanced high strength steel: Microstructure-properties relationship. J Manuf Process 2018;31:867–74. <https://doi.org/10.1016/j.jmapro.2018.01.009>. Figure 4

ELSEVIER LICENSE
TERMS AND CONDITIONS

Jan 18, 2022

This Agreement between Dr. Alireza Mohamadizadeh ("You") and Elsevier ("Elsevier") consists of your license details and the terms and conditions provided by Elsevier and Copyright Clearance Center.

License Number	5232010683149
License date	Jan 18, 2022
Licensed Content Publisher	Elsevier
Licensed Content Publication	Journal of Manufacturing Processes
Licensed Content Title	Resistance spot welding of MS1200 martensitic advanced high strength steel: Microstructure-properties relationship
Licensed Content Author	M. Pouranvari,S. Sobhani,F. Goodarzi
Licensed Content Date	Jan 1, 2018
Licensed Content Volume	31
Licensed Content Issue	n/a
Licensed Content Pages	8
Start Page	867
End Page	874
Type of Use	reuse in a thesis/dissertation
Portion	figures/tables/illustrations
Number of figures/tables/illustrations	1
Format	electronic
Are you the author of this Elsevier article?	No
Will you be translating?	No
Title	Characterization and microstructure-based modeling of spot weld failure in hot stamped steel
Institution name	University of Waterloo
Expected presentation date	Jan 2022
Portions	Figure 4
Requestor Location	Dr. Alireza Mohamadizadeh 200 University Avenue N2L 3G1 Waterloo, ON N2L 3G1 Canada Attn: Dr. Alireza Mohamadizadeh
Publisher Tax ID	GB 494 6272 12
Total	0.00 CAD
Terms and Conditions	

Figure 2-9

Source: Tolton CJ. Characterization of Spot Weld Failure within Weld Groups under Predominantly Shear Loading by 2020. Figure 11

18 January 2022

Dear Cameron Tolton,

I would like permission to include the material listed below in my thesis titled "Characterization and microstructure-based modeling of spot weld failure in hot stamped steel".

- Figure 11 on page 13 of the master's thesis titled "Characterization of Spot Weld Failure within Weld Groups under Predominantly Shear Loading" by Cameron Jeffrey Tolton.

As part of this project, the source for this material is clearly credited. Material is impartial in nature and is used, copied, and stored for educational purposes only.

To indicate your agreement with the permission requested in this letter and the credit line detailed below, please sign and return this letter to me.

In signing, you are representing that you are the sole owner of the rights in the material granted by you in this letter, that you have the authority to grant permission, and that the University of Waterloo's intended use of the material will not infringe the rights of others.

I would greatly appreciate your consent to my request. If you require any additional information, please contact me.

Sincerely,


Alireza Mohamadizadeh

Mechanical and Mechatronics Engineering

University of Waterloo

APPROVED / PERMISSION GRANTED:

Name: Cameron Tolton

Signature 

Date: 2022-01-18

Company:

Address:

TITLE OR DESCRIPTION OF MATERIAL [Waterloo Organizational Unit to fill out]:

Creator / Author: Cameron Jeffrey Tolton

Copyright year, If known: 2020

[Figure/Table/Page Number, if applicable]: Figure 11

CAPTION AND CREDIT INFORMATION, [Waterloo Organizational Unit to fill out] e.g.:

Credit line(s) / copyright notice for the material

Figure 2-10

Source: Kianersi D, Mostafaei A, Amadeh AA. Resistance spot welding joints of AISI 316L austenitic stainless steel sheets: Phase transformations, mechanical properties and microstructure characterizations. Mater Des 2014;61:251–63. <https://doi.org/10.1016/j.matdes.2014.04.075>. Figure 4

ELSEVIER LICENSE TERMS AND CONDITIONS

Jan 18, 2022

This Agreement between Dr. Alireza Mohamadizadeh ("You") and Elsevier ("Elsevier") consists of your license details and the terms and conditions provided by Elsevier and Copyright Clearance Center.

License Number	5232020844907
License date	Jan 18, 2022
Licensed Content Publisher	Elsevier
Licensed Content Publication	Materials & Design
Licensed Content Title	Resistance spot welding joints of AISI 316L austenitic stainless steel sheets: Phase transformations, mechanical properties and microstructure characterizations
Licensed Content Author	Danial Kianersi, Amir Mostafaei, Ahmad Ali Amadeh
Licensed Content Date	Sep 1, 2014
Licensed Content Volume	61
Licensed Content Issue	n/a
Licensed Content Pages	13
Start Page	251
End Page	263
Type of Use	reuse in a thesis/dissertation
Portion	figures/tables/illustrations
Number of figures/tables/illustrations	1
Format	electronic
Are you the author of this Elsevier article?	No
Will you be translating?	No
Title	Characterization and microstructure-based modeling of spot weld failure in hot stamped steel
Institution name	University of Waterloo
Expected presentation date	Jan 2022
Portions	Figure 4
Requestor Location	Dr. Alireza Mohamadizadeh 200 University Avenue N2L 3G1 Waterloo, ON N2L 3G1 Canada Attn: Dr. Alireza Mohamadizadeh
Publisher Tax ID	GB 494 6272 12
Total	0.00 CAD
Terms and Conditions	

Figure 2-12

Source: Pouranvari M, Marashi SPH, Safanama DS. Failure mode transition in AHSS resistance spot welds . Part II : Experimental investigation and model validation. Mater Sci Eng A 2011;528:8344–52. <https://doi.org/10.1016/j.msea.2011.08.016>. Figure 5

ELSEVIER LICENSE TERMS AND CONDITIONS

Jan 18, 2022

This Agreement between Dr. Alireza Mohamadizadeh ("You") and Elsevier ("Elsevier") consists of your license details and the terms and conditions provided by Elsevier and Copyright Clearance Center.

License Number	5232060145111
License date	Jan 18, 2022
Licensed Content Publisher	Elsevier
Licensed Content Publication	Materials Science and Engineering: A
Licensed Content Title	Failure mode transition in AHSS resistance spot welds. Part II: Experimental investigation and model validation
Licensed Content Author	M. Pouranvari,S.P.H. Marashi,D.S. Safanama
Licensed Content Date	Nov 15, 2011
Licensed Content Volume	528
Licensed Content Issue	29-30
Licensed Content Pages	9
Start Page	8344
End Page	8352
Type of Use	reuse in a thesis/dissertation
Portion	figures/tables/illustrations
Number of figures/tables/illustrations	1
Format	electronic
Are you the author of this Elsevier article?	No
Will you be translating?	No
Title	Characterization and microstructure-based modeling of spot weld failure in hot stamped steel
Institution name	University of Waterloo
Expected presentation date	Jan 2022
Portions	Figure 5
Requestor Location	Dr. Alireza Mohamadizadeh 200 University Avenue N2L 3G1 Waterloo, ON N2L 3G1 Canada Attn: Dr. Alireza Mohamadizadeh
Publisher Tax ID	GB 494 6272 12
Total	0.00 CAD
Terms and Conditions	

Figure 2-14

Source: Dancette S, Fabrègue D, Massardier V, Merlin J, Dupuy T, Bouzekri M. Experimental and modeling investigation of the failure resistance of Advanced High Strength Steels spot welds. Eng Fract Mech 2011;78:2259–72. <https://doi.org/10.1016/j.engfracmech.2011.04.013>. Figure 2b and Figure 4a

ELSEVIER LICENSE
TERMS AND CONDITIONS

Jan 18, 2022

This Agreement between Dr. Alireza Mohamadizadeh ("You") and Elsevier ("Elsevier") consists of your license details and the terms and conditions provided by Elsevier and Copyright Clearance Center.

License Number	5232060272662
License date	Jan 18, 2022
Licensed Content Publisher	Elsevier
Licensed Content Publication	Engineering Fracture Mechanics
Licensed Content Title	Experimental and modeling investigation of the failure resistance of Advanced High Strength Steels spot welds
Licensed Content Author	S. Dancette, D. Fabrègue, V. Massardier, J. Merlin, T. Dupuy, M. Bouzekri
Licensed Content Date	Jul 1, 2011
Licensed Content Volume	78
Licensed Content Issue	10
Licensed Content Pages	14
Start Page	2259
End Page	2272
Type of Use	reuse in a thesis/dissertation
Portion	figures/tables/illustrations
Number of figures/tables/illustrations	2
Format	electronic
Are you the author of this Elsevier article?	No
Will you be translating?	No
Title	Characterization and microstructure-based modeling of spot weld failure in hot stamped steel
Institution name	University of Waterloo
Expected presentation date	Jan 2022
Portions	Figure 2b, Figure 4a
Requestor Location	Dr. Alireza Mohamadizadeh 200 University Avenue N2L 3G1 Waterloo, ON N2L 3G1 Canada Attn: Dr. Alireza Mohamadizadeh
Publisher Tax ID	GB 494 6272 12
Total	0.00 CAD
Terms and Conditions	

Figure 2-15

Source: Ordoñez Lara JH, Ambriz RR, García C, Plascencia G, Jaramillo D. Fatigue Life of Resistance Spot Welding on Dual-Phase Steels BT. Proc 17th Int Conf New Trends Fatigue Fract 2018:225–36. Figure 3 and Figure 4

SPRINGER NATURE LICENSE TERMS AND CONDITIONS

Jan 18, 2022

This Agreement between Dr. Alireza Mohamadizadeh ("You") and Springer Nature ("Springer Nature") consists of your license details and the terms and conditions provided by Springer Nature and Copyright Clearance Center.

License Number	5232060436392
License date	Jan 18, 2022
Licensed Content Publisher	Springer Nature
Licensed Content Publication	Springer eBook
Licensed Content Title	Fatigue Life of Resistance Spot Welding on Dual-Phase Steels
Licensed Content Author	J. H. Ordoñez Lara, R. R. Ambriz, C. García et al
Licensed Content Date	Jan 1, 2018
Type of Use	Thesis/Dissertation
Requestor type	academic/university or research institute
Format	electronic
Portion	figures/tables/illustrations
Number of figures/tables/illustrations	2
Will you be translating?	no
Circulation/distribution	1 - 29
Author of this Springer Nature content	no
Title	Characterization and microstructure-based modeling of spot weld failure in hot stamped steel
Institution name	University of Waterloo
Expected presentation date	Jan 2022
Portions	Figure 3, Figure 4
Requestor Location	Dr. Alireza Mohamadizadeh 200 University Avenue N2L 3G1 Waterloo, ON N2L 3G1 Canada Attn: Dr. Alireza Mohamadizadeh
Total	0.00 CAD
Terms and Conditions	

Figure 2-16

Source: Tong W, Tao H, Jiang X, Zhang N, Marya MP, Hector LG, et al. Deformation and fracture of miniature tensile bars with resistance-spot-weld microstructures. Metall Mater Trans A Phys Metall Mater Sci 2005;36:2651–69. <https://doi.org/10.1007/s11661-005-0263-4>. Figure 1 and Figure 2

SPRINGER NATURE LICENSE TERMS AND CONDITIONS

Jan 18, 2022

This Agreement between Dr. Alireza Mohamadizadeh ("You") and Springer Nature ("Springer Nature") consists of your license details and the terms and conditions provided by Springer Nature and Copyright Clearance Center.

License Number	5232060603551
License date	Jan 18, 2022
Licensed Content Publisher	Springer Nature
Licensed Content Publication	Metallurgical and Materials Transactions A
Licensed Content Title	Deformation and fracture of miniature tensile bars with resistance-spot-weld microstructures
Licensed Content Author	Wei Tong et al
Licensed Content Date	Jan 1, 2005
Type of Use	Thesis/Dissertation
Requestor type	academic/university or research institute
Format	electronic
Portion	figures/tables/illustrations
Number of figures/tables/illustrations	2
Will you be translating?	no
Circulation/distribution	1 - 29
Author of this Springer Nature content	no
Title	Characterization and microstructure-based modeling of spot weld failure in hot stamped steel
Institution name	University of Waterloo
Expected presentation date	Jan 2022
Portions	Figure 1, Figure 2
Requestor Location	Dr. Alireza Mohamadizadeh 200 University Avenue N2L 3G1 Waterloo, ON N2L 3G1 Canada Attn: Dr. Alireza Mohamadizadeh
Total	0.00 CAD
Terms and Conditions	

Figure 2-19

Source: Enomoto Y. Steam turbine retrofitting for the life extension of power plants. Elsevier Ltd; 2017. <https://doi.org/10.1016/B978-0-08-100314-5.00017-8>. Figure 17.5

ELSEVIER LICENSE TERMS AND CONDITIONS

Jan 18, 2022

This Agreement between Dr. Alireza Mohamadizadeh ("You") and Elsevier ("Elsevier") consists of your license details and the terms and conditions provided by Elsevier and Copyright Clearance Center.

License Number	5232081213024
License date	Jan 18, 2022
Licensed Content Publisher	Elsevier
Licensed Content Publication	Elsevier Books
Licensed Content Title	Advances in Steam Turbines for Modern Power Plants
Licensed Content Author	Y. Enomoto
Licensed Content Date	Jan 1, 2017
Licensed Content Pages	40
Start Page	397
End Page	436
Type of Use	reuse in a thesis/dissertation
Portion	figures/tables/illustrations
Number of figures/tables/illustrations	2
Format	electronic
Are you the author of this Elsevier chapter?	No
Will you be translating?	No
Title	Characterization and microstructure-based modeling of spot weld failure in hot stamped steel
Institution name	University of Waterloo
Expected presentation date	Jan 2022
Portions	Figure 17.5
Requestor Location	Dr. Alireza Mohamadizadeh 200 University Avenue N2L 3G1 Waterloo, ON N2L 3G1 Canada Attn: Dr. Alireza Mohamadizadeh
Publisher Tax ID	GB 494 6272 12
Total	0.00 CAD
Terms and Conditions	

Bibliography

- [1] Kuziak R, Kawalla R, Waengler S. Advanced high strength steels for automotive industry. *Arch Civ Mech Eng* 2008;8:103–17. [https://doi.org/10.1016/S1644-9665\(12\)60197-6](https://doi.org/10.1016/S1644-9665(12)60197-6).
- [2] Taylor T, Clough A. Critical review of automotive hot-stamped sheet steel from an industrial perspective. *Mater Sci Technol (United Kingdom)* 2018;34:809–61. <https://doi.org/10.1080/02670836.2018.1425239>.
- [3] Fan DW, Kim HS, De Cooman BC. A Review of the Physical Metallurgy related to the Hot Press Forming of Advanced High Strength Steel. *Steel Res Int* 2010;80:241–8. <https://doi.org/10.2374/SRI08SP131>.
- [4] ArcelorMittal. Steels for hot stamping. *Procedia Eng* 2008. <https://doi.org/10.1016/j.proeng.2011.04.368>.
- [5] George R, Bardelcik A, Worswick MJ. Hot forming of boron steels using heated and cooled tooling for tailored properties. *J Mater Process Technol* 2012;212:2386–99. <https://doi.org/10.1016/j.jmatprotec.2012.06.028>.
- [6] Peister C, George R, Omer K, Worswick MJ, Malcolm S, Dykeman J, et al. Forming of an axially tailored automotive channel section through hot stamping of tailor-welded blanks. *J Phys Conf Ser* 2017;896:012052. <https://doi.org/10.1088/1742-6596/896/1/012052>.
- [7] Williams NT, Parker JD. Review of resistance spot welding of steel sheets Part 1 Modelling and control of weld nugget formation. *Int Mater Rev* 2004;49:45–75. <https://doi.org/10.1179/095066004225010523>.
- [8] Jong Y-S, Lee Y-K, Kim D-C, Kang M-J, Hwang I-S, Lee W-B. Microstructural Evolution and Mechanical Properties of Resistance Spot Welded Ultra High Strength Steel Containing Boron. *Mater Trans* 2011;52:1330–3. <https://doi.org/10.2320/matertrans.M2011005>.
- [9] Zhang H, Senkara J. *Resistance Welding: Fundamentals and Applications*. Second Edi. CRC press; 2011.
- [10] Wung P. A forced-based failure criterion for spot weld design. *Exp Mech* 2001;41:107–13. <https://doi.org/10.1007/BF02323112>.
- [11] Lin SH, Pan J, Tyan T, Prasad P. A general failure criterion for spot welds under combined

- loading conditions. *Int J Solids Struct* 2003;40:5539–64. [https://doi.org/10.1016/S0020-7683\(03\)00341-X](https://doi.org/10.1016/S0020-7683(03)00341-X).
- [12] A.B NJ. Manufacturing a hardened steel article, 1974.
- [13] Aspacher J. Forming hardening concepts. 1st Int Conf Hot Sheet Met Form High Perform Steel, Kassel, Ger 2008:77–81.
- [14] Philipp H, Joël W, Hein P, Wilsius J, Philipp H, Joël W, et al. Status and innovation trends in hot stamping of USIBOR 1500 P. *Steel Res Int* 2008;2:85–91. <https://doi.org/10.2374/SRI08SP010-79-2008-85-91>.
- [15] Gharbi MM, Palm C. Trends and challenges in hot stamping technology. *AIP Conf Proc* 2017;1896. <https://doi.org/10.1063/1.5008063>.
- [16] ArcelorMittal. Steels for hot stamping - Usibor® and Ductibor®. Eng Proceeding 2008.
- [17] Karbasian H, Tekkaya AE. A review on hot stamping. *J Mater Process Technol* 2010;210:2103–18. <https://doi.org/10.1016/j.jmatprotec.2010.07.019>.
- [18] Naderi M. Hot Stamping of Ultra High Strength Steels 2007:190. <https://doi.org/28187>.
- [19] Hoffmann H, So H, Steinbeiss H. Design of hot stamping tools with cooling system. *CIRP Ann - Manuf Technol* 2007;56:269–72. <https://doi.org/10.1016/j.cirp.2007.05.062>.
- [20] Merklein M, Wieland M, Lechner M, Bruschi S, Ghiotti A. Hot stamping of boron steel sheets with tailored properties: A review. *J Mater Process Technol* 2016;228:11–24. <https://doi.org/10.1016/j.jmatprotec.2015.09.023>.
- [21] Vural M, Akkuş A, Eryürek B. Effect of welding nugget diameter on the fatigue strength of the resistance spot welded joints of different steel sheets. *J Mater Process Technol* 2006;176:127–32. <https://doi.org/10.1016/j.jmatprotec.2006.02.026>.
- [22] Al-Mukhtar A. Review of Resistance Spot Welding Sheets: Processes and Failure Mode. *Adv Eng Forum* 2016;17:31–57. <https://doi.org/10.4028/www.scientific.net/AEF.17.31>.
- [23] Committee on Automotive Welding. AWS D8.1M, Specification for Automotive Weld Quality - Resistance Spot Welding of Steel. American Welding Society; 2013.
- [24] Bertin L. Tensile Strength of Automotive Aluminum Joints Using Resistance Spot Welding, Self-Piercing Riveting and Adhesive Hybrid Joining. 2014.

- [25] Pouranvari M, Ranjbarnoodeh E. Dependence of the fracture mode on the welding variables in the resistance spot welding of ferrite-martensite DP980 advanced high-strength steel. *Mater Technol* 2012;46:665–71. <https://doi.org/10.1179/1879139512Y.0000000034>.
- [26] Weldcor. Temperature Distribution During a Resistance Spot Welding n.d. <https://www.weldcor.ca/public/ckfinder/userfiles/files/FIGURE R-8.png> (accessed September 18, 2021).
- [27] Tolf E, Hedegård J. Influence of reduced cooling time on the properties of resistance spot welds. *Weld World* 2008;52:43–53. <https://doi.org/10.1007/BF03266631>.
- [28] Andersson O. Process planning of resistance spot welding. 2013. <https://doi.org/10.1158/0008-5472.CAN-06-0363>.
- [29] Zhang H. Expulsion and its influence on weld quality. *Weld J* 1999;78:373s-380s.
- [30] Pouranvari M, Abedi A, Marashi P, Goodarzi M. Effect of expulsion on peak load and energy absorption of low carbon steel resistance spot welds. *Sci Technol Weld Join* 2008;13:39–43. <https://doi.org/10.1179/174329307X249342>.
- [31] Nikoosohbat F, Kheirandish S, Goodarzi M, Pouranvari M, Marashi SPH. Microstructure and failure behaviour of resistance spot welded DP980 dual phase steel. *Mater Sci Technol* 2010;26:738–44. <https://doi.org/10.1179/174328409X414995>.
- [32] Kaiser JG, Dunn GJ, Eagar TW. Effect of electrical resistance on nugget formation during spot welding. *Weld J* 1982;62:167.
- [33] Kearns WH. *Welding Processes-Resistance and Solid-State Welding and Other Joining Processes*. vol. 3. Amer Welding Society; 1980.
- [34] Den Uijl NJ, Smith S. Resistance spot welding of advanced high strength steels for the automotive industry. 4th Int Semin Adv Resist Welding, Wels, Austria 2006:30–60.
- [35] Den Uijl NJ. *Resistance Spot Welding of Advanced High Strength Steels*. University of Delft, 2015. <https://doi.org/10.4233/uuid:ef6aa135-0ef3-42d5-b2a7-d270f36529ad>.
- [36] Ely KJ, Zhou Y. Microresistance spot welding of Kovar, steel, and nickel. *Sci Technol Weld Join* 2001;6:63–72. <https://doi.org/10.1179/136217101101538541>.
- [37] Ighodaro O. Effects of Metallic Coatings on Resistance Spot Weldability of Hot Stamping

- Steel. University of Waterloo, 2017.
- [38] Ramazani A, Mukherjee K, Abdurakhmanov A, Abbasi M, Pahl U. Characterization of Microstructure and Mechanical Properties of Resistance Spot Welded DP600 Steel. *Metals (Basel)* 2015;5:1704–16. <https://doi.org/10.3390/met5031704>.
- [39] Abe F, Kern TU, Viswanathan R. *Creep-Resistant Steels*. Elsevier; 2008. <https://doi.org/10.1533/9781845694012>.
- [40] Hou JS. *Resistance Spot Welding and In-Process Heat Treatment of Hot Stamped Boron Steel*. University of Waterloo, 2016.
- [41] Pouranvari M, Sobhani S, Goodarzi F. Resistance spot welding of MS1200 martensitic advanced high strength steel: Microstructure-properties relationship. *J Manuf Process* 2018;31:867–74. <https://doi.org/10.1016/j.jmapro.2018.01.009>.
- [42] Raabe D. Recovery and Recrystallization: Phenomena, Physics, Models, Simulation. In: Laughlin DE, Hono KBT-PM (Fifth E, editors. *Phys. Metall. Fifth*, Oxford: Elsevier; 2014, p. 2291–397. <https://doi.org/https://doi.org/10.1016/B978-0-444-53770-6.00023-X>.
- [43] Speer J, Matlock DK, De Cooman BC, Schroth JG. Carbon partitioning into austenite after martensite transformation. *Acta Mater* 2003;51:2611–22. [https://doi.org/10.1016/S1359-6454\(03\)00059-4](https://doi.org/10.1016/S1359-6454(03)00059-4).
- [44] Mola J, De Cooman BC. Quenching and Partitioning (Q&P) Processing of Martensitic Stainless Steels. *Metall Mater Trans A* 2013;44:946–67. <https://doi.org/10.1007/s11661-012-1420-1>.
- [45] Saha DC, Biro E, Gerlich AP, Zhou Y. Effects of tempering mode on the structural changes of martensite. *Mater Sci Eng A* 2016;673:467–75. <https://doi.org/https://doi.org/10.1016/j.msea.2016.07.092>.
- [46] Rathbun RW, Matlock DK, Speer JG. Fatigue behavior of spot welded high-strength sheet steels. *Weld J* 2003;82:207–18.
- [47] Pouranvari M, Marashi SPH. Critical review of automotive steels spot welding: process, structure and properties. *Sci Technol Weld Join* 2013;18:361–403. <https://doi.org/10.1179/1362171813Y.0000000120>.
- [48] D.J.Radakovic MT. An Evolution of the Cross-Tension Test of Resistance Spot Welds in

- High-Strength Dual-Phase Steels. *Weld J* 2012;91:8–15.
- [49] Tolton CJ. Characterization of Spot Weld Failure within Weld Groups under Predominantly Shear Loading by 2020.
- [50] Seeger F, Michel G, Blanquet M. Investigation of spot weld behavior using detailed modeling technique. *7 LS-DYNA Anwenderforum* 2008:29–38.
- [51] Verlag Stahleisen GmbH. Testing and Documentation Guideline for the Joinability of thin sheet of steel - Part 2: Resistance Spot Welding (SEP 1220-2) 2011:37.
- [52] Mohamadizadeh A, Biro E, Worswick M. Novel Double-Half Spot Weld Testing Technique For Damage Progress And Failure Analysis Using Digital Image Correlation Techniques. *Exp Mech* 2021. <https://doi.org/10.1007/s11340-021-00743-4>.
- [53] Zhang F, Xu H, Fang X. Failure behavior and crash modelling of resistance rivet spot welding (RRSW) for joining Al and steel in vehicle structure. *Int J Crashworthiness* 2020;0:1–18. <https://doi.org/10.1080/13588265.2020.1786269>.
- [54] Heidrich D, Zhang F, Fang X. Fatigue Strength of Rivet Resistance Spot Welding Technique in Comparison with Self-Piercing Riveting for Multi-material Body-in-White Structure. *J Mater Eng Perform* 2021;30:3806–21. <https://doi.org/10.1007/s11665-021-05684-6>.
- [55] Kianersi D, Mostafaei A, Amadeh AA. Resistance spot welding joints of AISI 316L austenitic stainless steel sheets: Phase transformations, mechanical properties and microstructure characterizations. *Mater Des* 2014;61:251–63. <https://doi.org/10.1016/j.matdes.2014.04.075>.
- [56] Sun X, Stephens E V., Khaleel MA. Effects of fusion zone size and failure mode on peak load and energy absorption of advanced high strength steel spot welds under lap shear loading conditions. *Eng Fail Anal* 2008;15:356–67. <https://doi.org/10.1016/j.engfailanal.2007.01.018>.
- [57] Radakovic DJ, Tumuluru M. Predicting Resistance Spot Weld Failure Modes in Shear Tension Tests of Advanced High-Strength Automotive Steels. *Weld J* 2008;87:96S-105S.
- [58] Tamizi M, Pouranvari M, Movahedi M. Welding metallurgy of martensitic advanced high strength steels during resistance spot welding. *Sci Technol Weld Join* 2017;22:327–35. <https://doi.org/10.1080/13621718.2016.1240979>.
- [59] Pouranvari M, Marashi SPH. Failure mode transition in AHSS resistance spot welds. Part I. Controlling factors. *Mater Sci Eng A* 2011;528:8337–43.

<https://doi.org/10.1016/j.msea.2011.08.017>.

- [60] Pouranvari M, Marashi SPH, Safanama DS. Failure mode transition in AHSS resistance spot welds . Part II : Experimental investigation and model validation. *Mater Sci Eng A* 2011;528:8344–52. <https://doi.org/10.1016/j.msea.2011.08.016>.
- [61] Pouranvari M, Asgari HR, Mosavizadch SM, Marashi PH, Goodarzi M. Effect of weld nugget size on overload failure mode of resistance spot welds. *Sci Technol Weld Join* 2007;12:217–25. <https://doi.org/10.1179/174329307X164409>.
- [62] Song JH, Ha JW, Huh H, Lim JH, Park SH. Dynamic failure of a spot weld in a lap-shear tests under combined loading conditions. *Int J Mod Phys B* 2008;22:5527–32.
- [63] Pouranvari M, Marashi P. Resistance Spot Welding of Unequal Thickness Low Carbon Steel Sheets. *Adv Mater Res* 2009;83–86:1205–11. <https://doi.org/10.4028/www.scientific.net/AMR.83-86.1205>.
- [64] Dancette S, Fabrègue D, Massardier V, Merlin J, Dupuy T, Bouzekri M. Experimental and modeling investigation of the failure resistance of Advanced High Strength Steels spot welds. *Eng Fract Mech* 2011;78:2259–72. <https://doi.org/10.1016/j.engfracmech.2011.04.013>.
- [65] Ordoñez Lara JH, Ambriz RR, García C, Plascencia G, Jaramillo D. Fatigue Life of Resistance Spot Welding on Dual-Phase Steels BT. *Proc 17th Int Conf New Trends Fatigue Fract* 2018:225–36.
- [66] Tamizi M, Pouranvari M, Movahedi M. The Role of HAZ Softening on Cross-Tension Mechanical Performance of Martensitic Advanced High Strength Steel Resistance Spot Welds. *Metall Mater Trans A* 2021. <https://doi.org/10.1007/s11661-020-06104-5>.
- [67] Pouranvari M, Marashi SPHH. On failure mode of resistance spot welded DP980 advanced high strength steel. *Can Metall Q* 2012;51:447–55. <https://doi.org/10.1179/1879139512Y.0000000034>.
- [68] Zhao Y, Zhang Y, Lai X. Analysis of fracture modes of resistance spot welded hot-stamped boron steel. *Metals (Basel)* 2018;8:1–15. <https://doi.org/10.3390/met8100764>.
- [69] Sherepenko O, Jüttner S. Transient softening at the fusion boundary in resistance spot welded ultra-high strengths steel 22MnB5 and its impact on fracture processes. *Weld World* 2019;63:151–9. <https://doi.org/10.1007/s40194-018-0633-3>.

- [70] Gould JE, Workman D. Fracture morphologies of resistance spot welds exhibiting hold time sensitivity behavior. Proc Sheet Met Weld Conf VIII 1998.
- [71] Khan MI, Kuntz ML, Zhou Y. Effects of weld microstructure on static and impact performance of resistance spot welded joints in advanced high strength steels. Sci Technol Weld Join 2008;13:294–304. <https://doi.org/10.1179/174329308X271733>.
- [72] Luo Y, Wu SC, Hu YN, Fu YN. Cracking evolution behaviors of lightweight materials based on in situ synchrotron X-ray tomography: A review. Front Mech Eng 2018;13:461–81. <https://doi.org/10.1007/s11465-018-0481-2>.
- [73] Wittevrongel L, Lava P, Lomov S V., Debruyne D. A Self Adaptive Global Digital Image Correlation Algorithm. Exp Mech 2015;55:361–78. <https://doi.org/10.1007/s11340-014-9946-3>.
- [74] Tao H, Tong W, Hector LG, Zavattieri PD. Uniaxial tensile and simple shear behavior of resistance spot-welded dual-phase steel joints. J Mater Eng Perform 2008;17:517–34. <https://doi.org/10.1007/s11665-007-9170-8>.
- [75] Tong W, Tao H, Zhang N, Jiang X, Marya MP, Hector LG, et al. Deformation and fracture of miniature tensile bars with resistance-spot-weld microstructures. Metall Mater Trans A 2005;36:2651–69. <https://doi.org/10.1007/s11661-005-0263-4>.
- [76] Eller TK, Greve L, Andres M, Medricky M, Geijselaers HJM, Meinders VT, et al. Plasticity and fracture modeling of the heat-affected zone in resistance spot welded tailor hardened boron steel. J Mater Process Technol 2016;234:309–22. <https://doi.org/10.1016/j.jmatprotec.2016.03.026>.
- [77] Bai Y, Wierzbicki T. Application of extended Mohr-Coulomb criterion to ductile fracture. Int J Fract 2010;161:1–20. <https://doi.org/10.1007/s10704-009-9422-8>.
- [78] Ghassemi-Armaki H, Biro E, Sadagopan S. Advanced Characterization of HAZ Softening of AHSS for Crash Modeling. ISIJ Int 2017;57:1451–60. <https://doi.org/10.2355/isijinternational.ISIJINT-2016-649>.
- [79] O'Keefe C. Investigation of Resistance Spot Weld Failure in Tailored Hot Stamped Assemblies. University of Waterloo, 2018.
- [80] Dancette S, Massardier-Jourdan V, Fabrègue D, Merlin J, Dupuy T, Bouzekri M, et al. HAZ

- Microstructures and Local Mechanical Properties of High Strength Steels Resistance Spot Welds. *ISIJ Int* 2011;51:99–107. <https://doi.org/10.2355/isijinternational.51.99>.
- [81] Raath ND, Norman D, McGregor I, Hepple S, Dashwood R, Hughes DJ. Characterization of Loading Responses and Failure Loci of a Boron Steel Spot Weld. *Metall Mater Trans A Phys Metall Mater Sci* 2018;49:1536–51. <https://doi.org/10.1007/s11661-018-4502-x>.
- [82] Paveebunvipak K, Uthaisangsuk V. Microstructure based modeling of deformation and failure of spot-welded advanced high strength steels sheets. *Mater Des* 2018;160:731–51. <https://doi.org/10.1016/j.matdes.2018.09.052>.
- [83] Ma Y, Yu Y, Geng P, Ihara R, Maeda K, Suzuki R, et al. Fracture modeling of resistance spot welded ultra-high-strength steel considering the effect of liquid metal embrittlement crack. *Mater Des* 2021;210:110075. <https://doi.org/10.1016/j.matdes.2021.110075>.
- [84] Chung K, Noh W, Yang X, Han HN, Lee M-GG, Yang X, et al. Practical failure analysis of resistance spot welded advanced high-strength steel sheets. *Int J Plast* 2016;94:122–47. <https://doi.org/10.1016/j.ijplas.2016.10.010>.
- [85] Patil S, Lankarani H. Characterisation and modelling the strength of EHSS steel grade spot weld for automotive joints and its application for frontal impact load-case. *Int J Crashworthiness* 2017;0:1–11. <https://doi.org/10.1080/13588265.2017.1389628>.
- [86] Hamid M SP. Simulation Study of Spot Weld Material Configurations for Crash Analysis. *J Appl Mech Eng* 2015;04. <https://doi.org/10.4172/2168-9873.1000149>.
- [87] Skrzypek J, Ganczarski A. Modeling of Material Damage and Failure of Structures: Theory and Applications. Berlin, Heidelberg: Springer Berlin Heidelberg; 1999. <https://doi.org/10.1007/s00132-007-1106-3>.
- [88] Marya M, Gayden XQ. Development of requirements for resistance spot welding dual-phase (DP600) steels part 1—the causes of interfacial fracture. *Weld J* 2005;84:172–82.
- [89] Ma C, Chen DL, Bhole SD, Boudreau G, Lee A, Biro E. Microstructure and fracture characteristics of spot-welded DP600 steel. *Mater Sci Eng A* 2008;485:334–46. <https://doi.org/10.1016/j.msea.2007.08.010>.
- [90] Enomoto Y. Steam turbine retrofitting for the life extension of power plants. Elsevier Ltd; 2017. <https://doi.org/10.1016/B978-0-08-100314-5.00017-8>.

- [91] Paul SK, Kumar A. Micromechanics based modeling to predict flow behavior and plastic strain localization of dual phase steels. *Comput Mater Sci* 2012;63:66–74. <https://doi.org/10.1016/j.commatsci.2012.05.061>.
- [92] Srithananan P, Kaewtatip P, Uthaisangsuk V. Micromechanics-based modeling of stress-strain and fracture behavior of heat-treated boron steels for hot stamping process. *Mater Sci Eng A* 2016;667:61–76. <https://doi.org/10.1016/j.msea.2016.04.065>.
- [93] Golling S, Östlund R, Oldenburg M. Characterization of ductile fracture properties of quench-hardenable boron steel: Influence of microstructure and processing conditions. *Mater Sci Eng A* 2016;658:472–83. <https://doi.org/10.1016/j.msea.2016.01.091>.
- [94] Besson J. Continuum models of ductile fracture: A review. vol. 19. 2010. <https://doi.org/10.1177/1056789509103482>.
- [95] Östlund R. Microstructure Based Modelling of Ductile Fracture in Quench-Hardenable Boron Steel. Luleå University of Technology, 2015.
- [96] Lemaitre J. A Continuous Damage Mechanics Model for Ductile Fracture. *J Eng Mater Technol* 1985;107:83. <https://doi.org/10.1115/1.3225775>.
- [97] Tie-jun W, Tib-jun W. Unified Cdm Model and Local Criterion 1992;42:177–83.
- [98] Bonora N. A nonlinear CDM model for ductile failure. *Eng Fract Mech* 1997;58:11–28. [https://doi.org/10.1016/S0013-7944\(97\)00074-X](https://doi.org/10.1016/S0013-7944(97)00074-X).
- [99] Dhar S, Dixit PM, Sethuraman R. A continuum damage mechanics model for ductile fracture. *Int J Press Vessel Pip* 2000;77:335–44. [https://doi.org/10.1016/S0308-0161\(00\)00019-3](https://doi.org/10.1016/S0308-0161(00)00019-3).
- [100] Baaser H, Gross D. Remarks on the Use of Continuum Damage Models and on the Limitations of their Applicability in Ductile Fracture Mechanics. Berlin, Heidelberg: Springer Berlin Heidelberg; 2003. https://doi.org/10.1007/978-3-540-36564-8_14.
- [101] Wierzbicki T, Bao Y, Lee YW, Bai Y. Calibration and evaluation of seven fracture models. *Int J Mech Sci* 2005;47:719–43. <https://doi.org/10.1016/j.ijmecsci.2005.03.003>.
- [102] Björklund O. Ductile Failure in High Strength Steel Sheets. Linköping University Electronic Press, 2014.
- [103] Lee Y. Fracture Prediction in Metal Sheets. 2005.

- [104] Zadpoor AA, Sinke J, Benedictus R. Formability prediction of high strength aluminum sheets. *Int J Plast* 2009;25:2269–97. <https://doi.org/10.1016/j.ijplas.2009.02.005>.
- [105] Cockcroft MG, Latham DJ. Ductility and the workability of metals. *J Inst Met* 1968;96:33–9. <https://doi.org/citeulike-article-id:4789874>.
- [106] Clift SE, Hartley P, Sturgess CEN, Rowe GW. Fracture prediction in plastic deformation processes. *Int J Mech Sci* 1990;32:1–17. [https://doi.org/10.1016/0020-7403\(90\)90148-C](https://doi.org/10.1016/0020-7403(90)90148-C).
- [107] Johnson GR, Cook WH. Fracture characteristics of three metals subjected to various strains, strain rates, temperatures and pressures. *Eng Fract Mech* 1985;21:31–48. [https://doi.org/10.1016/0013-7944\(85\)90052-9](https://doi.org/10.1016/0013-7944(85)90052-9).
- [108] Xue L. Damage accumulation and fracture initiation in uncracked ductile solids subject to triaxial loading. *Int J Solids Struct* 2007;44:5163–81. <https://doi.org/10.1016/j.ijsolstr.2006.12.026>.
- [109] Neukamm F, Feucht M, Haufe A. Considering damage history in crashworthiness simulations. 7th Eur LS-DYNA Conf 2009.
- [110] ten Kortenaar L, Omer K, Butcher C, Bardelcik A, Worswick M, Detwiler D, et al. Implementation of a Failure Criterion for Axial Crush of Fully Hardened Boron Steel. *Hot Sheet Met Form High-Performance Steel Chs2 (5Th Int Conf 2015):157–65*.
- [111] Samadian P, Butcher C, Worswick MJ. The Determination of the Fracture Behavior of the Different Microstructures of Ductibor® 500-AS Steel. *7th Int Conf Hot Sheet Met Form High Perform Steel 2019*.
- [112] Omer K, ten Kortenaar L, Butcher C, Worswick M, Malcolm S, Detwiler D. Testing of a hot stamped axial crush member with tailored properties – Experiments and models. *Int J Impact Eng* 2017;103:12–28. <https://doi.org/10.1016/j.ijimpeng.2017.01.003>.
- [113] Peister C, O’Keeffe C, Imbert J, Butcher C, Worswick M, Malcolm S, et al. Dynamic and Quasi-Static Testing and Modeling of Hot Stamped Tailor-Welded Axial Crush Rails. *18th Int. Conf. Exp. Mech. (ICEM 2018)*, vol. 2, 2018, p. 526. <https://doi.org/10.3390/icem18-05401>.
- [114] Tresca H. Memoir on the flow of solid bodies under strong pressure. *Comptes-Rendus l’académie Des Sci* 1864;59:754–8.

- [115] Coulomb CA. An attempt to apply the rules of maxima and minima to several problems of stability related to architecture. *Mémoires l'Académie R Des Sci* 1776;7:343–82.
- [116] Mohr O. Welche Umstände bedingen die Elastizitätsgrenze und den Bruch eines Materials? *Zeit Des Ver Deut Ing* 1900;44:1524–1530. <https://doi.org/10.1007/s00440-016-0719-z>.
- [117] Nielsen KL, Tvergaard V. Ductile shear failure or plug failure of spot welds modelled by modified Gurson model. *Eng Fract Mech* 2010;77:1031–47. <https://doi.org/10.1016/j.engfracmech.2010.02.031>.
- [118] Nahshon K, Hutchinson JW. Modification of the Gurson Model for shear failure. *Eur J Mech A/Solids* 2008;27:1–17. <https://doi.org/10.1016/j.euromechsol.2007.08.002>.
- [119] Yang X, Xia Y, Zhou Q. A simplified FE model for pull-out failure of spot welds. *Eng Fract Mech* 2010;77:1224–39. <https://doi.org/10.1016/j.engfracmech.2010.02.029>.
- [120] Chao YJ. Ultimate Strength and Failure Mechanism of Resistance Spot Weld Subjected to Tensile, Shear, or Combined Tensile/Shear Loads. *J Eng Mater Technol* 2003;125:125. <https://doi.org/10.1115/1.1555648>.
- [121] Meyers MA, Chawla KK. Mechanical Behavior of Materials. *Mater Today* 2009;12:44. [https://doi.org/https://doi.org/10.1016/S1369-7021\(09\)70086-0](https://doi.org/https://doi.org/10.1016/S1369-7021(09)70086-0).
- [122] Wung P, Walsh T, Ourchane A, Stewart W, Jie M. Failure of spot welds under in-plane static loading. *Exp Mech* 2001;41:100–6. <https://doi.org/10.1007/BF02323111>.
- [123] Rokhlin SI, Adler L. Ultrasonic method for shear strength prediction of spot welds. *J Appl Phys* 1984;56:726–31. <https://doi.org/10.1063/1.334000>.
- [124] Zhang SC. Stress Intensities at Spot Welds. *Int J Fract* 1997;88:167–85. <https://doi.org/10.1023/A:1007461430066>.
- [125] Lee Y, Wehner T, Lu M-W, Morrisett T, Pakalnins E. Ultimate Strength of Resistance Spot Welds Subjected to Combined Tension and Shear. *J Test Eval* 1998;26:213. <https://doi.org/10.1520/JTE11994J>.
- [126] Lin S-H, Pan J, Wu S, Tyan T, Wung P. Spot Weld Failure Loads under Combined Mode Loading Conditions. Society, 2001. <https://doi.org/10.4271/2001-01-0428>.
- [127] Lin SH, Pan J, Wu SR, Tyan T, Wung P. Failure loads of spot welds under combined opening

- and shear static loading conditions. *Int J Solids Struct* 2002;39:19–39.
[https://doi.org/10.1016/S0020-7683\(01\)00187-1](https://doi.org/10.1016/S0020-7683(01)00187-1).
- [128] Xiang Y, Wang Q, Fan Z, Fang H. Optimal crashworthiness design of a spot-welded thin-walled hat section. *Finite Elem Anal Des* 2006;42:846–55.
<https://doi.org/10.1016/j.finel.2006.01.001>.
- [129] Malcolm S, Nutwell E. Spotweld Failure Prediction using Solid Element Assemblies. 6th Eur LS-Dyna Users Conf 2007:47–56.
<https://pdfs.semanticscholar.org/ce0e/f1f48a05f9582fb194687e46f974a6bdee33.pdf> (accessed July 10, 2018).
- [130] Schneider F, Jones N. Influence of spot-weld failure on crushing of thin-walled structural sections. *Int J Mech Sci* 2003;45:2061–81. <https://doi.org/10.1016/j.ijmecsci.2003.11.004>.
- [131] Tarigopula V, Langseth M, Hopperstad OS, Clausen AH. Axial crushing of thin-walled high-strength steel sections. *Int J Impact Eng* 2006;32:847–82.
<https://doi.org/10.1016/j.ijimpeng.2005.07.010>.
- [132] Bier M, Liebold C, Haufe A, Klamser H. Evaluation of a Rate-Dependent , Elasto-Plastic Cohesive Zone Mixed-Mode Constitutive Model for Spot Weld Modeling. *LS-DYNA Forum* 2010:25–38.
- [133] Seeger F, Feucht M, Frank T, Keding B, Haufe A. An Investigation on Spot Weld Modelling for Crash Simulation with LS-DYNA. 4th LS-DYNA User Forum, Bamb 2005:1–12.
ftp://ftp.lstc.com/outgoing/jday/spotwelds/application_of_spotwelds.pdf (accessed July 7, 2017).
- [134] Madasamy C, Tyan T, Faruque O. Finite element modeling of spot weld connections in crash applications. *SAE Tech Pap* 2004. <https://doi.org/10.4271/2004-01-0691>.
- [135] Pandya KS, Grolleau V, Roth CC, Mohr D. Fracture response of resistance spot welded dual phase steel sheets: Experiments and modeling. *Int J Mech Sci* 2020;187:105869.
<https://doi.org/10.1016/j.ijmecsci.2020.105869>.
- [136] Wang J, Xia Y, Zhou Q, Zhang J. Simulation of Spot Weld Pullout by Modeling Failure Around Nugget. 2006 SAE World Congr 2006. <https://doi.org/10.4271/2006-01-0532>.
- [137] Committee on Automotive Welding. AWS D8.9M Recommended Practices For Test Methods

For Evaluating The Resistance Spot Welding Behaviour Of Automotive Sheet Steel Materials. American Welding Society; 2012.

- [138] Yuan X, Zhang Q. Microstructure Evolution of Hot-Dip Al-10%Si Coating During the Austenitization of 22MnB5 Hot Stamping Steel. *Jinshu Xuebao/Acta Metall Sin* 2017;53:1495–503. <https://doi.org/10.11900/0412.1961.2017.00077>.
- [139] Gui Z xiang, Liang W kang, Liu Y, Zhang Y sheng. Thermo-mechanical behavior of the Al-Si alloy coated hot stamping boron steel. *Mater Des* 2014;60:26–33. <https://doi.org/10.1016/j.matdes.2014.03.011>.
- [140] Samadian P, Butcher C, Worswick MJ. Microstructures and Flow Behavior of Ductibor® 500-AS Steel for a Range of As-Quenched Conditions. *J Mater Eng Perform* 2020;29:7153–69. <https://doi.org/10.1007/s11665-020-05205-x>.
- [141] Omer K, George R, Bardelcik A, Worswick M, Malcolm S, Detwiler D. Development of a hot stamped channel section with axially tailored properties – experiments and models. *Int J Mater Form* 2018;11:149–64. <https://doi.org/10.1007/s12289-017-1338-7>.
- [142] Committee on Automotive Welding. AWS J1.3M Specification for Materials Used in Resistance Welding Electrodes and Tooling. 2020.
- [143] ArcelorMittal. Private Communication 2017.
- [144] Eller TK. Modeling of tailor hardened boron steel. 2016.
- [145] Eller TK, Greve L, Andres M, Medricky M, Meinders VT, Van Den Boogaard AH. Determination of strain hardening parameters of tailor hardened boron steel up to high strains using inverse FEM optimization and strain field matching. *J Mater Process Technol* 2016;228:43–58. <https://doi.org/10.1016/j.jmatprotec.2015.09.036>.
- [146] Eller TK, Greve L, Andres MT, Medricky M, Hatscher A, Meinders VT, et al. Plasticity and fracture modeling of quench-hardenable boron steel with tailored properties. *J Mater Process Technol* 2014;214:1211–27. <https://doi.org/10.1016/j.jmatprotec.2013.12.015>.
- [147] Rahmaan T, Abedini A, Butcher C, Pathak N, Worswick MJ. Investigation into the shear stress, localization and fracture behaviour of DP600 and AA5182-O sheet metal alloys under elevated strain rates. *Int J Impact Eng* 2017;108:303–21. <https://doi.org/10.1016/j.ijimpeng.2017.04.006>.

- [148] VDA 238-100: Plate bending test for metallic materials. 2010.
- [149] Cheong K, Omer K, Butcher C, George R, Dykeman J. Evaluation of the VDA 238-100 Tight Radius Bending Test using Digital Image Correlation Strain Measurement. *J Phys Conf Ser* 2017;896. <https://doi.org/10.1088/1742-6596/896/1/012075>.
- [150] Lu Y, Peer A, Abke T, Kimchi M, Zhang W. Subcritical heat affected zone softening in hot-stamped boron steel during resistance spot welding. *Mater Des* 2018;155:170–84. <https://doi.org/10.1016/j.matdes.2018.05.067>.
- [151] Sherepenko O, Kazemi O, Rosemann P, Wilke M, Halle T, Jüttner S. Transient Softening at the Fusion Boundary of Resistance Spot Welds: A Phase Field Simulation and Experimental Investigations for Al–Si-coated 22MnB5. *Metals (Basel)* 2019;10:10. <https://doi.org/10.3390/met10010010>.
- [152] Mohamadizadeh A, Biro E, Worswick M, Zhou N, Malcolm S, Yau C, et al. Spot Weld Strength Modeling and Processing Maps for Hot-Stamping Steels. *Weld J* 2019;98:241–9. <https://doi.org/10.29391/2019.98.021>.
- [153] Welding C on A. AWS C1.1M Recommended Practices for Resistance Welding. American Welding Society; 2012.
- [154] Ha J, Lim J-HH, Oh C-YY. Construction procedure of spot weld failure model for crash simulation. In: Zhu Y, Zehnder AT, editors. *Conf. Proc. Soc. Exp. Mech. Ser.*, vol. 4, Cham: Springer, Cham; 2017, p. 67–75. https://doi.org/10.1007/978-3-319-42028-8_9.
- [155] Matsuda K, Kodama S. Evaluation of corona bond strength of resistance spot welding. *Sci Technol Weld Join* 2020;25:66–72. <https://doi.org/10.1080/13621718.2019.1613010>.
- [156] Chao YJ. Failure mode of spot welds: interfacial versus pullout. *Sci Technol Weld Join* 2003;8:133–7.
- [157] Bardelcik A, Worswick MJ, Winkler S, Wells MA. A strain rate sensitive constitutive model for quenched boron steel with tailored properties. *Int J Impact Eng* 2012;50:49–62. <https://doi.org/10.1016/j.ijimpeng.2012.06.007>.
- [158] Rosenthal D. Mathematical Theory of Heat Distribution During Welding and Cutting. *Weld J* 1941;20:220–34.
- [159] Biro E. Heat-Affected Zone Softening Kinetics in Dual- Phase and Martensitic Steels. 2014.

- [160] Samadian P, Butcher C, Worswick MJ. New mean-field homogenization schemes for the constitutive modelling of the elastic and elastoplastic deformation behavior of multi-phase materials. *Mater Today Commun* 2020;24:100707. <https://doi.org/10.1016/j.mtcomm.2019.100707>.
- [161] Lee SH. On the Development of Fold Initiator Patterns to Promote Progressive Folding of Hot Stamped Ultra- High Strength Axial Crush Structures. University of Waterloo, 2021.
- [162] Samadian P, ten Kortenaar L, Omer K, Butcher C, Worswick MJ. Fracture characterization of tailored Usibor® 1500-AS and damage modelling based on a coupled-micromechanical-phenomenological strategy. *Eng Fract Mech* 2020;223:106785. <https://doi.org/10.1016/j.engfracmech.2019.106785>.
- [163] Ling Y. Uniaxial True Stress-Strain after Necking. *AMP J Technol* 2004;5:37–48.
- [164] Hockett JE, Sherby OD. Large strain deformation of polycrystalline metals at low homologous temperatures. *J Mech Phys Solids* 1975;23:87–98. [https://doi.org/10.1016/0022-5096\(75\)90018-6](https://doi.org/10.1016/0022-5096(75)90018-6).
- [165] Wierzbicki T, Xue L. On the Effect of the Third Invariant of the Stress Deviator on Ductile Fracture. Tech Report, Impact Amd Crashworthiness Lab Massachusetts Inst Technol Cambridge, MA 2005;136.
- [166] Bai Y, Wierzbicki T. A new model of metal plasticity and fracture with pressure and Lode dependence. *Int J Plast* 2008;24:1071–96. <https://doi.org/10.1016/j.ijplas.2007.09.004>.
- [167] Gavin HP. The Levenberg-Marquardt Algorithm For Nonlinear Least Squares Curve-Fitting Problems. Duke Univ 2019:1–19.
- [168] Levenberg K. A method for the solution of certain non-linear problems in least squares. *Q Appl Math* 1944;2:164–8. <https://doi.org/10.1090/qam/10666>.
- [169] Lyons T, Souza KD. Investigation of Mesh Regularization in MAT _ 224 for Subsequent Use in Impact Simulations. 16th Int. LS-DYNA User Conf., 2020, p. 1–16.
- [170] Khandoker N, Takla M. Tensile strength and failure simulation of simplified spot weld models. *Mater Des* 2014;54:323–30. <https://doi.org/10.1016/j.matdes.2013.08.070>.
- [171] Sadigh MAS, Marami G, Paygozar B. Failure simulation in resistance spot-welded lap-joints using cohesive zone modeling. *J Cent South Univ* 2018;25:2567–77.

<https://doi.org/10.1007/s11771-018-3936-z>.

Appendix A

Mohamadizadeh A, Biro E, Worswick M, Zhou N, Malcolm S, Yau C, Jiao Z, Chen K. “Spot Weld Strength Modeling and Processing Maps for Hot-Stamping Steels”. *Weld. J.*, 2019;98:241–9.

**“Accessible through the link below as well as the University of Waterloo’s
Institutional Repository (UW Space)”**

<https://s3.amazonaws.com/WJ-www.aws.org/supplement/2019.98.021.pdf>

Appendix B

Mohamadizadeh A, Biro E, Worswick M. “Shear band formation at the fusion boundary and failure behaviour of resistance spot welds in ultra-high-strength hot-stamped steel”. *Sci. Technol. Weld. Join.* 2020;0:1–8.

**“Accessible through the link below as well as the University of Waterloo’s
Institutional Repository (UW Space)”**

<https://www.tandfonline.com/doi/full/10.1080/13621718.2020.1773057>

Appendix C

Mohamadizadeh A, Biro E, Worswick M. “Novel Double-Half Spot Weld Testing Technique For Damage Progress And Failure Analysis Using Digital Image Correlation Techniques”. Exp. Mech. 2021.

**“Accessible through the link below as well as the University of Waterloo’s
Institutional Repository (UW Space)”**

<https://doi.org/10.1007/s11340-021-00743-4>

Appendix D

Sherepenko O, Mohamadizadeh A, Zvorykina A, Worswick M, Biro E, Jüttner S. “Determination of resistance spot weld failure path in ultra-high-strength press-hardened steel by control of fusion boundary transient softening”. *J Mater Sci* 2021;56:14287–97.

**“Accessible through the link below as well as the University of Waterloo’s
Institutional Repository (UW Space)”**

<https://doi.org/10.1007/s10853-021-06165-w>

Appendix E

Mohamadizadeh A, Biro E, Worswick M.” Failure characterization and meso-scale damage modeling of spot welds in hot-stamped automotive steels using a hardness-mapping approach”, Eng. Frac. Mech., Under Review (2021).

(Under review- External Link not available)